Pannexin 1 regulates dendritic spines in developing cortical neurons

by

Juan C. Sanchez-Arias
Doctor of Medicine, Universidad del Valle, 2014

A Dissertation Submitted in Partial Fulfillment
of the Requirements for the Degree of

DOCTOR OF PHILOSOPHY

in the Division of Medical Sciences (Neuroscience)

Supervisory Committee

Pannexin 1 regulates dendritic spines in developing cortical neurons

by

Juan C. Sanchez-Arias
Doctor of Medicine, Universidad del Valle, 2014

Supervisory Committee

Dr. Leigh Anne Swayne, Division of Medical Sciences
Supervisor

Dr. Craig E. Brown, Division of Medical Sciences
Departmental Member

Dr. Robert Chow, Department of Biology
Outside Member

Abstract

Sensory, cognitive, and emotional processing are rooted in the cerebral cortex. The cerebral cortex is comprised of six layers defined by the neurons within them that have distinctive connection, both within cortex itself and with other subcortical structures. Although still far from solving the mysteries of the mind, it is clear that networks form by neurons in the cerebral cortex provide the computational substrate for a remarkable range of behaviours. This neuron-to-neuron activation is mediated through dendritic spines, the postsynaptic target of most excitatory synapses in the cerebral cortex. Dendritic spines are small protrusions found along dendrites of neurons, and their number, as well as structural changes, accompany the development of synapses and establishment of neuronal networks. In fact, dendritic spines undergo rapid structural and functional changes guided by neuronal activity. This marriage between structural and functional plasticity, makes dendritic spines crucial in fine-tuning of networks in the brain; not surprisingly, dendritic spine aberrations are a hallmark of multiple neurodevelopmental, neuropsychiatric, and neurodegenerative disorders. With this in mind, I considered Pannexin 1 (Panx1) an interesting novel candidate for a regulatory role on cortical neuronal network and dendritic spine development, for the following reasons. First, *Panx1* transcripts are enriched in the brain and in the cortex are most abundant during the embryonic and early postnatal period. . This timing roughly corresponds to a period of synaptogenesis in the postnatal brain. Second, Panx1 localizes to postsynaptic compartments in neurons and its disruption leads to enhance excitability and potentiation of neuron-to-neuron communication. Third, disruption of Panx1 (either knockdown or pharmacological blockade) leads to neurite outgrowth in neuron-like cells. Lastly, genetic variants in *PANX1* have been associated with neurodevelopmental disorders. This dissertation explores the role of Panx1 in the development of dendritic spines and neuronal networks, furthering our

understanding on cortical development and placing Panx1 as a novel regulator of structural and functional plasticity in the brain.

Chapter 1 discusses core concepts on cortical development, with an emphasis on pyramidal neuron, the most abundant and only known projection neurons in the cerebral cortex. Here, I review the embryonic origin of pyramidal neurons, their postnasal development, and how cortical circuits are assembled. I finish this chapter with a brief review on Panx1 and its known expression and involvement in neuronal function.

In Chapter 2 I explore the functional properties of neuronal networks and synaptic composition of cortical neurons in the absence of Panx1. Using live cell imaging and analysis of Ca^{2+} transients in dense primary cortical cultures, revealed that *Panx1* knock-out (KO) cultures exhibit more and larger groups of significantly co-activated neurons, known as network ensembles. These network properties were not explained by differences in cell viability or cell-type composition. Examination of protein expression from cortical synaptosome preparations revealed that Panx1 is enriched in synaptic compartments, while also confirming a developmental downregulation. This analysis also revealed increased levels of the postsynaptic scaffolding protein PSD-95, along with the postsynaptic glutamate receptors GluA1 and GluN2A. Lastly, *ex vivo* tracing of dendritic spines on apical dendrites of Layer 5 pyramidal neurons in global and glutamatergic-specific *Panx1* KO brain slices revealed higher spine densities in early and late postnatal development, with no differences in spine length. Analysis of dendritic spine densities in fixed cultured cortical neurons revealed an increase associated with *Panx1* KO. Altogether, this work presents for the first time a connection between Panx1 and structural development of dendritic spines and suggest that Panx1 regulates cortical neuronal networks through changes in spine density.

Chapter 3 examines the influence of Panx1 on spiny protrusions growth and movement. Spiny protrusion are long, thin, highly dynamic spine precursors. Taking advantage of a

fluorescent signal localized to the plasma membrane, I visualized spiny protrusions and quantified their dynamics in wildtype (WT) and *Panx1* KO developing cortical neurons, both under fixed and live conditions. I found that transient Panx1 expression is associated with decreased spiny protrusion density both in WT and *Panx1* KO neurons. Using live cell imaging, I found that spiny protrusions are more stable and less motile in *Panx1* KO neurons, while its transient expression reversed both of these phenotypes. These results suggest that Panx1 regulation of dendritic spines development is rooted partly in the regulation of spiny protrusion dynamics.

Overall, this dissertation demonstrates that Panx1 negatively regulates dendritic spines in part by influencing spiny protrusion dynamics. It is reasonable to speculate that Panx1 regulation of dendritic spines underlies its newly discovered role in the formation network ensembles, providing a putative mechanism for previously described roles of Panx1 in synaptic plasticity. Likewise, this body of work furthers our understanding of Panx1 by filling some of the gaps attached to its developmental expression and association with neurodevelopmental disease.

Table of Contents

List of Abbreviations

+TIPs	microtubule plus-end tracking proteins
AMPA	α-amino-3-hydroxy-5-methyl-4-isoxazolepropionic acid
Arp3	actin related protein 3
ATP	adenosine triphosphate
BP	bipolar
bp	base pair
BDNF	brain-derived neurotrophic factor
Brsk1/2	serine/threonine-protein kinase 1/2
BSA	bovine serum albumin
Ca^{2+}	calcium ions
CAM	cell adhesion molecule
Camkk1	calcium/calmodulin-dependent protein kinase kinase 1
cAMP	cyclic adenosine monophosphate
CP	cortical plate
CR	Cajal-Retzius neuron
Crmp2	collapsin response mediator protein 2
DIV	days *in vitro*
DMEM	Dulbecco's modified Eagle medium
DNA	deoxyribonucleic acid
ECL	enhanced chemiluminescence substrate
EDTA	ethylenediaminetetraacetic acid
EGFP	enhanced green fluorescent protein

EM	electron microscopy
Emx1	empty spiracles homeobox 1
ESC	embryonic stem cell
FIJI	Fiji is just ImageJ
FluoroSNNAP	Fluorescence Single Neuron and Network Analysis Package
Fmr1	fragile X mental retardation 1
FPKM	Fragments Per Kilobase of transcript per Million
GABA	gamma-aminobutyric acid
GFAP	glial fibrillary acidic protein
GluA1	AMPA receptor subunit 1
GlluA2	AMPA receptor subunit 2
GluN1	NMDA receptor subunit 1
GluN2A	NMDA receptor subunit 2A
GluN2B	NMDA receptor subunit 2B
Glut	Glutamate
GO	gene ontology
HBSS	Hank’s balanced salt solution
HRP	horseradish peroxidase
IKNM	interkinetic nuclear migration
IP3	inositol triphosphate
IZ	intermediate zone
KO	knock-out
LTD	long-term depression

LTP	long-term potentiation
Mark2	microtubule affinity-regulating kinase 2
MP	multipolar
MT	microtuble
MZ	marginal zone
N2a	neuro-2a
NMDA	N-methyl-D-aspartate
NMDAR	N-methyl-D-aspartate receptor
NPC	neural precursor cell
OPC	oligodendrocyte progenitor cell
P2XR	ionotropic purinergic receptor
P2YR	metabotropic purinergic receptor
P2X7R	purinergic receptor P2X7
Panx	pannexin
Panx1	pannexin 1
Panx2	pannexin 2
Panx3	pannexin 3
PP	preplate
PBS	phosphate buffered saline
PCR	polymerase chain reaction
PFA	paraformaldehyde
PMSF	phenylmethylsufonyl fluoride
PSD	postsynaptic density

PSD-95	postsynaptic density proteins 95
PVDF	polyvinylidene fluoride
RGC	radial glial cell
RIPA	radio-immunoprecipitation assay
RNA	ribonucleic acid
rpm	rotations per minute
SDS-PAGE	sodium dodecyl sulfate polyacrylamide gel electrophoresis
SVZ	subventricular zone
Syngap1	synaptic Ras GTPase-activating protein 1
TBS	TRIS buffered saline
UVIC	University of Victoria
VZ	ventricular zone
WT	wildtype

List of Tables

List of Figures

Acknowledgments

I would like to express the upmost gratitude to my advisor and mentor Dr. Leigh Anne Swayne who gave me the opportunity to pursue this research. I will be forever thankful for her guidance, encouragement, and constant support throughout these years that allowed to become more than a scientist. I also want to thank Dr. Craig E. Brown and Dr. Robert (Bob) Chow for kindly accepting being part of my thesis committee. Their guidance, advice, and critical feedback throughout the project were key.

Funding for this project was provided by operating grants from the Canadian Institutes of Health Research (CIHR Grant MOP142215), The Scottish Rite Charitable Foundation of Canada (15118), and the University of Victoria-Division of Medical Sciences to Dr. Leigh Anne Swayne, which were critical for my graduate journey as an international student. I was also fortunate to count with support from the University of Victoria Graduate Fellowships and Donor Awards.

I want to thank the amazing members of the Swayne Lab, for their experimental help, moral support, and countless of stimulating conversations. Their assistance accelerated several tasks and allowed this project to reach unprecedented goals. Andrew and Leigh - were great colleagues whose advice I will always remember. Lena, Catherine, Anna, and Sarah, your constant encouragement kept me motivated even during the most difficult times. I cannot think of a better group of people to collaborate with and grow scientifically. To my love Caitlin, thank you for support, care, and a life worth of smiles and happiness,

Lastly and most importantly, I want to thank my beloved mother Alid and my beloved brother Reinaldo who have always put up with me, support my craziest ideas, and allowed to pursue my wildest dreams.

Dedication

A mi amada madre Alid, a mi adorado hermano Rei, y a mi padre Reinaldo (Q.E.P.D.)

por siempre creer en mi

"Todo hombre puede ser, si se lo propone, escultor de su propio cerebro"

- *Santiago Ramon y Cajal*

1 Chapter 1: Introduction

1.1 Development of pyramidal neurons in the cerebral cortex

1.1.1 Origin of cortical pyramidal neurons

The mammalian cerebral cortex plays a central role in sensory, emotional, and cognitive processing (Rubenstein, 2011). As the outer mantle of neural tissue, it is organized in six layers, each containing molecularly and functional distinct groups of excitatory projection (pyramidal) neurons and inhibitory interneurons (Kwan et al., 2012). Pyramidal neurons originate from asymmetrical cellular division of neural progenitor cells (NPCs) in the ventricular zone (VZ) and populate the cerebral cortex in an *inside-outside* fashion (Bystron et al., 2008): earlier born cells migrate radially to the inner layers 6 (L6) and L5, while late born cells reach the outer layers L4, L3, and L2 (Figure 1).

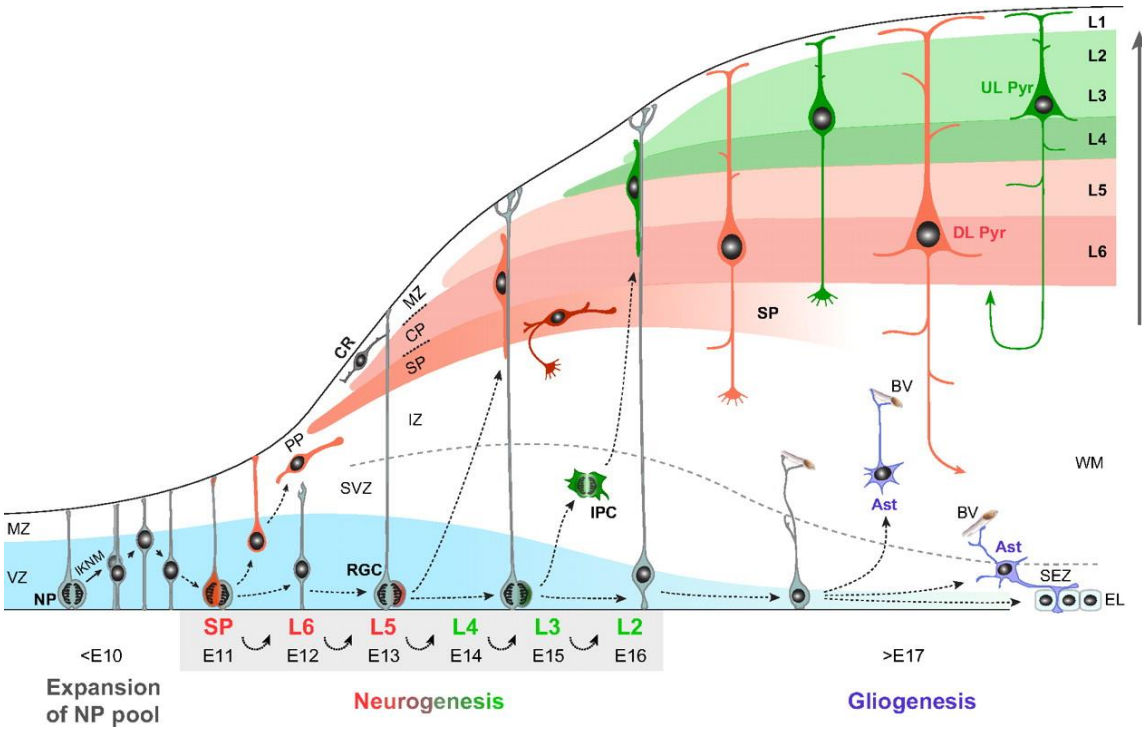

Figure 1.1. Pyramidal neurons migrate radially in an *inside-out* fashion to form the cerebral cortex. Early in embryonic development, neural precursor (NP) cells in the ventricular zone (VZ) undergo interkinetic nuclear migration (IKNM) and expand their pool through symmetrical cellular division. After embryonic day 10 (E10), asymmetrical division triggers NPCs to give rise to neuroblasts, which migrate radially using radial glial cells (RGCs) processes initially, reaching the preplate (PP) to form the cortical plate (CP) that will develop into layers L2-L6. CP neurons separate the PP into the subplate (SP) and marginal zone (MZ), with earlier born cells occupying deep layers (L6, L5), followed by wave of later born cells that is complemented by intermediate precursor cells (IPCs) in the subventricular zone (SVZ) and intermediate zone (IZ) and organize into the upper layers (L4, L3, and L2) as upper-layer pyramidal neurons. This process is completed by E17, after which NPCs become gliogenic and give rise cortical subependymal zone (SEZ) astrocytes (Ast) as well as the ependymal layer (EL). CR, Cajal-Retzius neuron; BV, blood vessel; DL Pyr, deep-layer pyramidal neuron; UL Pyr, upper-layer pyramidal neuron, WM, white matter. Used with permission from Kwan et al. (2012); Copyright Clearance Center Order License ID 1018962-1.

Deep layer cortical pyramidal neurons project mainly outside the cerebral cortex (corticofugal), with a small group of layer 5 neurons (known as intratelencephalic L5A neurons) projecting to intracortical targets (Hallman et al., 1988; Kim et al., 2015). Upper layer cortical pyramidal neurons project to ipsilateral or contralateral targets (Molyneaux et al., 2007). Both deep and upper layer neurons can be further classified by the transcriptions factors they express (Kwan et al., 2012).

1.1.2 Morphological development of cortical pyramidal neurons

Cortical pyramidal neurons, also known as principal cells, have been considered the basic building blocks of cortical circuits since their initial descriptions derived from Golgi impregnated neural tissue (Cajal, 1894, 1995). Characterized by their triangular (sometimes ovoid) cell body, pyramidal neurons are exclusively found in the cerebral

cortex, where they are the most abundant and sole projection neurons (Peters and Jones, 1984). The typical pyramidal neuron extends a thick apical dendrite towards the pial surface. Oblique branches extend from this apical dendrite as it ascends towards the pial surface. From the base, large basal dendrites emerge. This basal dendrites continue laterally or downward (towards the corpus callosum) and account for approximately 90% of the total dendritic length of the pyramidal cell (Larkman, 1991; DeFelipe and Fariñas, 1992). A prominent feature of the pyramidal neuron dendritic arbor is that all dendritic surfaces are covered by microscopy protrusions called dendritic spines, with the exception of most of the proximal segment (approximately 10 µm from the cell body limit) which are spine-free. Also, the axon emerges from the base of cell body, and projects towards ipsilateral cortical targets or downwards joining the corticofugal tracts(Peters and Jones, 1984; DeFelipe and Fariñas, 1992).

Dendrites and axons of pyramidal cells (and all neurons) are structurally and functionally distinct, with dendrites serving as receptive fields and axons acting as output structures. Such asymmetry reflects the flow of information in the nervous system (dendrite to soma to axon) and is one of the most striking examples of cell polarization (Solecki et al., 2006; Takano et al., 2015). Work performed using dissociated cultured neurons derived from rodents established that neurons cultured *in vitro* develop their dendrites and axon in five stages (Figure 1.2A, (Dotti et al., 1988; Banker, 2018)). Immediately after isolation, neurons in stage 1 resemble spheres and extend a relatively small number of filopodia shortly after plating (1-2 hours). Then, in stage 2, about 12 and 36 hours after plating, neurons retract and elongate multiple unpolarized neurites until stage 3, when a single neurite grows rapidly specifying into the axon at 2 days *in vitro* (DIV2). Axonal

specification is achieved by local activation of downstream neurotrophic signalling pathways that regulate the neuronal cytoskeleton and trafficking. This specification not only depletes local neurotrophic factors but also triggers a negative-feedback loop that prevents the formation of additional axons; the combined effect is known as global inhibition (Solecki et al., 2006; Nakamuta et al., 2011; Takano et al., 2015). During stage 4 unspecified neurites develop into dendrites (DIV4-7), and lastly, in stage 5 (DIV7 and onwards) dendrites continue to develop and are populated by dendritic spines (Dotti et al., 1988).

Use of organotypic slices has captured the polarization of cortical neurons within the extracellular environment present in the developing cortex, shedding some light on the influence of extracellular cues in the formation of axons and dendrites (Funahashi et al., 2014). Neurons migrating from the VZ start as multipolar (MP) cells with multiple minor neurites; Then, one of these minor neurites grows rapidly towards the within the IZ, becoming the trailing process. Meanwhile, another neurite oriented towards the pial surface turns into leading process (Figure 1.2B). The trailing process specifies into the axon and the leading process into the apical dendrite, while all other minor neurites retract giving a bipolar shape (Miyata, 2004; Noctor et al., 2004). Once these fully polarized bipolar neurons reach the CP they develop into pyramidal neurons and continue to grow their dendrites which become populated by spines; dendrite growth reaches a plateau by postnatal day 20 (P20) for segments near to the cell body, while distal segments and branches continue to develop well into adulthood (Petit et al., 1988). The molecular mechanisms underlying neuronal polarization *in vivo* include extrinsic factors such as neurotrophins, adhesion molecular, and cell-to-cell interactions as well as intrinsic factors

that include the Rho family of GTPases and kinases such as Mark2, Brsk1/2, and Camkk1; however, how developing neurons integrate these signals *in vivo* remains elusive (Funahashi et al., 2014; Dong et al., 2015).

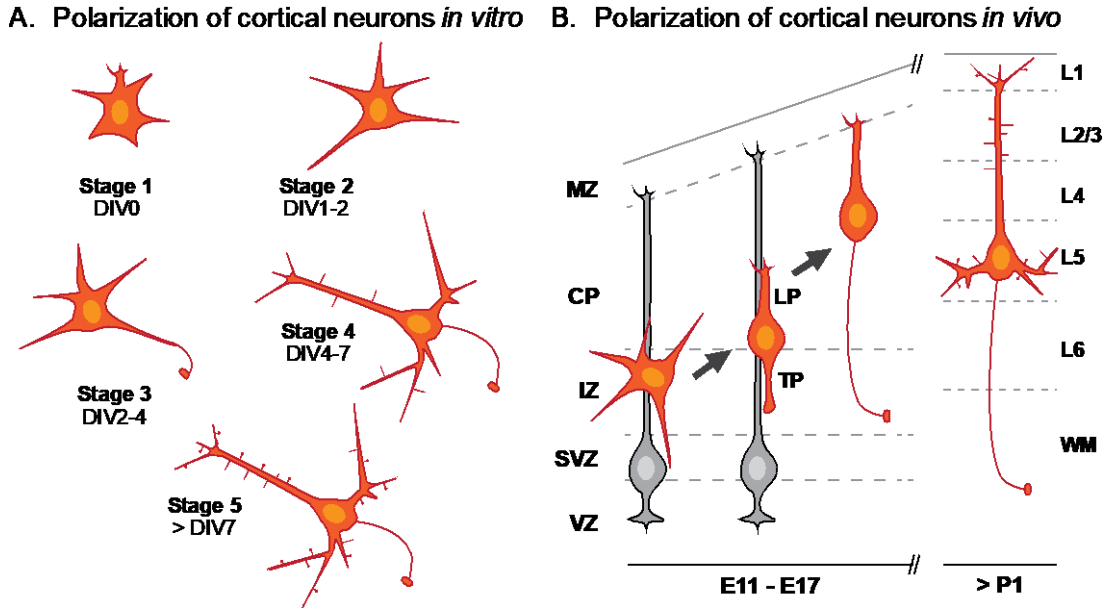

Figure 1.2. Comparison of cortical neuron polarization. The flow of information in the nervous system has dendrites as receptive fields and axons as signal output structures. This functional compartmentalization is reflected structurally, with dendrites and axons representing clearly distinct types of neurites. ***A*** Cortical neurons *in vitro* develop and polarize in five stereotypical stages (Dotti et al., 1988); see text for further description. ***B.*** Polarization of cortical neurons *in vivo* is influenced by extrinsic and intrinsic cues. During migration, neurons initially assume a multipolar morphology, followed by the growth of a trailing process (TP) and a leading process (LP), which will become the axon and apical dendrite, respectively. Once the polarized neuron (with a bipolar morphology) reaches the cortical plate (CP), further dendrite development leads to the formation of dendritic spines and synapses. DIV, days *in vitro*; MZ, marginal zone; IZ, intermediate zone; SVZ, subventricular zone; VZ, ventricular zone; P, postnatal day; L, cortical layer.

1.1.3 Postnatal dendritic spine formation in pyramidal neurons

1.1.3.1 Structure and function of dendritic spines

A prominent feature of all pyramidal neurons is the presence of dendritic spines populating their dendritic trees (Cajal, 1894; DeFelipe and Fariñas, 1992). Dendritic spines are postsynaptic specializations that develop from small membranous protrusions that mature and stabilize to receive excitatory inputs (Ziv and Smith, 1996; Yuste and Bonhoeffer, 2004; Holtmaat et al., 2005). As key elements of the synapse, dendritic spines play important roles in neural information processing and assembly of circuits (Yuste, 2011). Similarly, dendritic spine structural or functional abnormalities have been identified in various neuropsychiatric disorders, such as autism spectrum disorder (ASD), schizophrenia, and intellectual disability (Forrest et al., 2018; Lima-Caldeira et al., 2019); highlighting the importance of these structures in cortical function.

The ultrastructure of dendritic spines is characterized by a bulbous head and a slim neck (Figure 1.3A; Harris and Weinberg, 2012). The head of the dendritic spine (~200 – 1400 nm) contains the electron-dense postsynaptic density (PSD) (Gray, 1959; Gulley and Reese, 1981) where scaffolding proteins, such as PSD-95, serve as anchors for glutamate receptors (Chen et al., 2008). Dendritic spine head size scales with synaptic strength and efficacy; larger spine heads contain more PSD-95 and glutamate receptors which results in larger excitatory postsynaptic potentials (Matsuzaki et al., 2004; Segal, 2005). In contrast, decreasing synaptic efficacy causes dendritic spine head shrinkage or loss of dendritic spines (Figure 1.3B; Okamoto et al., 2004; Oh et al., 2013).The neck of dendritic spines, with a diameter typically between ~100-300 nm serves as a diffusion barrier, thereby compartmentalizing a distinct biochemical and electrical unit within the spine head (Svoboda et al., 1996; Kwon et al., 2017). Such compartmentalization isolates the

machinery required to regulate the activity at the level of single synapses and enables operational separation of individual synapses (Higley and Sabatini, 2012).

Dendritic spines undergo rapid and reversible morphological changes during their development. Complex cytoskeletal dynamics are driven by converging developmental signalling and synaptic activity based mechanisms, (reviewed in Dent et al., 2011). Dendritic spines are enriched in filamentous actin (F-actin), whose network supports the spine head and neck (Figure 1.3A; Harris and Weinberg, 2012). Actin network remodelling induced by synaptic activity is mediated through signalling cascades involving multiple actin binding proteins such as ADF/cofilin, actin-related protein-2/3 (Arp2/3) complex, profilin, debrin, Ca^{2+}/calmodulin-dependent protein kinase type II subunit β (CaMKIIβ), and alpha-actinin (Hotulainen and Hoogenraad, 2010). In addition to changes in the actin cytoskeleton, activity-dependent invasion of microtubules has been observed in dendritic spines (Gu et al., 2008; Hu et al., 2008), which requires actin remodelling and actin-microtubule crosstalk (Schätzle et al., 2018).

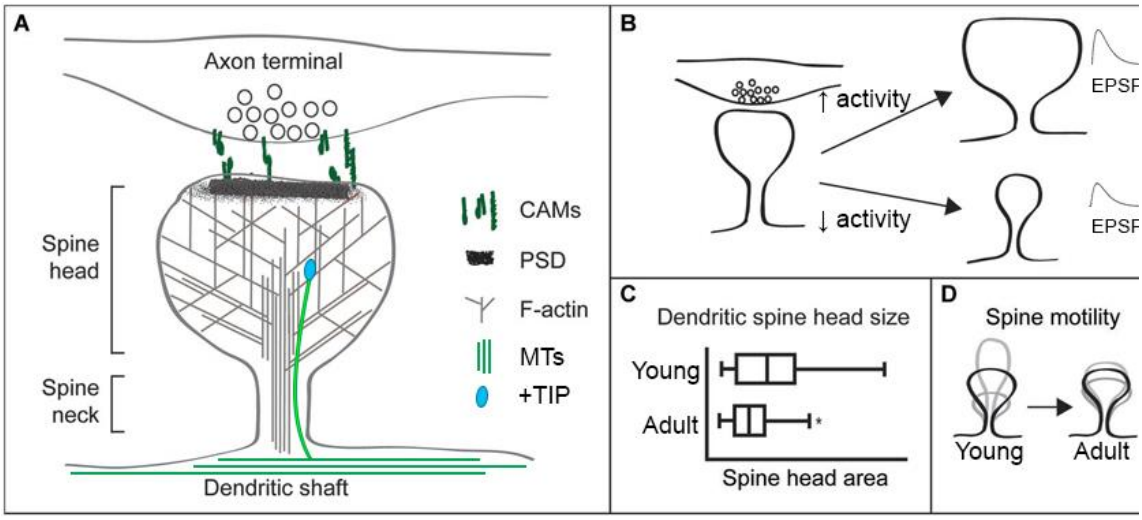

Figure 1.3. Dendritic spines are highly plastic synaptic specializations. ***A.*** Dendritic spines are small postsynaptic protrusions, which are apposed to presynaptic terminals through cell adhesion molecules

(CAMs). Crosstalk between actin and microtubules regulates dendritic spine morphology development. ***B.*** Neuronal activity regulates dendritic spine structural changes, both at the spine head and neck (Matsuzaki et al., 2004; Araya et al., 2014). ***C.*** Dendritic spine head size is developmentally regulated (Harris, 1999). ***D.*** Spine motility is also developmentally regulated: immature neurons exhibit highly motile spines, while mature neurons have more stable spines (Dunaevsky et al., 1999). CAMs (cell adhesion molecules; PSD; postsynaptic density; F-actin, filamentous actin; MTs; microtubules; +TIP, microtubule plus-end tracking proteins; EPSP, Excitatory postsynaptic potential. Adapted with permission from Levy et al. (2014). Creative Commons Attribution License CC BY 4.0.

Dendritic spine structure is also developmentally regulated (Figure 1.3D). Longitudinal imaging of dendritic spines at various developmental stages has revealed that dendritic spine stability and turnover decrease with age; this is reversed with sensory deprivation (Dunaevsky et al., 1999; Zuo et al., 2005b, 2005a). Despite this body of knowledge, the underlying mechanisms and processes that play a role in developmental regulation of dendritic spines are still poorly understood.

1.1.3.2 *In vitro* and *in vivo* formation of dendritic spines synapses

Developmental formation of dendritic spines starts as an activity-independent process as evidenced by the normal assembly of the brain and cortex, normal neuronal development, and presence functional spines and synapses in the absence of glutamatergic (excitatory) neurotransmission (Verhage et al., 2000; Harms and Craig, 2005; Lu et al., 2013; Sando et al., 2017; Sigler et al., 2017). This intrinsic developmental program lays out a general neuronal connectivity plan that is further refined and maintained through activity-dependent mechanisms.

An important step in the assembly of synapses is the contact of postsynaptic structures, such as dendritic spines, with presynaptic partners (axon terminals). Seminal work using

dissociated neuronal cultures showed that filopodia-like spiny protrusions on dendritic shafts survey their extracellular environment in search of a presynaptic partner (Ziv and Smith, 1996). The dynamic nature of these structures is highest early in neuronal development (~DIV7-10) and declines with maturation (>DIV15). Once these spiny protrusions stably contact a presynaptic terminal, activation of a developmental program leads to maturation into functional dendritic spines (Ziv and Smith, 1996). In this regard, CAMs are the most likely molecular players behind developmental spine and synapse formation, as these transmembrane proteins connect and organize pre- and postsynaptic compartments. The specific CAMs and their mechanism(s) of action contributing to synapse formation remains to be fully elucidated (reviewed in Südhof, 2018).

Long term imaging in organotypic slices and in living animals have confirmed and expanded the initial observations by Ziv and Smith (1996), allowing unprecedented longitudinal visualization of dendritic spines throughout development (Zuo et al., 2005a). Similar to what has been observed in dissociated cultures, spiny protrusions and dendritic spines in organotypic slices and in living animals are characterized by a high degree of motility and turnover (formation and elimination) during the first two postnatal weeks, which sharply declines after the third postnatal week, when most dendritic spines stabilize (Dunaevsky et al., 1999; Trachtenberg et al., 2002; Holtmaat et al., 2005; Zuo et al., 2005a). These observations agree with previous and recent tri-dimensional reconstructions of L5 pyramidal neurons at various developmental timepoints, in which dendritic spine numbers increase throughout the dendritic tree between the first and third postnatal week, concurrently with a transition from filopodia-like spiny protrusions to dendritic spines (Petit et al., 1988; Romand et al., 2011).

After the initial contact, pre- and postsynaptic components assemble within 1-2 hours in cultured dissociated neurons (Friedman et al., 2000). Translocation of PSD-95 into spiny protrusions plays a major role in their stability, maintenance, and maturation. For example, over-expression of PSD-95 induces clustering of glutamate receptors and enhances their activity, leading to maturation of pre- and postsynaptic compartments (El-Husseini et al., 2000). Moreover, spiny protrusions bearing clusters of PSD-95 are more stable and do not turnover in dissociated neurons (Prange and Murphy, 2001), while studies from living animals have shown that newly formed spines that failed to acquire PSD-95 clusters are eliminated (Cane et al., 2014).

1.2 Development of neuronal networks in the cerebral cortex

Neuronal networks, both *in vitro* and *in vivo*, feature self-sustaining bursts lasting a few hundred milliseconds (Murphy et al., 1992; Tibau et al., 2013; Miller et al., 2014; Arce-McShane et al., 2016). Using Ca^{2+} imaging one can investigate the development of neuronal networks both *in vitro* and *in vivo* with single cell resolution (Murphy et al., 1992; Adelsberger et al., 2005; Tibau et al., 2013; Miller et al., 2014). Early developing networks are characterized by long inter-burst intervals and large amplitude network-wide events. As the network matures, the inter-burst timing is significantly reduced and select groups of neurons with high interconnection and synchronicity emerge (Tibau et al., 2013). Such select groups of significantly co-activated neurons are referred to as network ensembles (Buzsáki, 2010; Miller et al., 2014; Hoshiba et al., 2017), and are thought to be the functional building blocks of the cerebral cortex, providing the substrate for sensory processing, memory formation, and consciousness (Miller et al., 2014; Carrillo-Reid et al., 2016; Wenzel et al., 2019).

Why would cerebral cortex computations require network ensembles? The precise recruitment of distinct network ensembles provides flexibility to cortical circuits to adapt their function by simply strengthening or weakening already established connections (Yuste, 2011). In this manner, an established cortical circuit with a limited number of neurons can trigger diverse behaviours by selectively engaging specific synapses (Figure 1.4; Yuste, 2011; Hoshiba et al., 2017). This flexibility required for behavioural development highlights the importance of controlled refinement of postnatal cortical circuitry that occurs during periods of heightened plasticity known as *critical periods* (Hensch, 2005).

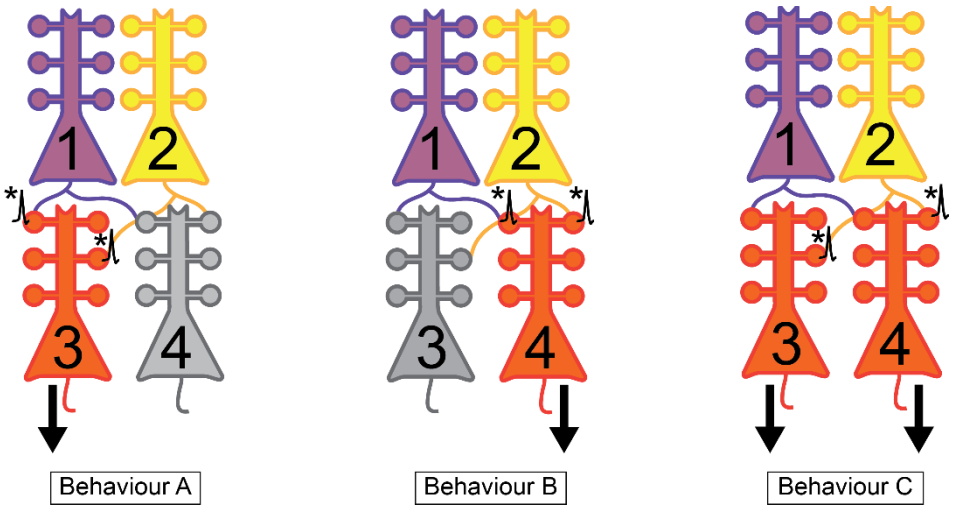

Figure 1.4. Dendritic spine synapses provide flexibility to network ensembles. Strengthening or weakening of specific synaptic connections (requiring stabilization and maturation of dendritic spines) in an established circuit leads to different operational outputs. For example, given a small circuit of 4 neurons, recruitment of a subset of synapses in neuron 3 and 4 produces "Behaviour A" and "Behaviour B", respectively, while simultaneous recruitment of specific synapses in neuron 3 and neuron 4 leads to "Behaviour C". Adapted with permission from Hoshiba et al. (2017). Creative Commons Attribution License CC BY 4.0.

1.3 Regulation of neural development by pannexin 1 channels

1.3.1 Properties of pannexin 1 (Panx1) channels

The family of pannexin (Panx) channel-forming proteins (Panx1, Panx2, Panx3) were discovered relatively recently via sequence similarity to invertebrate innexin gap junction-forming proteins (Panchin et al., 2000; Baranova et al., 2004). However, despite similar membrane topology, Panxs form large-pore channels rather than gap junctions; it has been speculated that this due to glycosylation of Panx extracellular loops (reviewed in Sosinsky et al., 2011). Similar to innexins and other large pore channels, such as connexin hemichannels and the LRRC8 family of channels (known as SWELL channels), Panxs have four transmembrane domains, two extracellular loops, and intracellular N- and C-termini (Penuela et al., 2013; reviewed in Chiu et al., 2018; Michalski et al., 2019; Deng et al., 2020a).

The region of greatest sequence differences between Panx family members is found at the C-terminus (Penuela et al., 2009, 2013). Considering that C-termini play important roles in the regulation and function of channel proteins, it is reasonable to speculate that Panx C-termini in underlie their functional and subcellular diversity (Ambrosi et al., 2010; Bhalla-Gehi et al., 2010; Wicki-Stordeur et al., 2013).

In line with its ubiquitous expression throughout the body, Panx1 has been implicated in numerous cellular processes in health and disease such as apoptosis, cell proliferation and maintenance, inflammatory signalling, regulation of blood pressure, and and maladaptive nervous system plasticity (Chekeni et al., 2010; Xiao et al., 2012; Billaud et al., 2015; Yang et al., 2015; Weilinger et al., 2016; Wicki-Stordeur et al., 2016; Burma et al., 2017; Weaver et al., 2017). The contribution to such a variety of cellular responses is largely influenced by the capacity of Panx1 to promote ATP release, and the downstream effects on

purinergic receptor signalling systems (Sandilos et al., 2012; reviewed in Dahl, 2015; Sanchez-Arias et al., 2016).

Until recently, single molecule techniques and biochemical approaches suggested that Panx1 channels consisted of hexameric oligomers (Boassa et al., 2007; Wang et al., 2014; Chiu et al., 2017). However, several recent cryo-electron microscopy studies have further resolved the Panx1 structure (at low Angstrom resolution, 3 - 3.8 Å) revealing a heptameric configuration(Deng et al., 2020b; Jin et al., 2020; Michalski et al., 2020; Qu et al., 2020). These studies have also confirmed that the channel is anion selective. In addition to fluxing anions, Panx1 also plays a role in regulating intracellular Ca^{2+} levels, apoptosis-related metabolites, and potentially transport of lipids (Bialecki et al., 2020; Medina et al., 2020; Yang et al., 2020).

1.3.2 Central nervous system distribution of Panx1 channels

Panx1 transcript levels are relatively higher in embryonic and early postnatal rodent brain and lower adulthood (Ray et al., 2005; Vogt et al., 2005). Neuronal Panx1 expression has been described across many different neuronal cell types, including pyramidal and parvalbumin-positive and calbindin-positive neurons of the cerebral cortex and hippocampus., Additionally, at the neuronal subcellular level, Panx1 appears to be enriched in postsynaptic compartments (Ray et al., 2005; Vogt et al., 2005; Zoidl et al., 2007). Review of a recent RNA-sequencing database of cell types isolated from the developing mouse brain (postnatal day 7, P7) confirms enrichment of *Panx1* in the brain, with the highest transcript levels observed in neurons, oligodendrocyte progenitors, and newly formed oligodendrocytes; meanwhile *Panx1* transcript levels were relatively low in developing microglia and *Panx1* was virtually absent in astrocytes (Zhang et al., 2014).

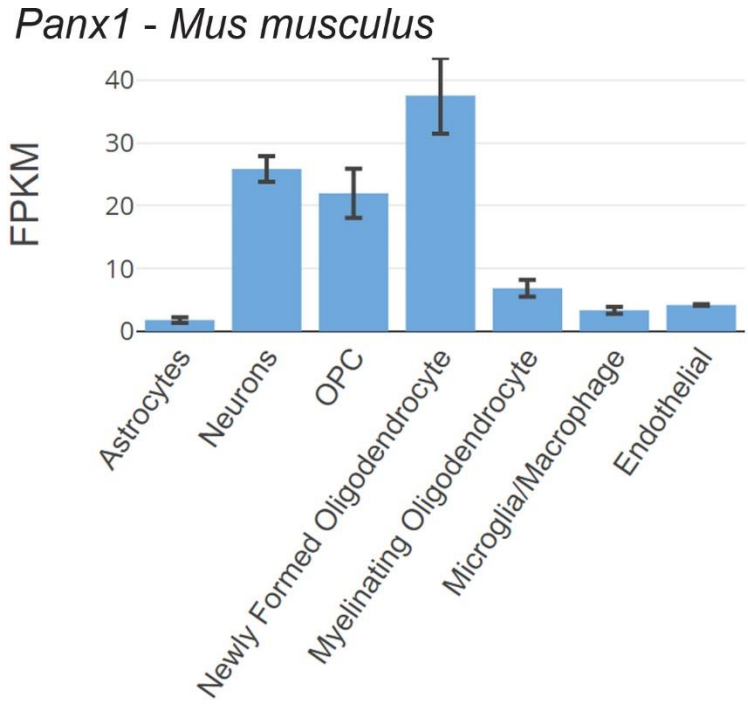

Figure 1.5. *Panx1* transcripts are enriched in developing neurons and developing oligodendrocytes. Zhang et al, prepared cerebral cortices of P7 C57BL/6J to isolate purified representative populations of neurons, astrocytes, oligodendrocyte precursor cells, newly formed oligodendrocytes, myelinating oligodendrocytes, microglia, endothelial cells, and pericytes and generate a transcriptome database. *Panx1* was highly enriched in neurons, OPCs, and newly formed oligodendrocytes, purified using L1CAM and BSL-1-coated plates in medium specified to deplete other cell-types. FPKM, Fragments Per Kilobase of transcript per Million mapped reads; OPC, oligodendrocyte progenitor cell. Produced from the Brain RNA-seq open database available at http://www.brainrnaseq.org/ and based on (Zhang et al., 2014).

1.3.3 Roles of Panx1 in synaptic plasticity and neurite development

The localization of Panx1 to postsynaptic compartments in cortical pyramidal and hippocampal neurons inspired multiple groups to investigate whether Panx1 plays a role in synaptic plasticity. despite the fact that Panx1 null (*Panx1* KO) mice do not exhibit overt behavioural or anatomical abnormalities (reviewed in Penuela et al., 2013). Both genetic ablation and pharmacological blockade of Panx1 increase excitability, enhance (long-term

potentiation) LTP, and preclude long-term depression (LTD) induction in acute hippocampal slices from adult mice (Prochnow et al., 2012; Ardiles et al., 2014). Although more extensive behavioural characterization of *Panx1* KO models is forthcoming, existing studies have reported anxiety-like behaviours, memory impairments, and disruption of the sleep-wakefulness cycle (Prochnow et al., 2012; Ardiles et al., 2014; Kovalzon et al., 2017; Gajardo et al., 2018).

On a more cellular and molecular level, Neuro2 (N2a) cells and NPCs from the VZ exposed to differentiating medium downregulated Panx1 levels, while simultaneously extending neurites. Moreover, disruption of Panx1 induced neurite outgrowth in these cells, suggesting that Panx1 negatively regulates neurite development (Wicki-Stordeur and Swayne, 2013). It has been proposed that these effects on neurites could be mediated through protein-protein interactions between Panx1 C-terminus and various elements of the actin cytoskeleton, such as actin itself, Arp3, and Crmp2 (Bhalla-Gehi et al., 2010; Wicki-Stordeur and Swayne, 2013; Xu et al., 2018).

2 Chapter 2: Panx1 Regulates Network Ensembles and Dendritic Spine Development in Cortical Neurons

This chapter was previously published as a manuscript with the following citation:

Juan C. Sanchez-Arias, Mei Liu, Catherine S. W. Choi, Sarah N. Ebert, Craig E. Brown and Leigh Anne Swayne (2019) ***Pannexin 1 Regulates Network Ensembles and Dendritic Spine Development in Cortical Neurons***. *eNeuro* 6:ENEURO.0503-18.2019.

This work was done with assistance of Mei Liu and Catherine Choi who ran and analyzed western blots in Figure 2.2 and 2.3. Sarah Ebert contributed to the analysis of Ca^{2+} imaging in Figure 2.1 *D,E*. Juan C. Sanchez Arias, Craig E. Brown, and Leigh Anne Swayne wrote the manuscript.

Note the following changes from the published version: Since "Panx1" was already define in the introduction, "Panx1" is used throughout this chapter. Additionally, the accompanying *Visual Abstract* has been incorporated in the discussion.

2.1 Abstract

Dendritic spines are the post-synaptic targets of excitatory synaptic inputs that undergo extensive proliferation and maturation during the first postnatal month in mice. However, our understanding of the molecular mechanisms that regulate spines during this critical period is limited. Previous work has shown that Panx1 regulates neurite growth and synaptic plasticity. We therefore investigated the impact of global *Panx1* KO on spontaneous cortical neuron activity using Ca^{2+} imaging and *in silico* network analysis. *Panx1* KO increased both the number and size of spontaneous co-active cortical neuron network ensembles. To understand the basis for these findings, we investigated Panx1 expression in postnatal synaptosome preparations from early postnatal mouse cortex. Between 2 and 4 postnatal weeks, we observed a precipitous drop in cortical synaptosome

protein levels of Panx1, suggesting it regulates synapse proliferation and/or maturation. At the same time points, we observed significant enrichment of the excitatory postsynaptic density proteins PSD-95, GluA1 and GluN2a in cortical synaptosomes from global Panx1 knockout mice. *Ex vivo* analysis of pyramidal neuron structure in somatosensory cortex revealed a consistent increase in dendritic spine densities in both male and female *Panx1* KO mice. Similar findings were observed in an excitatory neuron-specific *Panx1* KO line (*Emx1-Cre* driven; *Panx1* cKO^{E}) and in primary *Panx1* KO cortical neurons cultured *in vitro.* Altogether, our study suggests that Panx1 negatively regulates cortical dendritic spine development.

2.2 Significance Statement

Our findings reveal an important regulatory role for Panx1 in the formation of connections between nerve cells. We found that removal of Panx1 altered the ability of nerve cells from the cerebral cortex to fire together. We studied the impact of removing Panx1 on the formation of 'dendritic spines', which are microscopic protrusions that receive information from other nerve cells. We found that removing Panx1 increased the expression of proteins involved in dendritic spine function and increased the density of dendritic spines on nerve cells of the cerebral cortex. Together these findings suggest Panx1 is a 'brake' on the development of dendritic spines with important implications for the development of nerve cell connections.

2.3 Introduction

Panx1 forms channels permeable to ions and metabolites (for review, see Boyce et al., 2018), with modes of activation, channel properties and selectivity currently the subject of

intense debate and investigation (Chiu et al., 2018). Nonetheless, Panx1 is enriched in the nervous system, including in neuronal dendrites and spines (Zappalà et al., 2006; Zoidl et al., 2007; Weilinger et al., 2012, 2016; Cone et al., 2013). *Panx1* KO is associated with changes in hippocampal synaptic plasticity(Prochnow et al., 2012; Ardiles et al., 2014) .

Several lines of evidence suggest that Panx1 could regulate the formation of neuronal networks or network ensembles, which are groups of spontaneously co-active neurons. Ensembles are emerging as the functional building blocks of cortical activity that underlie sensorimotor integration and learning and memory (for review see Harris et al., 2003; Miller et al., 2014; Carrillo-Reid et al., 2015; Arce-McShane et al., 2016). The formation of synapses plays a major role in the development of network ensembles, providing the structural basis for higher network connectivity (Jung and Herms, 2014; as reviewed in Hoshiba et al., 2017; Frank et al., 2018). In the rodent cortex, *Panx1* transcript levels peak around the time of birth, and then markedly decline during the first four postnatal weeks (Ray et al., 2005; Vogt et al., 2005). This decrease in *Panx1* coincides with the critical period for the formation of microscopic protrusions emanating from glutamatergic pyramidal neurons called dendritic spines (Schlaggar et al., 1993; for review see O'Leary et al., 1994; Grutzendler et al., 2002; Trachtenberg et al., 2002; for review see Hensch, 2004; Holtmaat et al., 2005), which receive the majority of excitatory inputs in the brain (as reviewed in Nimchinsky et al., 2002; Alvarez and Sabatini, 2007; Yuste, 2011). Panx1 regulates neurite growth (Wicki-Stordeur and Swayne, 2013) and interacts with collapsin-response mediator protein 2 (Crmp2; Wicki-Stordeur, 2015; Xu et al., 2018), a stable synaptic protein (Heo et al., 2018) that regulates spine development (Zhang et al., 2016).

In order to understand how Panx1 regulates cortical neuron development, we used a multi-level approach involving analyses of network ensembles, synaptic protein expression and dendritic spines in mice with global and glutamatergic-neuron specific *Panx1* KO. *Panx1* KO cortical cultures showed increased network ensemble formation. Moreover, *Panx1* KO cortical synaptosomes exhibited significantly increased expression of excitatory synapse markers (PSD-95, GluA1 and GluN2A) and significantly increased cortical neuron dendritic spine densities. Together our results suggest that Panx1 regulates network ensemble formation by acting as a brake for dendritic spine formation.

2.4 Materials and Methods

2.4.1 Antibodies

Primary antibodies used in this study were: mouse anti-Gad67 (1:120, MAB5406, Millipore-Sigma), mouse anti-PSD-95 (1:50 for ICC; 1:1500 for Western blotting, MA1-045, Thermo-Fisher), rat anti-GFAP (1:200; 1:2000, 13-0300, Thermo-Fisher), rabbit anti-MAP2 (1:400, ab32454, Abcam), rabbit anti-Panx1 (1:2000 for Western blotting, 91137, Cell Signaling Technologies), rabbit anti-GluA1 (1:2000, 13185, Cell Signaling Technologies), rabbit anti-GluA2 (1:2000, 13604, Cell Signaling Technologies), rabbit anti-GluN1 (1:1000, 5704, Cell Signaling Technologies), rabbit anti-GluN2A (1:1000, ab169873, Abcam), rabbit anti-GluN2B (1:1000, 4207, Cell Signaling Technologies). Secondary antibodies used in this study were: Alexa Fluor® 488-conjugated AffiniPure donkey anti-rabbit IgG (1:600, 711-545-152), Alexa Fluor® 594-conjugated AffiniPure donkey anti-mouse IgG (1:600, 715-585-150), Alexa Fluor® 647-conjugated AffiniPure donkey anti-mouse IgG (1:600, 715-605-150), horseradish peroxidase (HRP)-conjugated AffiniPure donkey anti-rabbit IgG (1:4,000 - 1:8,000; 711-035-152), HRP-conjugated

AffiniPure donkey anti-mouse IgG (1:4,000 – 1:8,000; 715-035-150), HRP-conjugated AffiniPure donkey anti-rat (1:4,000 – 1:8,000; 712-035-150). All secondary antibodies were obtained from Jackson ImmunoResearch.

2.4.2 Experimental animals

All animal procedures were performed in accordance with guidelines by the and the Canadian Council on Animal Care and approved by the University of Victoria Animal Care Committee. Male and female mice from postnatal day zero (P0) to P30 (note that P29 and P30 mice were both labelled as P29) were used in this study. Global *Panx1* KO and *Panx1*$^{f/f}$ strains were derived from a strain originally generated by Dr. Valery Shestopalov (Dvoriantchikova et al., 2012) and now also available from the Jackson Laboratory (#026021). Note that the original *Panx1*$^{f/f}$ 129 strain carried a caspase 4 deletion (Vanden Berghe et al., 2015). These mice have been back-crossed in-house onto C57BL/6J at least 6 times. Wildtype (WT), *Panx1* KO, *Panx1*$^{f/f}$, and *Emx1*$^{IRES\text{-}Cre}$*;Panx1*$^{f/f}$ (cKO^{E}) are on a C57BL/6J background (#000664, the Jackson Laboratory). *Panx1* KO mice used for dendritic spine analysis were generated from *Panx1*$^{+/-}$ breeding pairs (to obtain WT and KO littermates). For conditional KO experiments, breeding pairs consisting of a *Panx1*$^{f/f}$ male and an *Emx1*$^{IRES\text{-}Cre}$*;Panx1*$^{f/f}$ female were used to generate *Panx1*$^{f/f}$ and *Emx1*$^{IRES\text{-}Cre}$*;Panx1*$^{f/f}$ littermates. The *Emx1*$^{IRES\text{-}Cre}$ strain was obtained from the Jackson Laboratory (#005628). Mice were housed under a 12 hours light/dark cycle starting at 8 am, with food and water *ad libitum*; temperature was maintained between 20-25 °C and humidity at 40% - 65%. All animals were weaned at P21 and housed in an enriched environment consisting of crinkle paper, nestlets, one paper hut, and one mouse igloo or mouse tunnel.

2.4.3 Genotyping

Primers for LoxTG-F, LoxTG-R, and *Panx1* Lox-R (CTTTGGCATTTTCCCAGTGT, CGCGGTTGTAGACTTTGTCA, and GTCCCTACAGGAGGCACTGA) were used to genotype mice. Identification of mice carrying the $Emx1^{IRES\text{-}Cre}$ transgene was determined using the primers *Emx1*-WT-F, *Emx1*-WT-R, Generic-Cre-F, and Generic-Cre-R (AAGGTGTGGTTCCAG AATCG, CTCTCCACCAGAAGGCTGAG, GCGGTCTGGCAGTAAAAACTATC, GTGAAA CAGCATTGCTGTCACTT). Genomic DNA was extracted from tail clips or ear notches using MyTaq™ Extract-PCR Kit (BIO-21126, Bioline). PCR of DNA from homozygous WT mice amplifies a single 585 bp band, whereas PCR of DNA from homozygous mutant mice have a single 900 bp band, with both bands apparent in PCR samples run using DNA from heterozygous mice; PCR of DNA from $Panx1^{f/f}$ mice have a single 1898 bp band (Dvoriantchikova et al., 2012). PCR of DNA from mice carrying a single copy of $Emx1^{IRES\text{-}Cre}$ transgene have both a 378 bp band (WT) and a 102 bp band (Cre), whereas PCR of DNA from those not carrying the $Emx1^{IRES\text{-}Cre}$ transgene have a single 378 bp band.

2.4.4 Tissue processing and diolistic labelling

Experiments were performed similar to previously described (Brusco et al., 2010; Staffend and Meisel, 2011). Mice were perfused transcardially with 0.1 M PBS followed by 1.5% paraformaldehyde (PFA) in 0.1 M PBS for 30-60 seconds. The dissected brains were immersed in 1.5% paraformaldehyde for 60 minutes and then transferred to 0.1 M PBS. DiI (1,1′-Dioctadecyl-3,3,3′,3′-tetramethylindocarbocyanine perchlorate; 42364 Millipore-Sigma) crystals were placed on the dorsolateral surface of the brains and incubated overnight at 37°C in 1.5% PFA. The tissue was fixed with 4% PFA for 30

minutes at room temperature (RT), followed by 3 washes with 0.1 M PBS and coronally-sectioned on a vibratome (150 µm). Hoechst 33342 (1:500 in 0.1 M PBS, Thermo-Fisher) was used as a nuclear counterstain.

2.4.5 Dendritic spine analysis in brain sections

Note that imaging and analysis were performed blind to the genotype of the groups. High resolution 1498 X 1498 image stacks (75.94 nm/pixel; 0.5 µm z-steps) were captured using a Leica SP8 confocal microscope with 561 nm laser illumination and a 40X/1.30NA oil objective and 2.6X digital zoom. The laser power and gain were manually adjusted to prevent oversaturation of pixel intensity values in the apical dendrite. The analysis was carried out with NIH Image J v.148 (Schneider et al., 2012, https://imagej.nih.gov/ij/) and was restricted to primary apical dendrites on their trajectory through Layers 2/3. Apical shafts were selected for analysis according to the following criteria: 1) The diolistic label reached the soma of a layer 5 pyramidal cell, and 2) the shaft measured 2-4 µm wide, and 3) at least 100 µm of the shaft was clearly discernible from surrounding cells/shafts. Spines were manually traced through z-sections from the head to their origin on the shaft, considering the following: i) they protruded from the shaft by at least 0.4 µm and ii) they were separated by at least 4 µm from a neighbouring apical dendrite. The spines of six apical dendrites that matched these criteria were analyzed for each animal. The spine density was defined as the number of spines per 10 µm and was calculated by dividing the total number of spines by the length of the apical dendrite in µm multiplied by 10. Representative images were processed uniformly with a Gaussian blur of 0.5 pixels, and uniform adjustments to levels and contrast were made using Photoshop CS6 Extended suite (Adobe Systems, Inc.).

2.4.6 Primary cortical neuron cultures

Cortices from P0 WT and *Panx1* KO pups of either sex were micro-dissected, chopped with a razor blade and incubated with papain (150 µg/L, P4762, Millipore-Sigma), dispase I (150 µg/L, D4818, Millipore-Sigma), and DNAse 1 (100 µg/L, 10104159001, Roche) for 40 minutes, followed by mechanical dissociation in DMEM/F12 medium supplemented with Neurocult™ SM1 supplement (05711, STEMCELL Technologies), and L-glutamine (200 mM, 07100, STEMCELL Technologies), and penicillin/streptomycin (P/S, 0.1 U/mL, 15140122, Gibco). Cells were plated at a density of 2.5 X 10^5 cells per cm² on poly-D-lysine (PDL) pre-coated glass coverslips (GG-12-1.5-PDL, NeuVitro) or Nunc™ LabTek™ Chamber Slide™ systems (154534PK, Thermo-Fisher) for MTT assays. The medium was replaced with Neurocult™ medium (STEMCELL Technologies, 05700) supplemented with SM1 and L-glutamine, P/S, and gentamicin (0.1 mg/mL, G1397, Millipore-Sigma). From 4 days *in vitro* (DIV) onwards, partial (half) the medium was replenished with new BrainPhys™ maturation medium (Bardy et al., 2015) supplemented with SM1 and Cytosine β-D-arabinofuranoside (ara-C, C1768, Millipore-Sigma) every third day.

2.4.7 Immunostaining and spiny protrusions analysis in cultured neurons

Primary cortical neurons were fixed in 4% EM-grade PFA solution pre-warmed to 37°C for 10 min, followed by a washed in PBS and permeabilization with 0.25% Triton X-100 in PBS (PBST) for 10 min at RT, washed again with PBS and then blocked with 10% donkey serum (DS, 017-000-121, Jackson Immunoresearch), 1% BSA, and 22.52 mg/mL glycine in PBST for 30 minutes at RT. Following blocking, cultures were incubated with primary antibodies in 1% BSA, and 5% DS in PBST overnight at 4 °C, washed in PBS

three times (10 min), and incubated with secondary antibodies and Alexa Fluor 555 phalloidin (A34055, Invitrogen) in PBST supplemented with 1% BSA, and 5% DS for 1 h at RT. After three washes (10 min), coverslips were mounted on microscope slides using Vectashield Antifade Mounting Medium (H-1000, Vectorlabs). Hoechst 33342 (H3570, Invitrogen) was used as nuclear stain. For the analysis of spiny protrusions and PSD-95+ dendritic spines, high resolution (2048 X 2048, pixel size 0.090 µm) images of neurons were captured using a Leica SP8 confocal microscope (63X/1.20NA). The same acquisition parameters were maintained for all cells across all separate cultures within an experiment. Dendritic spines were defined as actin-enriched protrusions ranging from 0.4 µm and 10 µm in length that emanated directly from the dendritic shaft. Using ImageJ, the longest dendrite of each cell was selected and defined as the primary neurite. Within the primary neurite, a 20 µm segment from the distal tip of the primary neurite was traced and dendritic spines within the segment were traced with individual ROIs; spine density was defined as the number of spines per 10 µm and was calculated by multiplying the total number of spines traced by 0.5. For cell-type characterization of neuronal cultures, coverslips were stained with the protocol described above and primary antibodies (MAP2, Gad67, and GFAP) were incubated overnight at 4 °C, followed by three 10 min washes in PBS, secondary antibody incubation at room temperature, and three more 10 min washes before mounting the coverslips with Vectashield. Images (1024 x 1024, pixel size 0.568 µm, 0.34 mm^2) were captured with a Leica SP8 confocal microscope (20X/0.7NA). The proportions of astrocytes and inhibitory cells were calculated based on GFAP and Gad67 immunoreactivity relative to the total amount of cells (MAP2-positive cells + GFAP-positive cells). The proportion of excitatory cells was determined from MAP2-

positive/Gad67-negative relative to the total amount of cells. Representative images were uniformly adjusted with Gaussian blur (2 pixels), and mild uniform adjustments to levels and contrast using Photoshop CS6 Extended suite (Adobe Systems, Inc.).

2.4.8 Neuronal network analysis in primary cortical neuron cultures

For Ca^{2+} imaging experiments, neuronal cultures 12–14 days *in vitro* were washed with HBSS and incubated in in BrainPhys™ maturation medium supplemented 4 µM Fluo-4 AM (F14201, Thermo-Fisher,) for 40 minutes at 37°C, 5% CO_2, and 95% humidity. Coverslips were washed, transferred to a 35 mm dish containing BrainPhys™ without phenol red (05791, STEMCELL Technologies), and incubated in the dark for 30 minutes at 37°C, 5% CO_2 and 95% humidity to allow complete de-esterification of the probe. The dish was then mounted onto a heated chamber held at 37°C, 5% CO2 and images were acquired every 5 seconds for 10 minutes (pixel dwell time 36 ns, streamed at 7.41 Hz, exposure/frame capture time 135 ms,; 120 frames) using a laser-scanning microscope (Leica SP8) using 471 nm laser illumination (constant 5% laser power) and a 20X objective (NA 0.70). Three fields of view (FOVs) were analyzed per coverslip. Regions of interest (ROIs) were drawn around each soma within each FOV. The raw fluorescence intensity values over time within each ROI were extracted using the Leica Application Suite Software (version 3.1.3.16308, Leica Microsystems); the background signal was determined in areas of the culture lacking neurons and was subtracted from all the intensity records; fluorescence intensity values were exported as .csv files. Two to three coverslips across 3 independent cultures were used for this analysis (WT = 8 coverslips across 3 independent cultures; KO = 7 coverslips across 3 independent cultures). Note that cells exhibiting a range in fluorescence intensity values limited to within 10% of maximal

fluorescence intensity across the entire recording (i.e. fluorescence intensity of 90% of maximum or greater) were removed from all subsequent analyses, resulting in a total of 27/1044 cells removed across WT coverslips (2.9%) and 66/1155 cells removed across *Panx1* KO coverslips (5.7%). This exclusion criteria allowed us to remove cells with abnormally high fluorescence values that could have confound our analysis; however, it might also eliminate cells with very small calcium transients, skewing our results towards more active cells. Then, the extracted .csv files were processed using the Fluorescence Single Neuron and Network Analysis Package, FluoroSNNAP (https://www.seas.upenn.edu/~molneuro/software.html, University of Pennsylvania), an open-source, interactive plugin for MATLAB (MATLAB R2014a, the Mathworks Inc.) for $\Delta F/F_0$ conversion from raw F data, spike probability inference, and network ensemble analysis. Once the raw fluorescence .csv file is imported, the analysis package generates a mock image or stack by randomly placing all the traced ROIs contained in the .csv file, which serves to interact with the imported data by selecting individual ROIs and visualizing their time-varying traces. By selecting the option "Convert raw fluorescence data to deltaF/F" the difference in fluorescence ($\Delta F/F_0$) was computed by taking the average of all the pixels within each ROI (raw fluorescence trace) and subtracting each value with the mean of the <50% values in the previous 10 frames (adjustable parameter), and then dividing that product by the mean of the lower 50% values in the previous 10 frames (Patel et al., 2015). Selection of the module "Infer underlying spike probability" calculates the spike probability of each individual ROI using a fast, non-negative deconvolution method developed by Vogelstein et al. (2010). This inferred spike probability algorithm represents neuronal activity better than $\Delta F/F$ (Vogelstein et al., 2010; Miller et al., 2014). Network

ensembles, defined as the group of co-activate neurons in a high-activity frame, were calculated by thresholding spike probability data to 3 standard deviations (SDs) above zero, determined from spike probabilities of the entire population in each FOV; this serves to identify active cells not confounded by noise. Values above the threshold were set to 1, and those below the threshold were set to 0. Then, these binary activity data were shuffled 1,000 times to identify the statistically significant number of groups of co-active neurons, using a significant level of $p<0.05$ (Miller et al., 2014). For distribution analyses the median raw Fluo-4 AM fluorescence intensity (in this case defined as baseline fluorescence) and the difference between maximum and minimum fluorescence intensity values (in this case defined as ΔF, fluorescence intensity range) across all frames were obtained for each ROI (cell) collected in the present study and plotted as relative frequency distributions. Violin plots were generated in RStudio, and distributions were compared using the non-parametric Mann-Whitney *U* test.

2.4.9 MTT cell viability assay

Cell viability was tested in WT and *Panx1* KO neuronal cultures Nunc™ LabTek™ Chamber Slide™ using the Vybrant® MTT ([3-(4,5-Dimethylthiazol-2-yl)-2,5-Diphenyltetrazolium Bromide]) cell proliferation Assay Kit (V13154, Thermo-Fisher) and following the manufacturer's instructions. Briefly, 12 mM of MTT stock solution (Component A) were prepared by adding 1 mL of PBS to a 5 mg vial of MTT; 20 µL of this 12 mM MTT solution was added to each well containing neurons bathed in 180 µ L of fresh BrainPhys™ without Phenol Red (05791, STEMCELL Technologies) and incubated for 4 hours at 37 °C and 5% CO_2; wells without neurons were used as negative controls. After this step, ¾ of the medium were removed and 100 µL of DMSO were added in,

mixing thoroughly the contents of the well and incubating for 10 minutes at 37 °C. After this, the resulting solution was mixed once again, and the absorbance was read at 540 nm using a microplate reader (Infinite®PRO microplate reader, Tecan Life Sciences). All absorbance values represent the average of 9 scans per well and were normalized to blank wells (wells without neurons). Six wells per culture per group were used for this assay (n = 3 per group).

2.4.10 Synaptosome preparation and Western blotting

Synaptic proteins were extracted using Syn-PER™ Synaptic Protein Extraction Reagent (87793, Thermo-Fisher) according to the manufacturer's instructions. Briefly, WT and *Panx1* KO P14 and P29 cortices were dissected and weighed and then submerged in ice-cold Syn-PER reagent (1 mL/100 mg) supplemented with protease inhibitor cocktail (P8340, Milipore-Sigma). After homogenization on ice, 10%-20% of the homogenate was stored at -80°C for future analysis; the remaining of the homogenate was centrifuged at 1200 X g for 10 minutes at 4°C. The pellet was discarded, and the supernatant transferred to a new tube, for a new round of centrifugation at 15,000 X g for 20 minutes at 4°C, obtaining synaptosomes. This pellet was resuspended in Syn-PER™ reagent using 150 µL per 100 mg of brain tissue. This synaptosome suspension was stored in 5% (v/v) DMSO at -80°C until analysis. On the day of analysis, 50 µL of the synaptosome suspension was placed in a new tube and centrifuged to collect the pellet. Protein was extracted by adding 200 µL of PBS-based RIPA lysis buffer (1% IGEPAL, 0.5% sodium deoxycholate, 0.1% SDS, supplemented with PI cocktail, PMSF and Na orthovanadate) and immersion in ice for 30 minutes. Samples were heated to 95-100°C for 10 minutes in Laemmli sample buffer, DTT and β−ME before loading 10 µg of protein per lane onto 10% PAGE gels

(TGX Stain-Free FastCast Acrylamide Kit 161-0183, Bio-Rad) and protein separation was achieved by application of 200 V. Following electrophoresis, gels were exposed to 30 s UV (G-box imager) to obtain the Stain-Free signal (total protein) and then transferred to polyvinyldene fluoride (PVDF) for 1 hour at 100 V. Following this, the Stain-free signal was captured by UV light (5 s), rinsed with deionized water for 30 s, blocked in 5% skim milk in PBS supplemented with 0.1% Tween 20, incubated with primary antibodies at 4°C overnight, and secondary antibodies for 1 h at RT after three washes in PBST. The immunoreactive bands were visualized by enhanced chemiluminescence and quantified using ImageJ (http://imagej.nih.gov/ij/). To determine the cortical specificity and extent of *Panx1* KO of the excitatory-specific *Panx1* KO model (*Panx1* cKO^{E}), we made whole lysates from the cortices and cerebelli of *Panx1*$^{f/f}$ and *Panx1* cKO^{E} littermates using PBS-based RIPA lysis buffer and processed as described above.

2.4.11 Experimental Design and Statistical Analysis

For *ex vivo* analysis (diolistic labeling of dendritic spines) WT and *Panx1* KO groups consisted of equal numbers of male and female mice. Note that separate analyses of male and female groups revealed no sex-specific differences in the overall effects and so the sexes were combined. For *in vitro* experiments, appropriate controls are clearly identified in detail in the figures and figure legends. Treatment timelines and all other relevant details are described in the results and figure legends and where appropriate, illustrated on the figures themselves. Researchers were blinded to the identity of the treatment/experimental groups at all stages of the analysis, except for Western blot analysis. Data are presented as means ± SEM. Significance comparisons were calculated using unpaired Student *t*-test, one-way ANOVA and two-way ANOVA for grouped analyses. Bonferroni's correction

was used for multiple comparisons when appropriate. When interactions were statistically significant while using two-way ANOVA for grouped analysis, a simple effect ANOVA with multiple comparison were performed using Bonferroni's correction. For non-normally distributed data we used non-parametric tests. Details of normality tests can be found in Table 1. Statistical significance was determined by a p value <0.05 in all tests used in the present study. Data was analyzed using GraphPad Prism version 6.0d (GraphPad Software, San Diego, CA), and RStudio (version 1.1.463, RStudio Inc). Significance is denoted as $p< 0.05$ (*), $p < 0.01$ (**), $p < 0.001$ (***), $p < 0.0001$ (****). Results of statistical tests are described in detail in the **Table 2.1 Statistical Table**; superscript letters throughout the results section and figure legends indicate the corresponding statistic in the table.

2.4.11.1 Table 2.1. Statistical table

Table 1. Statistical table

	Fig.	Comparison	Data Structure (Shapiro-Wilk normality test unless otherwise stated)	Type of test	Statistic	Confidence, 95% CI
a1	1B(i)	WT *vs. Panx1* KO	Normal distribution	Unpaired two-tailed *t* test	t = 4.051; df = 13	p = 0.0014; 1.667 to 5.476
a2	1B(i)	WT *vs. Panx1* KO	Normal distribution (D'Agostino-Pearson Normality Test chosen due to multiple identical values)	Unpaired two-tailed *t* test	i = 4.374; df=39	p < 0.0001; 1.894 to 5.153
b1	1C(i)	WT *vs. Panx1* KO	Normal distribution (D'Agostino-Pearson Normality Test chosen due to multiple identical values)	Unpaired two-tailed *t* test	t = 2.844; df = 39	p = 0.0071; 0.4654 to 2.758
b2	1C(ii)	WT *vs. Panx1* KO	Normal distribution	Unpaired two-tailed *t* test	t = 1.320; df = 30	p = 0.1968; -0.3101 to 1.443
c	1D	WT *vs. Panx1* KO	Not normal (p < 0.0001)	Mann-Whitney *U* test (two-tailed)	U = 316,969	p < 0.0001, 834622, 1.384e6
d	1E	WT *vs. Panx1* KO	Not normal (p < 0.0001)	Mann-Whitney *U* test (two-tailed)	U = 294,294	p < 0.0001; 811947, 1.407e6
e1	1F(ii)	WT *vs. Panx1* KO, interaction effect	Normal distribution	Two-way ANOVA	$F_{(2, 90)}$ = 3.475	p = 0.0352
e2	1F(ii)	WT *vs. Panx1* KO, cell-type effect	Normal distribution	Two-way ANOVA	$F_{(2, 90)}$ = 2615	p < 0.0001
e3	1F(ii)	WT *vs. Panx1* KO, genotype effect	Normal distribution	Two-way ANOVA	$F_{(1, 90)}$ = 4.934e-008	p = 0.9998
e4	1F(ii)	WT *vs. Panx1* KO, excitatory neurons	Normal distribution	Two-way ANOVA with Bonferroni's correction		p = 0.9702, -2.347 to 5.568

e5	1F(ii)	WT *vs. Panx1* KO, inhibitory neurons	Normal distribution	Two-way ANOVA with Bonferroni's correction		$p = 0.7500$, -2.079 to 5.835
e6	1F(ii)	WT *vs. Panx1* KO, astrocytes	Normal distribution	Two-way ANOVA with Bonferroni's correction		$p = 0.1026$, -7.445 to 0.4690
e7	1F(ii)	WT *vs. Panx1* KO	Normal distribution	Simple effect ANOVA‡	$F_{(5, 90)} = 1047$	$p < 0.0001$
e8	1F(ii)	WT *vs. Panx1* KO, excitatory neurons	Normal distribution	Simple effect ANOVA‡ with Bonferroni's correction		$p = 0.9702$, -2.347 to 5.568
e9	1F(ii)	WT *vs. Panx1* KO, inhibitory neurons	Normal distribution	Simple effect ANOVA‡ with Bonferroni's correction		$p = 0.7500$, -2.079 to 5.835
e10	1F(ii)	WT *vs. Panx1* KO, astrocytes	Normal distribution	Simple effect ANOVA‡ with Bonferroni's correction		$p = 0.1026$, -7.445 to 0.4690
f	1G	WT *vs. Panx1* KO Formazan absorbance (MTT conversion to formazan)	Normal distribution	Unpaired two-tailed *t* test	$t = 0.128$ df = 4	$p = 0.9089$, -25.76 to 23.59
g1	2A(iii)	PSD-95 & Panx1 expression in Homogenate (H) *vs.* Synaptosome (P3) content interaction	Normal distribution	Two-way ANOVA	$F_{(1, 8)} = 9.847$	$p = 0.0138$
g2	2A(iii)	PSD-95 & Panx1 expression effect	Normal distribution	Two-way ANOVA	$F_{(1, 8)} = 9.847$	$p = 0.0138$
g3	2A(iii)	H *vs.* P3 content effect	Normal distribution	Two-way ANOVA	$F_{(1, 8)} = 74.46$	$p < 0.0001$
g4	2A(iii)	PSD-95 expression in H *vs.* P3	Normal distribution	Two-way ANOVA with Bonferroni's correction		$p < 0.0001$; -358.0 to -180.1
g5	2A(iii)	Panx1 expression in H *vs.* P3	Normal distribution	Two-way ANOVA with Bonferroni's correction		$p = 0.0093$; -214.5 to -36.58
g6	2A(iii)	PSD-95 & Panx1 expression in H *vs.* P3	Normal distribution	Simple effect ANOVA‡	$F_{(3, 8)} = 31.38$	$p < 0.0001$
g7	2A(iii)	Panx1 expression in H *vs.* P3	Normal distribution	Simple effect ANOVA‡ with Bonferroni's correction		$p < 0.0001$; -214.5 to -36.58
g8	2A(iii)	PSD-95 & Panx1 expression in H & P3	Normal distribution	Simple effect ANOVA‡ with Bonferroni's correction		$p = 0.0093$; -358.0 to -180.1
h1	2B(iii)	Panx1 expression P7-P63	Normal distribution	One-way ANOVA	$F_{(3, 8)} = 365.9$	$p < 0.0001$
h2	2B(iii)	Panx1 expression P7-14	Normal distribution	One-way ANOVA with Bonferroni's correction		$p < 0.0001$; 0.6377 to 0.8563
h3	2B(iii)	Panx1 expression P14-P29	Normal distribution	One-way ANOVA with Bonferroni's correction		$p = 0.0006$; 0.1161 to 0.3218
h4	2B(iii)	Panx1 expression P29-P63	Normal distribution	One-way ANOVA with Bonferroni's correction		$p = 0.9604$; -0.08815 to 0.1304
i1	3B	Panx1 expression WT *vs.* KO (genotype) by age interaction	Normal distribution	Two-way ANOVA	$F_{(1, 16)} = 84.46$	$p < 0.0001$
i2	3B	Genotype effect	Normal distribution	Two-way ANOVA	$F_{(1, 16)} = 144.7$	$p < 0.0001$

i3	3B	Age effect	Normal distribution	Two-way ANOVA	$F_{(1, 16)} = 84.46$	$p < 0.0001$
i4	3B	Panx1 expression WT P14 *vs.* WT P29	Normal distribution	Two-way ANOVA with Bonferroni's correction		$p < 0.0001$; 70.14 to 103.1
i5	3B	Panx1 expression KO P14 *vs.* KO P29	Normal distribution	Two-way ANOVA with Bonferroni's correction		$p = >$ 0.9999; -16.48 to 16.48
i6	3B	Panx1 expression WT P14-29 & KO P14-29	Normal distribution	Simple effect ANOVA‡	$F_{(3, 16)} = 104.5$	$p < 0.0001$
i7	3B	Panx1 expression WT P14 *vs.* WT P29	Normal distribution	Simple effect ANOVA‡ with Bonferroni's correction		$p < 0.0001$, 67.87 to 105.4
i8	3B	Panx1 expression WT P14 % KO 14	Normal distribution	Simple effect ANOVA‡ with Bonferroni's correction		$p < 0.0001$; 81.25 to 118.7
i9	3B	Panx1 expression WT 29 *vs.* KO P29	Normal distribution	Simple effect ANOVA‡ with Bonferroni's correction		$p = 0.2476$; -5.369 to 32.13
i10	3B	Panx1 expression KO P14 *vs.* KO P29	Normal distribution	Simple effect ANOVA‡ with Bonferroni's correction		$p > 0.9999$; -18.75 to 18.75
j1	3B	PSD-95 expression WT *vs.* KO (genotype) by age interaction	Normal distribution	Two-way ANOVA	$F_{(1, 16)} = 4.208$	$p = 0.0570$
j2	3B	Genotype effect	Normal distribution	Two-way ANOVA	$F_{(1, 16)} = 37.42$	$p < 0.0001$
j3	3B	Age effect	Normal distribution	Two-way ANOVA	$F_{(1, 16)} = 175.8$	$p < 0.0001$
j4	3B	PSD-95, WT P14 *vs.* KO P14	Normal distribution	Two-way ANOVA with Bonferroni's correction		$p < 0.0001$; -113.1 to -45.30
j5	3B	PSD-95, WT P29 *vs.* KO P29	Normal distribution	Two-way ANOVA with Bonferroni's correction		$p = 0.0220$; -73.34 to -5.516
k1	3B	GluA1 expression WT *vs.* KO (genotype) by age interaction	Normal distribution	Two-way ANOVA	$F_{(1, 16)} = 0.1996$	$p = 0.6611$
k2	3B	Genotype effect	Normal distribution	Two-way ANOVA	$F_{(1, 16)} = 9.090$	$p = 0.0082$
k3	3B	Age effect	Normal distribution	Two-way ANOVA	$F_{(1, 16)} = 0.02040$	$p = 0.8882$
k4	3B	GluA1, WT P14 *vs.* KO P14	Normal distribution	Two-way ANOVA with Bonferroni's correction		$p = 0.1763$; -131.3 to 20.11
k5	3B	GluA1, WT P29 *vs.* KO P29	Normal distribution	Two-way ANOVA with Bonferroni's correction		$p = 0.0526$; -150.6 to 0.7678
l1	3B	GluA2 expression WT *vs.* KO (genotype) by age interaction	Normal distribution	Two-way ANOVA	$F_{(1, 16)} = 1.156$	$p = 0.2982$
l2	3B	Genotype effect	Normal distribution	Two-way ANOVA	$F_{(1, 16)} = 0.5621$	$p = 0.4643$
l3	3B	Age effect	Normal distribution	Two-way ANOVA	$F_{(1, 16)} = 0.1894$	$p = 0.6693$

m1	3B	GluN1 expression WT *vs.* KO (genotype) by age interaction	Normal distribution	Two-way ANOVA	$F_{(1, 16)}$ = 4.900	p = 0.0417
m2	3B	Genotype effect	Normal distribution	Two-way ANOVA	$F_{(1, 16)}$ = 0.05221	p = 0.8222
m3	3B	Age effect	Normal distribution	Two-way ANOVA	$F_{(1, 16)}$ = 19.95	p = 0.0004
m4	3B	GluN1, WT P14 *vs.* KO P14	Normal distribution	Two-way ANOVA with Bonferroni's correction		p = 0.3590; -22.63 to 6.241
m5	3B	GluN1, WT P29 *vs.* KO P29	Normal distribution	Two-way ANOVA with Bonferroni's correction		p = 0.2069; -4.355 to 24.52
m6	3B	GluN1 expression WT P14-29 & KO P14-29	Normal distribution	Simple effect ANOVA‡	$F_{(3, 16)}$ = 8.300	p = 0.0015
m7	3B	GluN1 expression WT P14-29	Normal distribution	Simple effect ANOVA‡ with Bonferroni's correction		p = 0.0009; -43.99 to -11.15
m8	3B	GluN1 expression KO P14-29	Normal distribution	Simple effect ANOVA‡ with Bonferroni's correction		p = 0.5231; -25.72 to 7.123
m9	3B	GluN1 expression WT *vs.* KO, P14	Normal distribution	Simple effect ANOVA‡ with Bonferroni's correction		p = 0.7180, -24.62 to 8.227
m10	3B	GluN1 expression WT *vs.* KO, P29	Normal distribution	Simple effect ANOVA‡ with Bonferroni's correction		p = 0.4138, -6.341 to 26.50
n1	3B	GluN2A expression WT *vs.* KO (genotype) by age interaction	Normal distribution	Two-way ANOVA	$F_{(1, 16)}$ = 0.05302	p = 0.8208
n2	3B	Genotype effect	Normal distribution	Two-way ANOVA	$F_{(1, 16)}$ = 7.892	p = 0.0126
n3	3B	Age effect	Normal distribution	Two-way ANOVA	$F_{(1, 16)}$ = 1.092	p = 0.3115
n4	3B	GluN2A, WT P14 *vs.* KO P14	Normal distribution	Two-way ANOVA with Bonferroni's correction		p = 0.1739; -159.7 to 24.14
n5	3B	GluN2A, WT P29 *vs.* KO P29	Normal distribution	Two-way ANOVA with Bonferroni's correction		p = 0.0945; -171.8 to 12.03
o1	3B	GluN2B expression WT *vs.* KO (genotype) by age interaction	Normal distribution	Two-way ANOVA	$F_{(1, 16)}$ = 3.507	p = 0.0795
o2	3B	Genotype effect	Normal distribution	Two-way ANOVA	$F_{(1, 16)}$ = 1.219	p = 0.2859
o3	3B	Age effect	Normal distribution	Two-way ANOVA	$F_{(1, 16)}$ = 4.547	p = 0.0488
o4	3B	GluN2B, WT P14 *vs.* WT P29	Normal distribution	Two-way ANOVA with Bonferroni's correction		p > 0.9999; -35.97 to 41.75
o5	3B	GluN2B, KO P14 *vs.* KO P29	Normal distribution	Two-way ANOVA with Bonferroni's correction		p = 0.0240; 5.644 to 83.37
p1	4B(i)	Spine density WT P14 *vs.* KO P14	Normal distribution	Unpaired two-tailed t test	t = 3.962; df=14	p = 0.0014; -5.368 to -1.597
p2	4B(i)	Spine length WT P14 *vs.* KO P14	Normal distribution	Unpaired two-tailed t test	t = 0.8432; df=14	p = 0.4133; -0.09070 to 0.2082

p3	4B(i)	Spine head diameter WT P14 *vs.* KO P14, total distribution	Not normal	Mann-Whitney *U* test (two-tailed)	$U = 1.474e^7$	$p = 0.0131$
p4	4B(i)	Spine head diameter WT P14 *vs.* KO P14, 25% right tail (> percentile 75)	Not normal	Mann-Whitney *U* test (two-tailed)	*U* = 931,253	$p = 0.4022$.
q1	4B(ii)	Spine density WT P29 *vs.* KO P29	Normal distribution	Unpaired two-tailed *t* test	$t = 5.754$; df=12	$p < 0.0001$; 3.279 to 7.275
q2	4B(iii)	Spine length WT P29 *vs.* KO P29	Normal distribution	Unpaired two-tailed *t* test	$t = 0.8214$; df=12	$p = 0.4274$; -0.05194 to 0.1148
r1	4B(iii)	Spine density $Panx1^{f/f}$ *vs.* Panx1 cKO^E	Normal distribution	Unpaired two-tailed *t* test	$t = 4.548$; df=4	$p = 0.0104$; 2.767 to 11.44
r2	4C(ii)	Spine length $Panx1^{f/f}$ *vs.* Panx1 cKO^E	Normal distribution	Unpaired two-tailed *t* test	t =0 .8717; df=4	$p = 0.4326$; -0.1602 to 0.3069
s1	4C(ii)	Spine density WT *vs.* KO primary cortical neurons	Normal distribution (D'Agostino-Pearson Normality Test chosen due to multiple identical values)	Unpaired two-tailed *t* test	$t = 8.336$; df=25	p <0.0001; 4.482 to 7.424
s2	4C(ii)	PSD-95+ spines WT *vs.* KO primary cortical neurons	Normal distribution (D'Agostino-Pearson Normality Test chosen due to multiple identical values)	Unpaired two-tailed *t* test	$t = 4.243$; df=25	$p = 0.0003$; 1.220 to 3.521
s3	4C(ii)	Spine Length WT *vs.* KO primary cortical neurons	Normal distribution	Unpaired two-tailed *t* test	$t = 1.302$; df=25	$p = 0.2047$; -0.4186 to 0.09428

2.5 Results

2.5.1 Increased network ensembles and altered Ca^{2+} dynamics in *Panx1* KO cortical neurons

To determine the impact of Panx1 on network connectivity, we performed Fluo-4 AM Ca^{2+} imaging in primary cortical neuron cultures from WT and *Panx1* KO mice (**Figure 2.1**). Spontaneous developing networks in cultured cortical neurons exhibit self-sustaining bursts lasting a few hundred milliseconds occurring at 0.05 Hz to 0.1 Hz between DIV8-21 (Habets et al., 1987; Murphy et al., 1992; Maeda et al., 1995; Tibau et al., 2013). Considering these characteristics and other experimental factors (minimization of phototoxicity, imaging multiple fields-of-view; FOV), we imaged DIV12-14 cultures at 0.2 Hz (pixel dwell time = 36 ns; total frame capture time = 135 ms) for 10 minutes (120 frames). To tease out the effects of *Panx1* KO on network properties we performed

computational modeling of our Ca^{2+} imaging data using the MATLAB based open-source package, FluoroSNNAP (Fluorescence Single Neuron and Network Analysis Package). FluoroSNNAP allowed us to determine the number and properties of network ensembles, which are defined as groups of neurons that undergo statistically significant co-activation. These ensembles are identified by their contribution to a so-called 'high-activity frame' characterized by a statistically significant proportion of activated neurons (Miller et al., 2014; Patel et al., 2015). Within this algorithm, statistically significant ($p < 0.05$) high activity frames are identified by comparing the mean activity level of a given frame with a computationally-derived activity threshold calculated using the inferred spike activity data of each cell permutated 1,000 times across the entirety of the recording period.

Figure 2.1*A* depicts Fluo-4 and FluoroSNNAP analyses from exemplary FOV and exemplary cells from wildtype (left side) and *Panx1* KO (right side) cortical neuron cultures. **Figure 2.1*Ai*** depicts two sequential Fluo-4 AM fluorescence frames captured from an exemplary WT FOV (left side) and an exemplary *Panx1* KO FOV (right side) cultured cortical neurons. An increase in Fluo-4 AM fluorescence intensity in exemplary WT cell #75 highlighted in 'high-activity' frame #27 (on the right) is evident upon comparison with the preceding frame (#26). Similarly, an increase in Fluo-4 fluorescence intensity in exemplary *Panx1* KO cell #85 highlighted in 'high-activity' frame #30 (on the right) is evident upon comparison with preceding frame (#29). The FluoroSNNAP-computed $\Delta F/F$ (**Figure 2.1*Ai*** middle panels) and inferred activity (**Figure 2.1*Ai*** bottom panels) of these two exemplary cells is also shown across all frames. **Figure 2.1*Aii*** depicts the percent of co-active neurons (top panels) and cell-specific spike activity (raster plot; bottom panels) across all 120 frames from the wildtype (left) and *Panx1* KO (right)

exemplary FOV. In this exemplary FOV, there are more red crosses (spikes from cells participating in a network ensemble) in the *Panx1* KO raster plot. Note that total of 27/1044 cells (2.9%) were removed from WT (2.9%) and 66/1155 cells (5.7%) were from *Panx1* KO coverslips according to our exclusion criteria (cells exhibiting sustained fluorescence intensity at 90% of maximum or greater). Consistent with this exemplary data, overall, *Panx1* KO cultures exhibited a significant increase in network ensembles (**Figure 2.1*Bi***; $p = 0.0014^{a1}$) and number of cells per ensemble (**Figure 2.1*Bii***; $p < 0.0001^{a2}$), as well as a significant increase in core ensembles (co-active groups of neurons active in more than one network ensemble; **Figure 2.1*Ci***; $p = 0.0071^{b1}$). These changes in network properties were still observed when all the above excluded cells were included. We then looked at raw fluorescence intensity values from Fluo-4 AM labeled primary cortical neurons and plotted the median (defined as baseline for this analysis) and the difference between the maximum and minimum fluorescence intensity values (ΔF, fluorescence intensity range) for each neuron recorded during our imaging sessions. *Panx1* KO neurons exhibited a significant increase in the baseline intensity of Ca^{2+} transients (**Figure 2.1*D***; $p < 0.0001^{c}$) and range of fluorescence compared to WT neurons (**Figure 2.1*E***; $p < 0.0001^{d}$). Additionally, we examined cell-type composition and cell viability. WT and *Panx1* KO DIV12-13 cortical neuron cultures were composed of highly similar percentages of excitatory neurons (~80%), inhibitory neurons (~16%), and astrocytes (2-4%; **Figure 2.1*F***; $p = 0.9702^{e4,8}$, $p = 0.7500^{e5,9}$, $p = 0.1026^{e6,10}$ respectively). The low percentage of interneurons is consistent with previous data from this developmental timepoint (Habets et al., 1987; Benson et al., 1994; Frega et al., 2014; Johnson et al., 2015). Similarly, cell viability assessed by the conversion of MTT to formazan (MTT assay) was not

significantly different between the two groups (**Figure 2.1*G***; $p = 0.9089$[f]). Taken together, these data suggest that *Panx1* KO enhances functional connectivity of developing networks cortical neurons.

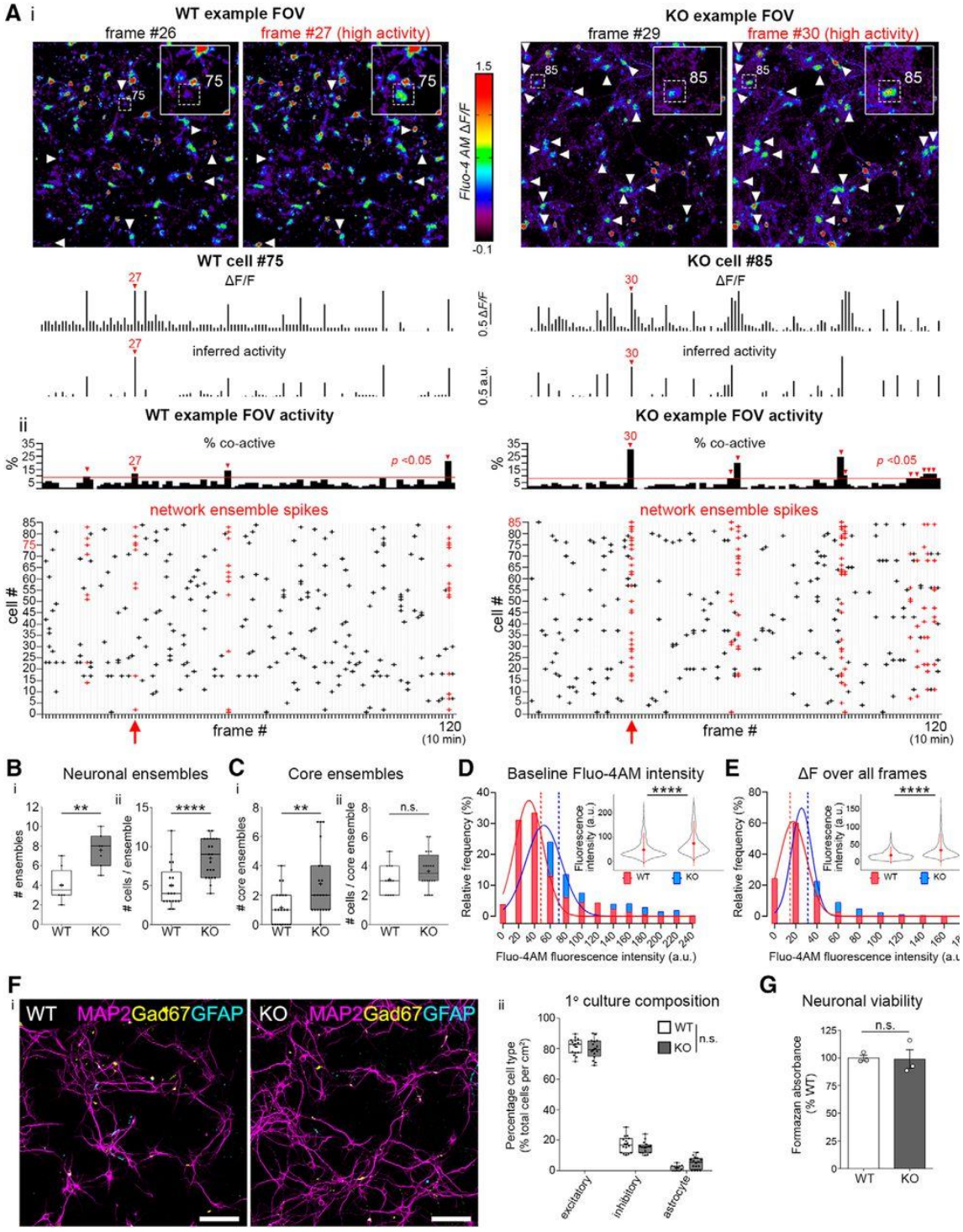

Figure 2.1. ***Increased network ensembles and altered Ca^{2+} dynamics in Panx1 KO cortical neurons***

A. Representative analyses for functional connectivity in WT and *Panx1* KO primary cortical neuron cultures. Ca^{2+} imaging data was collected using confocal microscopy in DIV12 primary cortical neurons using Fluo-4-AM. A MATLAB based program called FluoroSNNAP was used to determine network ensemble properties. ***A(i)*** Confocal micrographs of exemplary fields of view (FOVs) of WT and *Panx1* KO (labelled as KO) demonstrating Fluo-4-AM derived Ca^{2+} activity from low and high activity frames (as indicated), along with the FluoroSNNAP output $\Delta F/F$ (middle panels) *and* inferred spikes (bottom panels) from the identified WT (#75) and KO (#85) cells. ***A.(ii).*** Percentage of active neurons in each frame from the example FOVs (top panels). The red line indicates the threshold for a statistically significant number of coactive cells in a frame used by FluoroSNNAP (3 standard deviations; SD). Raster plots of WT and KO example FOVs (bottom panels) generated from thresholded spike probability data. Spikes from cells participating in a network ensemble are shown in red. The exemplary high activity frames and cells from part A are also highlighted in red. ***B.*** Network ensemble data from WT and *Panx1* KO DIV12 primary neuron cultures. ***B.(i)***. The mean number of network ensembles was increased in *Panx1* KO cultures (WT: 4.0 ± 0.6, KO: 7.6 ± 0.7 network ensembles; $t_{(13)} = 4.1$, $p = 0.0014$[a1]; n = 7-8 coverslips from 3 independent cultures; $^{**}p < 0.01$). ***B(ii).*** The number of cells involved in network ensembles was also increased in *Panx1* KO neurons (WT: 5.0 ± 0.6, KO: 8.5 ± 0.6 cell per ensemble; $t_{(13)} = 4.4$, $p < 0.0001$[a2]; n = 20-21 network ensembles from 3 independent cultures; $^{****}p < 0.0001$). ***C.*** Core network ensemble data from WT and *Panx1* KO DIV12 primary neuron cultures. ***C(i).*** The mean number of core ensembles (co-activated neurons participating in more than one ensemble) was increased in *Panx1* KO cultures (WT: 1.2 ± 0.3, KO: 2.7 ± 0.5 core ensembles; $t_{(39)} = 2.8$, $p = 0.0071$[b1]; n = 20-21 network ensembles from 3 independent cultures; $^{**}p < 0.01$). ***C(ii).*** The number of cells forming a core ensemble was not significant different between the analyzed groups (WT: 3.1 ± 0.3, KO: 3.7 ± 0.3 cells per core ensemble; $t_{(30)} = 1.3$, $p = 0.1968$[b2]; n = 12-20 core ensembles from 3 independent cultures; n.s., not significant). ***D.*** Distributions and violin plots of resting and total change (maximum minus minimum) in Fluo-4 AM fluorescence intensities in DIV12-14 primary cortical neuronal cultures. ***D(i).*** Frequency distributions of Fluo-4 AM Ca^{2+} indicator dye fluorescence intensities of WT (red) and *Panx1* KO (blue) revealed a right shift towards higher median Ca^{2+} levels at baseline (defined the as raw median fluorescence intensity value for each neuron; WT median = 37, n = 1017 cells; KO median = 58.50, n = 1089 cells; $p < 0.0001$[c]; Mann-Whitney $U = 316{,}969$; data compiled from 7-8 coverslips from 3 independent cultures per condition; $^{****}p < 0.0001$). Dotted lines represent the mean of each distribution; a.u., arbitrary units. ***E.*** Similarly, the difference between the maximum and minimum fluorescence intensity values (ΔF, fluorescence intensity range) was right-shifted and significant larger in *Panx1* KO neurons (WT median = 16, n = 1017 cells; KO median = 25, n = 1089 cells; $p < 0.0001$[d]; Mann-Whitney $U = 294{,}294$; data compiled from a total of 7-8 coverslips across 3 independent cultures per condition; $^{****}p < 0.0001$). Dotted lines represent the mean of each distribution; a.u., arbitrary units. ***F.*** WT and Panx1 KO cortical neuronal cultures have a similar cell-type composition. ***F(i).*** Representative images of WT and *Panx1* KO cortical neurons labeled

with the pan-neuronal marker MAP2, interneuron marker Gad67, and the astrocytic marker GFAP. Scale bar, 100 µm. ***F(ii).*** The proportion of excitatory neurons, inhibitory neurons, and astrocytes was similar between groups (WT excitatory neurons = 81.4% ± 1.3%, KO excitatory neurons = 79.8% ± 1.6%, p = 0.9702[e8]; WT inhibitory neurons = 17.1% ± 1.3%, KO inhibitory neurons = 15.2% ± 1.0%, p = 0.7500[e9]; WT astrocytes = 1.5% ± 0.4%, KO astrocytes = 4.9% ± 1.0%, p = 0.1026[e10], Simple effect ANOVA with Bonferroni's multiple comparison test, n = 16 FOV from 2 independent cultures; n.s., not significant). ***G.*** WT and Panx1 cortical neurons have similar cell viability. Conversion of MTT to formazan (absorbance measured at 540 nm) was not significant between groups (WT = 100% ± 2.5%, KO = 98.62% ± 8.5%; p = 0.9089[f]; $t_{(4)}$ = 0.128; n = 3 independent cultures; n.s., not significant). Data are presented as mean ± SEM.

2.5.2 Panx1 is enriched in synaptic compartments

To confirm expression of Panx1 in synaptic compartments, P14 cortical synaptosome fractions were prepared and validated by enrichment for PSD-95, and exclusion of the astrocyte protein glial fibrillary acidic protein (GFAP) by Western blotting (**Figure 2.2*A***). The synaptosome fractions demonstrated specific enrichment of Panx1 (**Figure 2.2*Aiii***; p = 0.0093[g6,8]). Western blot analysis of whole cortical lysates from WT (C57BL/6J) mice revealed a dramatic drop in Panx1 expression from P7 to P14, and further, from P14 to P29 (**Figure 2.2*Bii***; p <0.0001[g2], p = 0.0006[g3]), consistent with previous reports demonstrating peak *Panx1* transcript expression at embryonic day (E) 18 followed by a precipitous postnatal decrease (Ray et al., 2005; Vogt et al., 2005).

Figure 2.2. ***Panx1 is enriched in synaptic compartments A.*** Synaptic protein extraction and isolation revealed Panx1 enrichment in cortical synaptic compartments. ***A(i).*** Protocol for synaptosome preparation from dissected cortical tissue using SynPer™. ***A(ii).*** Western blot of subcellular fractionations obtained from a P14 WT brain and probed with PSD-95 (*top* panel), Panx1 (*second* panel), and GFAP (*third* panel), with Stain-Free (total protein) in the bottom panel, demonstrating enrichment of PSD-95 in the P3 fraction (synaptosomes) and exclusion of GFAP (*negative control*). ***A(iii).*** Quantification of Panx1 enrichment in synaptic compartments as determined by higher immunoreactivity in P3 (synaptosomes) relative to homogenate (H). As expected, PSD-95 was also enriched in P3 (Panx1, p = 0.0093[g6,8]; PSD-95, p <0.0001[g5,7]; Simple effect ANOVA with Bonferroni's multiple comparison test; n = 3 animals; **p <0.01, ****p<0.0001). ***B.*** Panx1 cortical expression is developmentally down regulated ***B(i).*** Western blot of WT

dissected whole cortical tissues from P7-P63 animals, probed with Panx1 (*top panel*), and Stain=Free (total protein) at the bottom. ***B(ii).*** Panx1 expression decreased with age (age, $F_{(3,8)} = 365.9$, $p < 0.0001$[h1]; n = 3 animals per group; ****$p<0.0001$) with levels markedly dropping from P7 to P14 ($p<0.0001$[h2]; P14-P29, $p = 0.0006$[h3]; P29-P63, $p = 0.9604$[h4]; one-way ANOVA with Bonferroni's comparison test; n = 3 animals per age group; ***$p < 0.001$; ****$p<0.0001$; n.s., not significant). Data are presented as mean ± SEM.

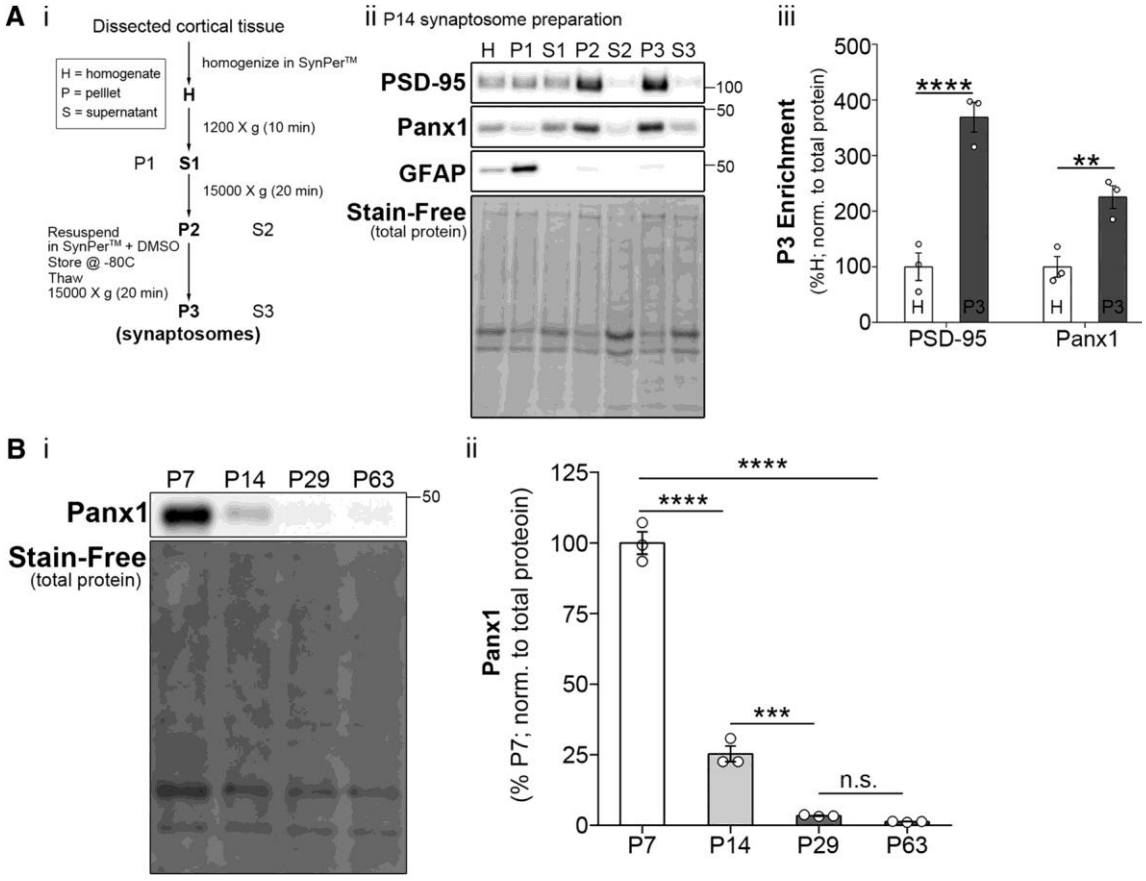

2.5.3 Increased PSD-95 and altered postsynaptic receptor expression in *Panx1* KO cortical synaptosomes

Similar to the changes observed in Panx1 expression in whole cortex lysates, Panx1 expression in cortical synaptosomes dropped markedly (~80%) between P14 and P29 (**Figure 2.3*A,B***; $p < 0.0001$[g3,4,7]). Panx1 was not detected in cortical synaptosomes from global *Panx1* KO mice (**Figure 2.3*A,B***). Consistent with the rapid development of

dendritic spines in the first month of postnatal life (Miller, 1986; Zuo et al., 2005; Romand et al., 2011), expression of PSD-95 increased significantly between P14 and P29 (**Figure 2.3*B***; $p < 0.0001^{h3}$). Somewhat unexpectedly, PSD-95 was further increased in *Panx1* KO synaptosomes relative to synaptosomes from age-matched WT controls (P14, $p < 0.0001^{h4}$; P29, $p = 0.0220^{h5}$). These changes were accompanied by significant increases in GluA1 and GluN2A in *Panx1* KO synaptosomes (**Figure 2.3*B***; $p = 0.0082^{i2}$ and $p = 0.0126^{l2}$, respectively). Interestingly, the developmental increase in GluN1 was more pronounced in WT synaptosomes ($p = 0.0009^{m7}$), whereas GluN2B levels in *Panx1* KO synaptosomes were higher at P14 and showed a more marked developmental decline at P29 ($p = 0.0488^{o3}$, $p = 0.0240^{o5}$). Because the elevated PSD-95 and altered expression of glutamate postsynaptic receptor subunits in *Panx1* KO synaptosomes could result from changes in the number of dendritic spines, we next investigated the impact of *Panx1* KO on the density of dendritic spines in cortical neurons *ex vivo*.

Figure 2.3. ***Increased PSD-95 and altered postsynaptic receptor expression in Panx1 KO cortical synaptosomes.*** ***A.*** Representative Western blots of cortical synaptosome preparations from WT and *Panx1* KO (P14 and P29) probed for Panx1, PSD-95, and glutamate postsynaptic receptor subunits (GluA1, GluA2, GluN1, GluN2A, GluN2B). The BioRad Stain-Free reagent (bottom panel) was used to quantify total protein for normalization. Molecular weight markers are indicated in kilodaltons (kDa). ***B.*** Quantification of protein expression levels of Panx1, PSD-95, and post-synaptic glutamate receptors. Expression levels for each protein were normalized to total protein and expressed as a percent of WT P14 values; n = 5 animals per group analyzed in five independent experiments. Panx1 significantly decreased from P14 to P29 in WT cortical synaptosomes (P14 = 100 ± 9.4%; P29 = 13.4 ± 1.2%, $p < 0.0001^{i3,4,7}$, simple effect ANOVA with Bonferroni's multiple comparison test; ****$p < 0.0001$). No Panx1 signal was detected in *Panx1* KO cortical synaptosomes**.** PSD-95 significantly increased with age in both WT and *Panx1* KO, and was also significantly higher in *Panx1* KO relative to WT within age-matched controls (age: $F_{(1,16)} = 37.4$, $p < 0.0001^{j3}$; genotype: $F_{(1,6} = 175.8$, $p < 0.0001^{j2}$; interaction: $F_{(1,16)} = 4.2$, $p = 0.0570^{j1}$; two-way ANOVA with Bonferroni's multiple comparison test; WT P14 = 100 ± 8.5%, KO P14 = 179.2 ± 9.1%, $p < 0.0001^{j4}$; WT P29 = 248.5 ± 9.0%, KO P29 = 287.9 ± 11.8%, $p = 0.0220^{j5}$; *$p < 0.05$, ****$p < 0.0001$). GluA1 and GluN2a also exhibited age-matched increases in expression in *Panx1* KO cortical

synaptosomes (GluA1: genotype, $F_{(1,16)}$ = 9.090, WT P14 = 100 ± 7.2%, KO P14 = 155.6 ± 24.4%; WT P29 = 93.42 ± 14.9%, KO P29 = 168.4 ± 31.7%, p = 0.0082[k2]; GluN2A: $F_{(1,16)}$ = 7.892, WT P14 = 100 ± 12.2%, KO P14 = 167.8 ± 31.20%; WT P29 = 121.4 ± 23.2%, KO P29 = 201.3 ± 33.3%,, p = 0.0126[n2]), GluN1 developmental upregulation was more pronounced in the WT group (p = 0.0009[m1-8]), whereas GluN2B immunoreactivity in *Panx1* KO synaptosomes exhibited a steeper developmental decline at P29 compared to WT (age: $F_{(1,16)}$ = 4.547, p = 0.0488[o3]; WT P14 = 100 ± 6.5%, WT P29 = 97.1 ± 16.6%, p >0.9999[o4]; KO P14 = 133.1 ± 11.9%, KO P29 = 88.6 ± 5.9%; p = 0.0014[o5]; two-way ANOVA with Bonferroni's multiple comparison test; *p<0.05). Data are presented as mean ± SEM. For additional statistical information results see **Table 2.1 Statistical Table**[i1-o5].

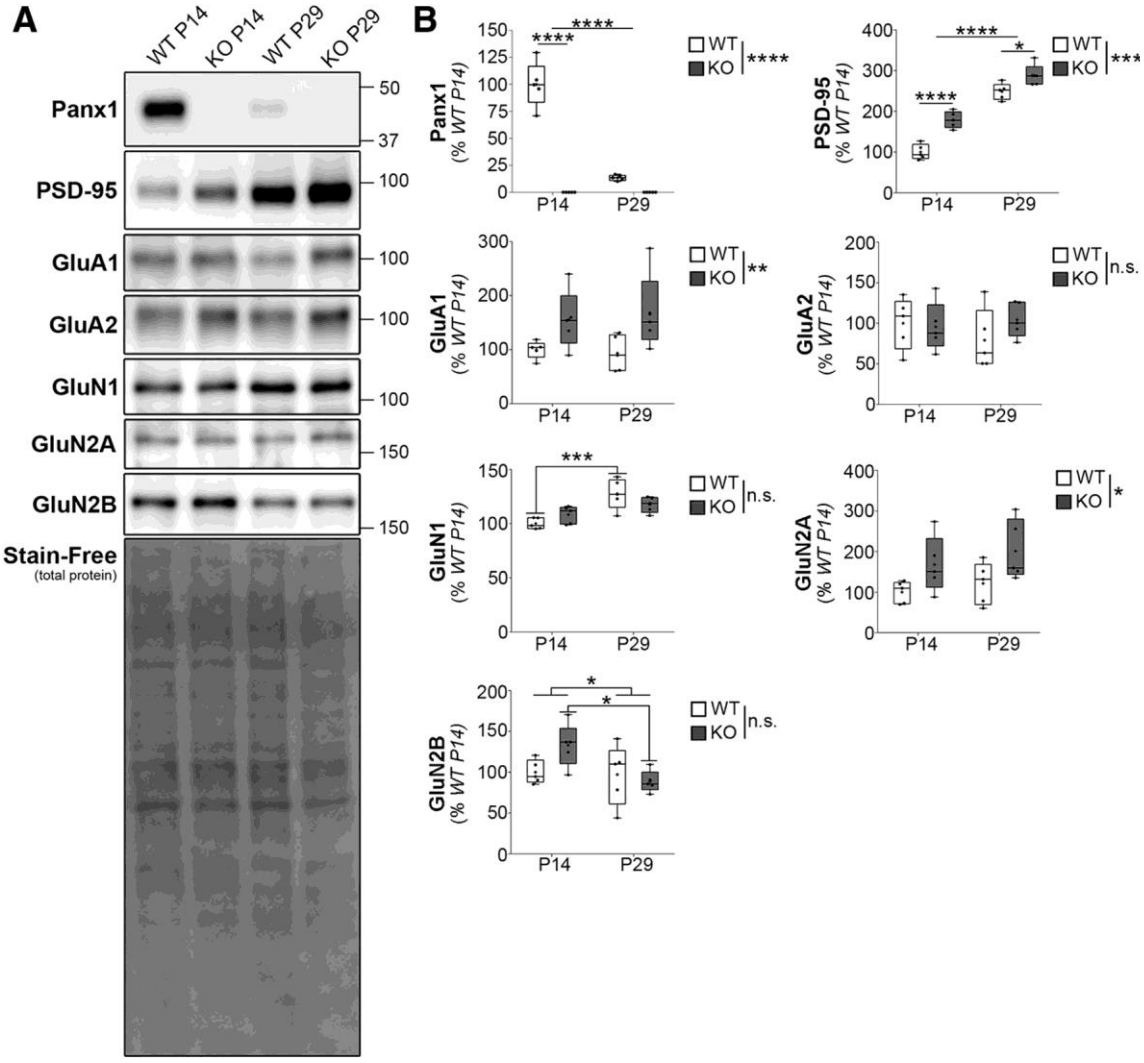

2.5.4 Increased dendritic spine densities in cortical neurons from *Panx1* KO mice

Based on our finding that synaptosomal PSD-95 expression was selectively increased in age-matched *Panx1* KO cortical synaptosomes, we tested the hypothesis that Panx1 regulates dendritic spine development. We used the fluorescent lipophilic dye, DiI (1,1′-Dioctadecyl-3,3,3′,3′-tetramethylindocarbocyanine perchlorate), which allows for relatively sparse labelling of somatosensory layer 5 pyramidal neurons (Figure 4A). As predicted, spine densities from the apical dendritic tuft of layer 5 pyramidal neurons were significantly higher in global *Panx1* KO mice than age-matched WT controls at both P14 and P29 (**Figure 2.4*Bi,Bii***; P14, $p = 0.0014^{p1}$; P29, $p < 0.0001^{q1}$). These changes were consistent with the increased synaptosome PSD-95 expression observed at P14 and P29. Next, because Panx1 has also been detected in astrocytes (Huang et al., 2007; Iglesias et al., 2009), microglia (Burma et al., 2017), and several vascular system cell types (Begandt et al., 2017) in various contexts, we also generated a conditional glutamatergic neuron-specific (*Emx-1$^{IRES\text{-}cre}$;Panx1$^{f/f}$*) *Panx1* KO (*Panx1 cKO^{E}*). Consistent with the global *Panx1* KO, spine densities in *Panx1 cKO^{E}* were significantly higher than in *Panx1$^{f/f}$* controls (**Figure 2.4*Biii***; $p = 0.0104^{r1}$). The Cre-based recombination in the Emx1-expressing lineage begins as early as E10.5 (Gorski et al., 2002). Western blot analysis (**Figure 2.4*Biv*)** of *Panx1* cKO^{E} and control (*Panx1$^{f/f}$*) cortical (Cx) and cerebellar (Cb) lysates demonstrates substantial reduction of Panx1 immunoreactivity in *Panx1* cKO^{E} cortical lysates, confirming *Panx1* KO in cortical excitatory neurons (comprising the majority of cortical tissue). Notably, mean spine lengths were not significantly different with either *Panx1* KO line, suggesting the additional spines do not represent abnormally long spines or filopodia, (Miller and Peters, 1981; Ziv and Smith, 1996; Zuo et al., 2005;

for review see Sala and Segal, 2014). *Panx1* KO primary cortical neurons grown in culture for DIV12-14 exhibited significantly higher densities of dendritic protrusions resembling dendritic spines (**Figure 2.4*C***). A similar proportion of dendritic protrusions co-localized with PSD-95 in both WT and *Panx1* KO cortical neurons and spine lengths were not significantly different between groups. Together these results suggest that deletion of *Panx1* in glutamatergic cortical neurons increases spine density in a cell-autonomous way.

Figure 2.4. ***Increased dendritic spine density in Panx1 KO cortical neurons A***. Experimental set-up for DiI labeling of apical dendrites of layer 5 somatosensory neurons *ex vivo*. On the left is a representative micrograph of a WT P14 mouse cortex labeled on the pial surface with DiI with an overlay delimiting the somatosensory cortex and cortical layers. A yellow arrow denotes the cell bodies of the layer 5 cortical neuron, shown in the inset; scale bar, 100 µm. On the right, a 100 µm segment of the primary apical dendrite of the cell in the inset, traversing layer 2/3; scale bar, 20 µm. Scale bar, 500 µm. ***B.*** Increased dendritic spine density in *Panx1* KO cortical neurons. ***B(i).*** Representative maximum intensity projections of *Panx1* WT (left) and *Panx1* KO (right) neurons at P14. Scale bar, 1 µm. Average spine density was significantly higher in *Panx1* KO (WT, 13.7 ± 0.7 spines per 10 µm; KO, 17.2 ± 0.5 spines per 10 µm, $p = 0.0014^{p1}$; $t_{(14)} = 3.9$, unpaired t-test, n = 8 animals per genotype; $^{**}p < 0.001$). Average spine length was not significantly different (WT, 1.64 ± 0.06 µm; KO, 1.58 ± 0.04 µm, $p = 0.4133^{p2}$; $t_{(14)} = 0.8$, unpaired t-test, n = 8 animals per genotype; n.s., not significant). ***B(ii)***. At P29. average spine density was significantly higher in *Panx1* KO (WT, 20.3 ± 0.5 spines per 10 µm; KO, 25.6 ± 0.8 spines per 10 µm; $t_{(12)} = 5.8$, $p < 0.0001^{q1}$, unpaired t-test, n = 7 animals per genotype; $^{****}p < 0.0001$). Average spine length was not significantly different (WT, 1.47 ± 0.01 µm; KO, 1.50 ± 0.03 µm, $p = 0.4274^{q2}$; $t_{(12)} = 0.8$, unpaired t-test, n = 8 animals per genotype; n.s., not significant). ***B(iii).*** Similarly, average spine density was significantly higher at P29 in a conditional excitatory neocortical pyramidal cell *Panx1* KO (*Emx1*$^{IRES\text{-}Cre/+}$*;Panx1*$^{f/f}$, *Panx1* cKO^{E}) when compared to *Panx1*$^{f/f}$ littermate controls (*Panx1*$^{f/f}$, 18.2 ± 1.4 spines per 10 µm; cKO^{E}, 25.3 ± 0.8 spines per 10 µm $t_{(4)} = 4.6$; $p = 0.0104^{r1}$, unpaired t-test, n = 3 mice per genotype; $^{*}p < 0.05$). Average spine length was not significantly different (*Panx1*$^{f/f}$, 1.43 ± 0.03 µm; cKO^{E}, 1.50 ± 0.08 µm, $p = 0.4326^{p2}$; $t_{(4)} = 0.9$, unpaired t-test, n = 3 animals per genotype; n.s., not significant). ***Biv***, *Top*, representative Western blot of cortical (Cx) and cerebellar (Cb) lysates from control (Panx1$^{f/f}$) and Panx1 cKO^{E} mice. *Bottom*, Genotyping results assaying for the presence of Cre and Emx1 in *Panx1*$^{f/f}$ and *Panx1* cKO^{E}. See Methods for more details.. ***C.*** Increased dendritic spine density and PSD-95-positive spine density in cultured cortical neurons at DIV12-14.***C(i)***. Representative maximum intensity projections of primary neurite (longest neurite) distal segments from WT and *Panx1* KO cultured cortical neurons. Dendritic spines were identified using fluorophore-conjugated phalloidin (F-actin; blue). PSD-95 puncta

(white) were quantified (PSD-95+ spines). Scale bar, 10 µm. ***C(ii).*** Quantification revealed increased mean spine density (WT, 10 ± 0.6 spines per 10 µm; KO, 16 ± 0.5 spines per 10 µm, $t_{(25)} = 8.4$, $p < 0.0001$[s1]; unpaired t-test, n = 10-17 cells from 3 independent cultures; ****$p<0.0001$), and increased of PSD-95-positive spines in *Panx1* KO cultured cortical neurons (WT, 1.5 ± 0.3 spines per 10 µm; KO, 3.9 ± 0.6 spines per 10 µm, $t_{(25)} = 4.2$, $p = 0.003$[s2]; unpaired t-test, n = 10-17 neurons from 3 independent cultures; ***$p<0.001$). Spine length was not different between groups ($p = 0.2047$[s3]). Data are presented as mean ± SEM.

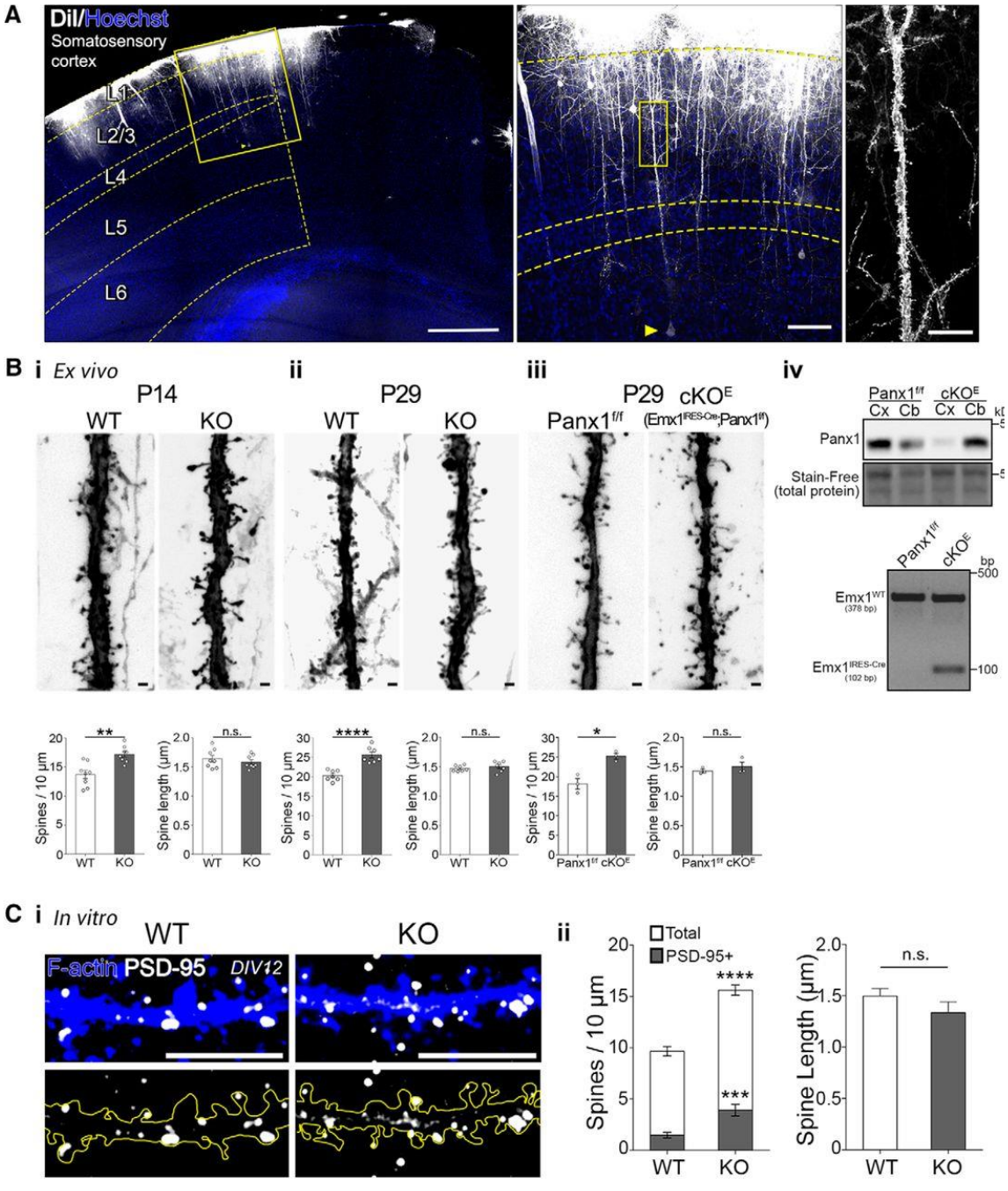

2.6 Discussion

To our knowledge, this is the first study connecting Panx1 to the structural development of dendritic spines. We observed similar spine lengths and proportions of spines expressing PSD-95 in wildtype and *Panx1* KO cortical neurons, suggesting *Panx1* KO does not simply induce a selective proliferation of immature spines, but rather increases the number of spines with very similar properties to those found in WT cortical neurons. Our results suggest that this increase in dendritic spine density underlies the larger number of network ensembles observed in *Panx1* KO cortical cultures (**Figure 2.5**). These findings are consistent with recent evidence demonstrating that incorporation of a cell into a network ensemble requires the development of spines and synapses (Jung and Herms, 2014; as reviewed in Hoshiba et al., 2017; Frank et al., 2018). While cortical cultures, in which we performed our network analysis, are known to contain abundant autaptic connections, these are also highly abundant within the developing rodent neocortex. Lübke et al. (1996) reported that autaptic contacts are found in most layer 5 cortical neurons *in situ* in the developing rat neocortex (92% of all coupled neurons; 80% of all cells analyzed). Amongst others, a recent report from Yin et al. (2018) confirmed that autapses occur in layer-5 pyramidal neurons in developing mouse prefrontal cortex and human frontal lobe (acute brain slices) that persist into adulthood, promoting neuronal responsiveness, burst firing and coincidence detection. Thus, not only might *Panx1* KO impact autapses in culture but also potentially *in vivo*. It is also important to note that our understanding of the contribution of spine development and synaptic strengthening to spontaneous network development is still relatively limited and we cannot yet determine whether the ~20-30% increases in spine density we observed *ex vivo* and *in vitro* equates directly to 20-30%

increases in the number of synapses. Finally, given that not all synapses/cells are recruited to shape the development of neuronal network ensembles, and since our current understanding of the recruitment process is limited (Hoshiba et al., 2017), in the absence of more sophisticated methodology, we are unable to predict which *Panx1* KO cells might be engaged in enhanced coupling. Moreover, rescue experiments in which Panx1 is re-expressed in control and *Panx1* KO neurons are now needed to determine whether the role of Panx1 in regulating spine formation and network ensembles is direct.

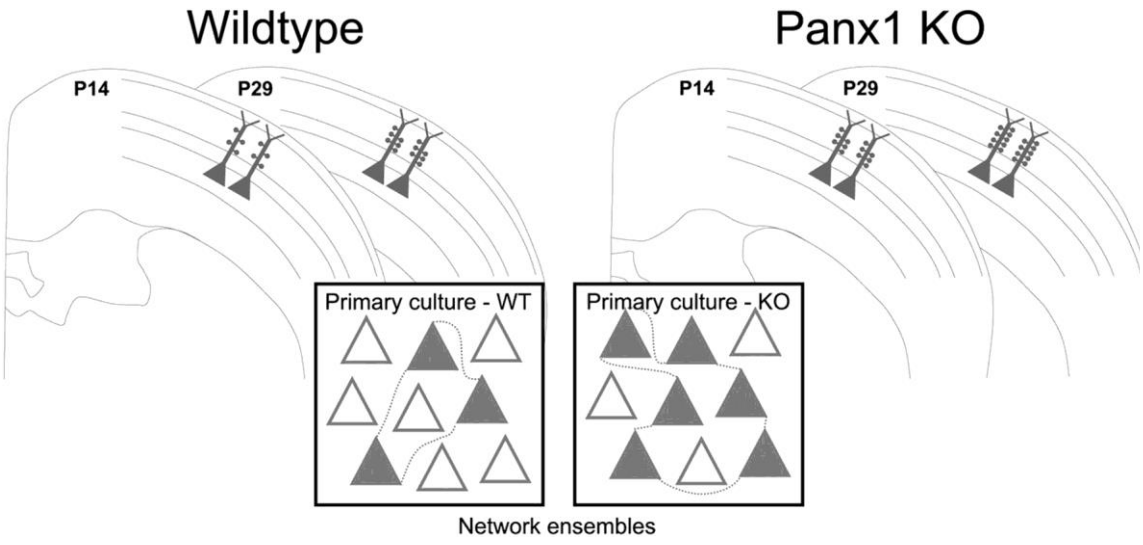

Figure 2.5. Loss of Panx1 in developing cortical neurons increases spine density and network ensembles. Dendritic spines receive the bulk of excitatory synapses in the cerebral cortex. Panx1 expression is developmentally regulated. Panx1 levels, high early in postnatal developmental, decrease progressively as neurons mature and form synapses (evidenced by increasingly PSD-95 expression with age). Analysis of Ca^{2+} transients in cultured neurons reveals that *Panx1* KO cortical cultures exhibit more, and larger, groups of activated neurons, known as network ensembles. *Panx1* KO cortical neurons exhibit increased spine densities *in vitro* and *ex vivo*. These results suggest that Panx1 acts as negative regulator of dendritic spine density in cortical neurons, impacting how neurons integrate into networks.

The current study expands on previous findings relating to synaptic plasticity in *Panx1* KO mice by focusing on a different region of the brain, the cortex, and by focus on potential developmental contributions. Previous studies focused primarily on the

hippocampal CA1 region at one month of age or older (Prochnow et al., 2012; Ardiles et al., 2014). These studies showed increased CA1 LTP (Prochnow et al., 2009; Ardiles et al., 2014) as well as a reduction in LTD (Ardiles et al., 2014) associated with *Panx1* KO; albeit, these effects were observed uniquely in adult animals (3 months for the Prochnow et al. study, 9-12 months for the Ardiles et al. study). Ardiles et al. (2014) found that hippocampal Panx1 expression levels were greatly reduced between young (one month) and older (9-12 month-old) animals, which is consistent with our findings over our earlier age range, and suggest that the decline in Panx1 levels begins in the early postnatal period and continues on with increasing age. More recent work showed that Panx1 channels are strongly active under ictal conditions in human brain cortical tissue from epilepsy patients and in the CA1 region of the hippocampus following kainic acid seizure induction (Dossi et al., 2018), suggesting that in pathological conditions Panx1 is positively correlated with excitability; although the mechanistic underpinnings, such as the possible interneuronal or glial contributions to this effect, have not yet been fully resolved. Relatedly, because Panx1 has been detected in multiple cell types and has been associated with cell death processes (reviewed in Sandilos and Bayliss, 2012; Thompson, 2015; Swayne and Boyce, 2017), we analyzed the cellular composition and viability of our cortical cultures. Wildtype and *Panx1* KO cultures were comprised of similar percentages of excitatory neurons, inhibitory neurons and astrocytes. The majority of cells in both wildtype and *Panx1* KO cultures were excitatory neurons (~80%). Inhibitory neurons, although less abundant (~16% in our cultures for both wildtype and *Panx1* KO), play an important role in shaping cortical networks (Lu et al., 2017). Panx1 has been detected in both excitatory and inhibitory neurons (Ray et al., 2005; Vogt et al., 2005; Zoidl et al., 2007), and this is consistent with

our Western blot data from *Panx1* cKO^{E} (glutamatergic-specific *Panx1* KO) and control (Panx1$^{f/f}$) lysates. Cortical control (*Panx1$^{f/f}$*) lysates exhibited a minor residual Panx1 immunoreactivity, which likely reflects expression in inhibitory neurons. While together our results suggest that the impact of *Panx1* KO on dendritic spine formation is cell-autonomous (glutamatergic neurons), a potential contribution of inhibitory neuron Panx1 to network ensemble development remains to be determined.

The mechanisms governing spine formation and plasticity are poorly understood (reviewed in Yoshihara et al., 2009; Murakoshi and Yasuda, 2012), and are developmental age- and brain region-specific, making it difficult to directly compare these previous studies with our own. For example the major chloride extruder in neurons, KCC2, differentially regulates brain-derived neurotrophic factor (BDNF)-dependent dendritic spine development in CA1 and somatosensory neurons during the first postnatal week (Awad et al., 2018). This study suggests molecular mechanisms of dendritic spine formation in different brain regions might not be completely generalizable. Moreover, mounting evidence implicates Panx1 as a possible chloride permeable channel (Ma et al., 2012; Nomura et al., 2017) and thus this differential regulation and of a chloride extruder could directly impact on Panx1 in spine formation; although it remains to be confirmed whether Panx1 channel function itself is implicated in the regulation of spine development. Further, BDNF, which regulates the brain region-specific effect of KCC2 (Awad et al., 2018), is expressed at higher levels in the hippocampus than in the cortex (Awad et al., 2018), suggesting fundamental differences in baseline levels of key molecular effectors of synaptic plasticity.

Activity-driven spine stabilization requires PSD-95 (Ehrlich et al., 2007); PSD-95 is more frequently detected at stable rather than transient synaptic contacts (Taft and Turrigiano, 2014), and its overexpression increases synaptic contact stability (El-Husseini et al., 2000). Moreover, most spines lacking a PSD do not persist >1 day, and further, a reduction in PSD-95 precedes spine loss (Cane et al., 2014). BDNF-dependent PSD-95 delivery into spines requires tubulin polymerization (Hu et al., 2011). Microtubule spine invasion is thought to be necessary for kinesin-based transport of cargo required for spine stabilization (for review, see Dent, 2017); although the mechanisms regulating this process are still relatively unknown. A recent report described an interaction between Panx1 and Crmp2 (Xu et al., 2018), a protein that regulates microtubule stabilization and elongation (Fukata et al., 2002; Niwa et al., 2017). Block of Panx1 with probenecid reduces the Panx1-Crmp2 interaction and concomitantly results in increased microtubule stability and enhance neurite outgrowth (Xu et al., 2018). Moreover, deletion of Crmp2 reduces dendritic spine density (Zhang et al., 2016). Of note, synaptosome fractions of WT and *Panx1* KO cortices at P14 and P29 exhibited similar Crmp2 protein levels (data not shown). Together these findings suggest a working model in which Panx1 sequesters Crmp2 by physical interaction until a specific cue, possibility a local elevation in extracellular ATP (Boyce et al., 2015; Boyce and Swayne, 2017), triggers Panx1 downregulation in the spine/shaft and release of Crmp2 to facilitate microtubule elongation, invasion and delivery of PSD-95 into the spine thereby facilitating associated downstream molecular events associated with spine growth and stability. The role of Panx1-interacting proteins in Panx1 regulation of spine development will be the focus of future studies.

Altogether, our novel findings presented here have implications for understanding neurodevelopment and diseases involving changes in spines. Alterations in dendritic spine densities have been described in a variety of neuropsychiatric disorders (Swann et al., 2000; Kulkarni and Firestein, 2012; Forrest et al., 2018). Of note, a recent study identified a human *PANX1* variant associated with multi-organ developmental abnormalities and marked intellectual disability (Shao et al., 2016). Moreover, single nucleotide polymorphisms affecting *Panx1* transcript levels have been implicated in ASD (Davis et al., 2012). Therefore, understanding the developmental role of Panx1 could provide important insights into variations in normal brain development as well as risk of neurodegenerative and neuropsychiatric disease.

3 Chapter 3: Panx1 regulates spiny protrusion dynamics in developing neurons

This manuscript has been posted as a preprint on the bioRxiv server

Juan C. Sanchez-Arias, Becca Candlish, and Leigh Anne Swayne (2020) ***Pannexin 1 regulates spiny protrusion dynamics in developing neurons***. *bioRxiv.* 2020.03.02.973917v2 *https://doi.org/10.1101/2020.03.02.973917*

This work was done with help of Becca Candlish who contributed to the production and maintenance of neuronal cultures for live-cell imaging experiments. Juan C. Sanchez Arias and Leigh Anne Swayne wrote the manuscript.

Note small editorial changes have been made to the version available in bioRxiv. Since "Panx1" was already define in the introduction, "Panx1" is used throughout this chapter. This work is currently under revision (with positive reviews at eNeuro #eN-NWR-0079-20) at the time of thesis submission. Ultimately, the linked to the published paper will be accessible from the bioR*x*iv document

3.1 Abstract

The integration of neurons into networks relies on the formation of dendritic spines. These specialized structures arise from dynamic filopodia-like spiny protrusions. Recently, it was discovered that cortical neurons lacking the channel protein Panx1 exhibited larger and more complicated neuronal networks, as well as, higher dendritic spine densities. Here, we expanded on those findings to investigate whether the increase in dendritic spine density associated with lack of Panx1 was due to differences in the rates of spine dynamics. Using a fluorescent membrane tag (mCherry-CD9-10) to visualize spiny protrusions in developing neurons (at 10 days-*in-vitro*, DIV10) we confirmed that lack of Panx1 leads to higher spiny protrusion density while transient transfection of Panx1 leads to decreased spiny protrusion density. To quantify the impact of Panx1 expression on spiny protrusion formation, elimination, and motility, we used live cell imaging in DIV10 neurons (1 frame

every 5 seconds for 10 minutes). We discovered, that at DIV10, loss of Panx1 stabilized spiny protrusions. Notably, re-expression of Panx1 in *Panx1* KO neurons resulted in a significant increase in spiny protrusion motility and turnover. In summary, these new data revealed that Panx1 regulates the development of dendritic spines by controlling protrusion dynamics.

3.2 Significance statement

Cells in the brain form intricate and specialized networks - *neuronal networks* - in charge of processing sensations, executing movement commands, and storing memories. To do this, brain cells extend microscopic protrusions - *spiny protrusions* - which are highly dynamic and survey the local environment to contact other cells. Those contact sites are known as synapses and undergo further stabilization and maturation establishing the function and efficiency of neuronal networks. Our work shows that removal of Panx1 increases the stability and decreases the turnover of spiny protrusion on young neurons.

3.3 Introduction

Panx1 is a four transmembrane domain protein that forms channels permeable to ion and metabolites with various activation mechanisms and diverse (patho)physiological implications (for review Boyce et al., 2018; Chiu et al., 2018). Panx1 is broadly and highly expressed in the brain during postnatal early development (Ray et al., 2005; Vogt et al., 2005) and localized and enriched in synaptic compartments (Zoidl et al., 2007; Sanchez-Arias et al., 2019).

Recent reports have implicated Panx1 in neurite outgrowth, hippocampal synaptic plasticity, and the development of neuronal networks and dendritic spines in cortical

neurons (Prochnow et al., 2012; Wicki-Stordeur and Swayne, 2013; Ardiles et al., 2014; Sanchez-Arias et al., 2019). While the behavioural features resulting from a loss of Panx1 have not been thoroughly characterized, a handful of studies have detected important phenotypes like anxiety, increased wakefulness, and spatial learning deficits (Prochnow et al., 2012; Ardiles et al., 2014; Kovalzon et al., 2017; Gajardo et al., 2018). Notably, dendritic spine development has been linked to each of these behaviours. For example, dendritic spine density is increased in various neurodevelopmental disorders in which clinical manifestations include anxiety, intellectual disability, and stereotypical movements (Phillips and Pozzo-Miller, 2015). Moreover, sleep promotes dendritic spine and spiny protrusion turnover in the cortex and hippocampus (Yang and Gan, 2012; Spano et al., 2019), which facilitates network sparsity and memory consolidation (Li et al., 2017; Frank et al., 2018). Dendritic spine-based synapses result from spiny protrusions (including dendritic filopodia) actively extending to contact presynaptic boutons during developmental excitatory synaptogenesis; upon contact, spiny protrusions stabilize and evolve into mature dendritic spines along active presynaptic boutons (Ziv and Smith, 1996; Fiala et al., 1998). These steps are critical in establishing network ensembles and Hebbian plasticity (Hoshiba et al., 2017).

In light of this evidence, we investigated the role of Panx1 in spiny protrusion dynamics in cultured primary cortical neurons at 10 days-*in-vitro* (DIV10). We first established an approach to study spiny protrusions using a fluorescent membrane tag (mCherry-CD9-10), allowing us to visualize these characteristically long and thin structures. Then, we transiently transfected WT and *Panx1* KO neuronal cultures with EGFP or Panx1EGFP (as well as mCherry-CD9-10) and analyzed spiny protrusions in

fixed and living neurons at DIV10. We confirmed that loss of Panx1 leads to higher spiny protrusion density while over-expression and rescue of Panx1 leads to decreased density. Using live cell imaging we observed increased stability and decreased turnover of spiny protrusions in *Panx1* KO neurons, while re-expression of Panx1 resulted in a significant increase in spiny protrusion motility and turnover. In summary, these new data reveal an inverse relationship between Panx1 expression and dendritic spine stability.

3.4 Materials and Methods

3.4.1 Table 3.1. Key Resources Table

Reagent or Resource	Source	Identifier	RRID
Experimental Models: Organisms/Strains			
Cortical neuron cultures from P0 C57BL/6J	The Jackson Laboratory	Cat# JAX:000664	RRID:IMSR_JAX:000664
Cortical neuron cultures from P0 *Panx1* KO on a C57BL/6J background	(Dvoriantchikova et al., 2012; Sanchez-Arias et al., 2019)	NA	NA
Recombinant DNA			
mCherry-CD9-10	Addgene	Plasmid #55013	RRID:Addgene_55013
pEGFP-N1	Clontech (Takara Bio) - discontinued	Cat# 6085-1	NA
Panx1EGFP	(Penuela et al., 2007)	NA	NA
Chemicals, Recombinant Proteins			
DMEM/F12	Thermo Fisher Scientific		NA
NeuroCult™	STEMCELL Tech.	Cat# 05713	NA
BrainPhys™	STEMCELL Tech.	Cat# 05790	NA
Neurocult™ SM1	STEMCELL Tech.	Cat# 05711	NA
GlutaMAX	Thermo Fisher Scientific	Cat# 35050061	NA
Penicillin/Streptomycin	Thermo Fisher Scientific	Cat# 15140122	NA
Gentamicin	MilliporeSigma	G1397	NA
Poly-D-lysine hydrobromide (PDL)	MilliporeSigma	P6407	NA
Dispase-1	MilliporeSigma	D4818-2MG	NA
Papain	MilliporeSigma	P4762-25MG	NA

DNAse-1	MilliporeSigma	11284932001	NA
Cytosine β-D-arabinofuranoside (ara-C)	MilliporeSigma	C1768	NA
Lipofectamine2000	Thermo Fisher Scientific	Cat# 11668027	NA
OptiMEM™ I	Thermo Fisher Scientific	Cat# 31985062	NA
Probenecid (water-soluble)	Thermo Fisher Scientific	Cat# P36400	NA
My-Taq Extract PCR Kit	Bioline	BIO-21126	NA
Vectashield	Vector Laboratories	H-1000	RRID:AB_2336789
Software and Algorithms			
FIJI (FIJI is just ImageJ)	NIH, (Schindelin et al., 2012)	NA	RRID:SCR_002285
MultiStackReg v1.45	Brad Busse (http://bradbusse.net/Multi-StackReg1.45_.jar)	NA	NA
R Project for Statistical Computing (version 3.6.2)	The R Foundation	NA	RRID:SCR_001905
Rstudio	Rstudio Inc.	NA	RRID:SCR_000432
tidyverse package for R	CRAN	NA	RRID:SCR_014601
DaBest package for R	CRAN, (Ho et al., 2019)	NA	NA
Adobe Photoshop CS6	Adobe Systems Inc.	NA	RRID:SCR_014199
Leica Application Suite Software version 3.1.3.16308	Leica Microsystems GmbH	NA	RRID:SCR_013673
Equipment			
Leica TCS SP8	Leica Microsystems GmbH	NA	NA
8-well Nunc™ Lab-Tek™ Chambered-coverglass	Thermo Fisher Scientific	155411PK	NA
PDL precoated coverslips	NeuVitro	GG-12-PDL	NA

3.4.2 Experimental animals

All animal procedures were approved by the University of Victoria Animal Care Committee and performed in accordance with the guidelines set by the Canadian Council on Animal Care. Male and female postnatal day (P)0-P1 were used in this study. C57BL/6J

mice were obtained from The Jackson Laboratory (#000664). The global *Panx1* KO strain in this study was derived from the *Panx1*^{Vsh} null mice originally generated by Dr. Valery Shestopalov (Dvoriantchikova et al., 2012). Note that this strain was developed using targeted mutagenesis on 129-embryonic stem cells (129-ESCs, 129X1/SvJ x 129S1/Sv) with C57BL/6J as the recipient strain and backcrossed for 5 generations by the original authors. Recent comparative genomic analysis revealed the original *Panx1*^{Vsh} null mice contained a loss of function passenger mutation in *Casp4* (*Casp11*), common to five 129-substrains (129X1/SvJ, 129S1/SvImJ, 129S2/SvPas, 129S6/SvEvTac and 129P3/J) and predicted to have passenger mutations in these additional genes *Mmp1a, Olfr832, Fbxl12, ENSMUSG00000095186,* and *ENSMUSG00000095891* (Vanden Berghe et al., 2015). These mice were further back-crossed in-house onto a C57BL/6J for at least 6 generations (Sanchez-Arias et al., 2019). Mice were housed under a 12 h light/dark cycle starting at 8:00 A.M., with food and water *ad libitum*; temperature was maintained between 20 and 25ºC and humidity at 40-65%.

3.4.3 Primary cortical neuron cultures and transfections

Primary cortical neuron cultures were prepared as previously described (Sanchez-Arias et al., 2019). Briefly, cortices from male and female P0 pups from timed-pregnant WT and *Panx1* KO breeding pairs were microdissected and incubated with papain, dispase-1, and DNAse-1 for 40 minutes in HBSS followed by mechanical dissociation in DMEM/F12 medium supplemented with Neurocult™ SM1, GlutaMAX, and penicillin/streptomycin (P/S). Then, 125,000 cells were plated in Nun™ Lab-Tek™ 8-well chambered coverglasses coated with PDL. After 1-2 hours after plating, the medium was replaced with Neurocult™ supplemented with Neurocult™ SM1, GlutaMAX, P/S, and gentamicin. From

4 days-*in-vitro* (DIV) onwards, partial (half) medium changes were done with BrianPhys™ maturation medium (Bardy et al., 2015); to limit proliferation of glial cells, ara-C was added to the medium at DIV4. Transfections were performed at DIV6 using Lipofectamine©2000. DNA/lipid complexes were diluted in OptiMEM-I® at ratio of 2 µg DNA:1 µL lipofectamine ratio and incubated at room temperature for 30 minutes. Then, these DNA/lipid complexes were added to cells in BrainPhys™ medium without antibiotics and incubated for 1-1.5 hours. Neurons were transfected with either pEGFP-N1 (250 ng) or Panx1EGFP (250 ng, gift from Silvia Penuela and Dale Laird). All transfections contained mCherry-CD9-10 (250 ng, was a gift from Michael Davidson; Addgene plasmid #55013; http://n2t.net/addgene:55013; RRID:Addgene_55013) to visualize neurons and spiny protrusions (**Figure 1**). All neurons in this study were used at DIV10. Neurons used for fixed quantifications were plated on PDL-coated coverslips

3.4.4 Genotyping

Primers for LoxTGF, LoxTGR, and Panx1 LoxR (CTTTGGCATTTTCCCAGTGT, CGCGGTTGTAGACTTTGTCA, and GTCCCTACAGGAGGCACTGA) were used to genotype mice as previously described (Sanchez-Arias et al., 2019). Genomic DNA was extracted from tail-clips using MyTaq™Extract PCR Kit. DNA from WT mice amplifies a single 585 bp band, whereas DNA from global *Panx1* KO mice have a single 900 bp band.

3.4.5 Imaging and analysis of spiny protrusions in live cortical neurons

Cortical neurons plated on chambered coverglasses in BrainPhys™ at 37°C and 5% CO_2 and primary and secondary dendrite segments of 67-76 µm were imaged (1024×256, pixel size: 0.06 µm) every 5 seconds for 10 minutes and 0.7 µm z-step using a Leica TSC SP8

microscope in resonant mode (8,000 Hz) with a 63× water immersion objective (1.20 NA). Images were exported to FIJI for analysis. First, the four-dimensionality (x,y,z,t) was reduced by creating maximum z projections before additional image processing and x-y drift was corrected with MultiStackReg v1.45 (developed by Brad Busse http://bradbusse.net/MultiStackReg1.45_.jar) when required. Then, images were subjected to a low-pass filter using a Gaussian blur (kernel size 2) and thresholded using the triangle method (Zack et al., 1977). From these binary images, outlines for each time frame were created and temporal colour-coded (**Figure 3*A,B***). Spiny protrusions were manually counted, and four basic characteristics were recorded: formation, elimination, lability, and motility. We defined formation as any *de novo* appearance of a spiny protrusion within the time-lapse recording; elimination was defined as the complete disappearance of a spiny protrusion. Lability was defined as spiny protrusions that were formed and eliminated within the duration of the time-lapse, typically short-lived and lasting 1-3 minutes (**Figure 3*C***). To assess spiny protrusion motility, we annotated partial extensions and partial retractions of individual spiny protrusions (**Figure 3*C***). The survival fraction of spiny protrusions was calculated by dividing the number of spiny protrusions at the end of each time-lapse (10-minute mark) by the number of spiny protrusions at the start (0-minute mark). The overall turnover rate was calculated as the net per cent gain and loss (sum of formation, elimination, and lability) of spiny protrusions divided by the number of spiny protrusions at the start of the time-lapse. Lastly, the overall movement change of spiny protrusions (Δ movement) was calculated by adding the basic dynamic characteristics (formation, elimination, lability, and motility) divided by the number of spiny protrusion at 0 min. Representative images were processed uniformly with a Gaussian blur of 0.5

pixels, and uniform adjustments to levels and contrast were made using Photoshop CS6 Extended suite (Adobe Systems Inc.).

3.4.6 Experimental design and statistical analysis

For all experiments 3 independent cultures were used. Neurons from either WT and *Panx1* KO were plated randomly in coverglasses and coverslips by one experimenter, and all transfections, imaging, and image analysis were performed blindly. Neurons with signs of blebbing or which focal planes were lost during image acquisition were excluded from analysis. Relevant details are described in *Results,* figure legends, and where appropriate, illustrated on the figures themselves. Data are presented as mean ± standard deviation. Data analysis using bootstrap estimation (5000 bootstrap resamples), determination of effect size, bias-corrected confidence intervals, and Cumming estimation plots were generated using the dabestR package for R (Bernard, 2019; Calin-Jageman and Cumming, 2019; Ho et al., 2019). Null-hypothesis significance testing was performed using R (version 3.6.2) and a p value < 0.05 was used as the significant threshold for these tests. Normality was tested using the Shapiro-Wilk test (McDonald, 2014). Group analyses for normally distributed data were performed with a two-way ANOVA coupled to multiple comparisons with Bonferroni's correction. For non-normally distributed data Kruskal-Wallis pairwise comparisons with Bonferroni's correction were used.

3.4.6.1 Table 3.2. Statistical Table

	Fig.	*Comparison*	*Effect size [95CI]*	*Pair.Comp.*	*Type of test*
a1	3.2Bi	Spiny protrusion density (# / 10 µm)			Two-way ANOVA with Bonferroni's correction
					Df | Mean^2 | F | Pr(
		WT-EGFP *vs. Panx1* KO-EGFP	2.36 [1.28; 3.54]	0.03517 *	genotype 1 9.61 2.679 0.1
		WT-EGFP *vs.* WT-Panx1EGFP	-3.24 [-4.54; -2.21]	0.00268 **	plasmid 1 252.48 70.432 2.3
		WT-EGFP *vs. Panx1* KO-Panx1EGFP	-3.72 [-5.17; -2.15]	0.00026 ***	interaction 1 22.05 6.151 0.0
		Panx1 KO-EGFP *vs. Panx1* KO-Panx1EGFP	-6.08 [-7.84; -4.51]	7.10e^{-09} ****	

a2	3.2Bii	Spiny protrusion length (µm)			Two-way ANOVA with Bonferroni's correction
		WT-EGFP *vs. Panx1* KO-EGFP	-0.13 [-0.397; 0.131]	>0.9999	
		WT-EGFP *vs.* WT-Panx1EGFP	0.105 [-0.21; 0.417]	>0.9999	
		WT-EGFP *vs. Panx1* KO-Panx1EGFP	0.031 [-0.31; 0.36]	>0.9999	
		Panx1 KO-EGFP *vs. Panx1* KO-Panx1EGFP	0.161 [-0.178; 0.53]	>0.9999	
b1	3.4Bi	Spiny protrusion formation (%)			Kruskal-Wallis chi-squared = 14.593, df = 3, p-value = 0.0022
		WT-EGFP *vs. Panx1* KO-EGFP	-3.02 [-5.39; -0.803]	0.2267	
		WT-EGFP *vs.* WT-Panx1EGFP	3.75 [-0.755; 10.3]	>0.9999	
		WT-EGFP *vs. Panx1* KO-Panx1EGFP	5.21 [1.21; 9.14]	0.2111	
		Panx1 KO-EGFP *vs. Panx1* KO-Panx1EGFP	8.23 [4.54; 11.8]	0.0028 **	
b2	3.4Bii	Spiny protrusion elimination (%)			Kruskal-Wallis chi-squared = 25.245, df = 3, p-value = 1.372e-05
		WT-EGFP *vs. Panx1* KO-EGFP	-2.57 [-5.85; -0.209]	0.62307	
		WT-EGFP *vs.* WT-Panx1EGFP	5.27 [0.455; 11.5]	0.15616	
		WT-EGFP *vs. Panx1* KO-Panx1EGFP	9.06 [4.02; 13.8]	0.00959	
		Panx1 KO-EGFP *vs. Panx1* KO-Panx1EGFP	11.6 [7.5; 15.8]	0.00024 ***	
b3	3.4Biii	Spiny protrusion lability (%)			Kruskal-Wallis chi-squared = 13.421, df = 3, p-value = 0.00381
		WT-EGFP *vs. Panx1* KO-EGFP	-1.11 [-3.17; 0.786]	>0.9999	
		WT-EGFP *vs.* WT-Panx1EGFP	2.34 [-0.966; 6.76]	>0.9999	
		WT-EGFP *vs. Panx1* KO-Panx1EGFP	6.2 [2.5; 9.81]	0.0291 **	
		Panx1 KO-EGFP *vs. Panx1* KO-Panx1EGFP	7.31 [3.92; 10.6]	0.0034 **	
b4	3.4Biv	Spiny protrusion motility (%)			Kruskal-Wallis chi-squared = 20.442, df = 3, p-value = 0.0001374
		WT-EGFP *vs. Panx1* KO-EGFP	-13.3 [-18.5; -8.42]	0.00016 ***	
		WT-EGFP *vs.* WT-Panx1EGFP	0.816 [-7.12; 9.33]	>0.9999	
		WT-EGFP *vs. Panx1* KO-Panx1EGFP	-3.1 [-9.89; 3.97]	>0.9999	
		Panx1 KO-EGFP *vs. Panx1* KO-Panx1EGFP	10.2 [4.53; 16]	0.03582 *	
c1	3.5Bi	Spiny protrusion survival fraction (%)			Kruskal-Wallis chi-squared = 24.351, df = 3, p-value = 2.11e^{-05}
		WT-EGFP *vs. Panx1* KO-EGFP	2.21 [0.0663; 5.03]	0.81748	
		WT-EGFP *vs.* WT-Panx1EGFP	-4.4 [-9.04; -0.308]	0.2034	
		WT-EGFP *vs. Panx1* KO-Panx1EGFP	-8.19 -12.3; -3.65]	0.00909 **	
		Panx1 KO-EGFP *vs. Panx1* KO-Panx1EGFP	-10.4 [-14; -6.58]	0.00028 ***	
c2	3.5Bii	Spiny protrusion turnover (%)			Kruskal-Wallis chi-squared = 19.895, df = 3, p-value = 0.0001784
		WT-EGFP *vs. Panx1* KO-EGFP	-4.48 [-7.73; -2.01]	0.0092 **	
		WT-EGFP *vs.* WT-Panx1EGFP	6.68 [0.967; 14.7]	0.5205	
		WT-EGFP *vs. Panx1* KO-Panx1EGFP	8.07 [2.84; 13]	>0.9999	
		Panx1 KO-EGFP *vs. Panx1* KO-Panx1EGFP	12.5 [8.06; 17]	0.0027 **	
c3	3.5Biii	Spiny protrusion Δ movement (%)			Kruskal-Wallis chi-squared = 28.526, df = 3, p-value = 2.816e-06
		WT-EGFP *vs. Panx1* KO-EGFP	-17.8 [-23.6; -11.9]	6.2e-^{05} ****	
		WT-EGFP *vs.* WT-Panx1EGFP	7.49 [-3.45; 20.1]	>0.9999	
		WT-EGFP *vs. Panx1* KO-Panx1EGFP	4.98 [-4.1; 13.8]	>0.9999	
		Panx1 KO-EGFP *vs. Panx1* KO-Panx1EGFP	22.8 [15; 30.4]	0.00033 ***	

	Df	Mean^2	F	Pr(
genotype	1	0.1133	0.618	0.4
plasmid	1	0.2018	1.101	0.3
interaction	1	0.0085	0.046	0.8

Fig., Figure, Pair Comp, Pairwise comparison; 95CI, 95% confidence interval Significance codes: <0.0001 '****', <0.001, '***', <0.01 '**', <0.05 '*'

3.5 Results

3.5.1 A novel approach to visualize and quantify spiny protrusions in cortical neurons

Spiny protrusions (including filopodia) are characteristically highly dynamic, thin, and long. As dendritic arbors mature, these transient structures stabilize into mature dendritic spines. Most methods used to detect these structures rely on cytoplasmic volume markers such as GFP (and its variants) or membrane-bound lipophilic dyes (DiI, DiO, etc). The former approach allows for sparse labelling but fails to fully label thin processes such a spiny protrusions (**Figure 1**), while the latter achieves clear visualization of these structures by labelling the membrane at the expense of widespread labelling (Mancuso et al., 2013). We transfected cortical neurons with the tetraspanin CD9-10 fused to a monomericred fluorescent protein mCherry (mCherry-CD9-10 was a gift from Michael Davidson, Addgene plasmid #55013), mCherry-CD9-10 facilitated detailed resolution of spiny protrusions in sparsely transfected cells (**Figure 1**).

Figure .3.1. A novel approach to visualize and quantify spiny protrusions in cortical neurons.

Representative maximum intensity projection of a dendritic segment from a neuron transfected with mCherry-CD9-10 and EGFP at DIV6 and fixed at DIV10. Thin and long spiny protrusions are more clearly visualized with mCherry CD9-10 (mid) than the cytoplasmic volume marker EGFP (bottom). Structures not clearly labeled with EGFP are denoted by "*" and those missed entirely are denoted with arrowheads. Scale bar 5 µm.

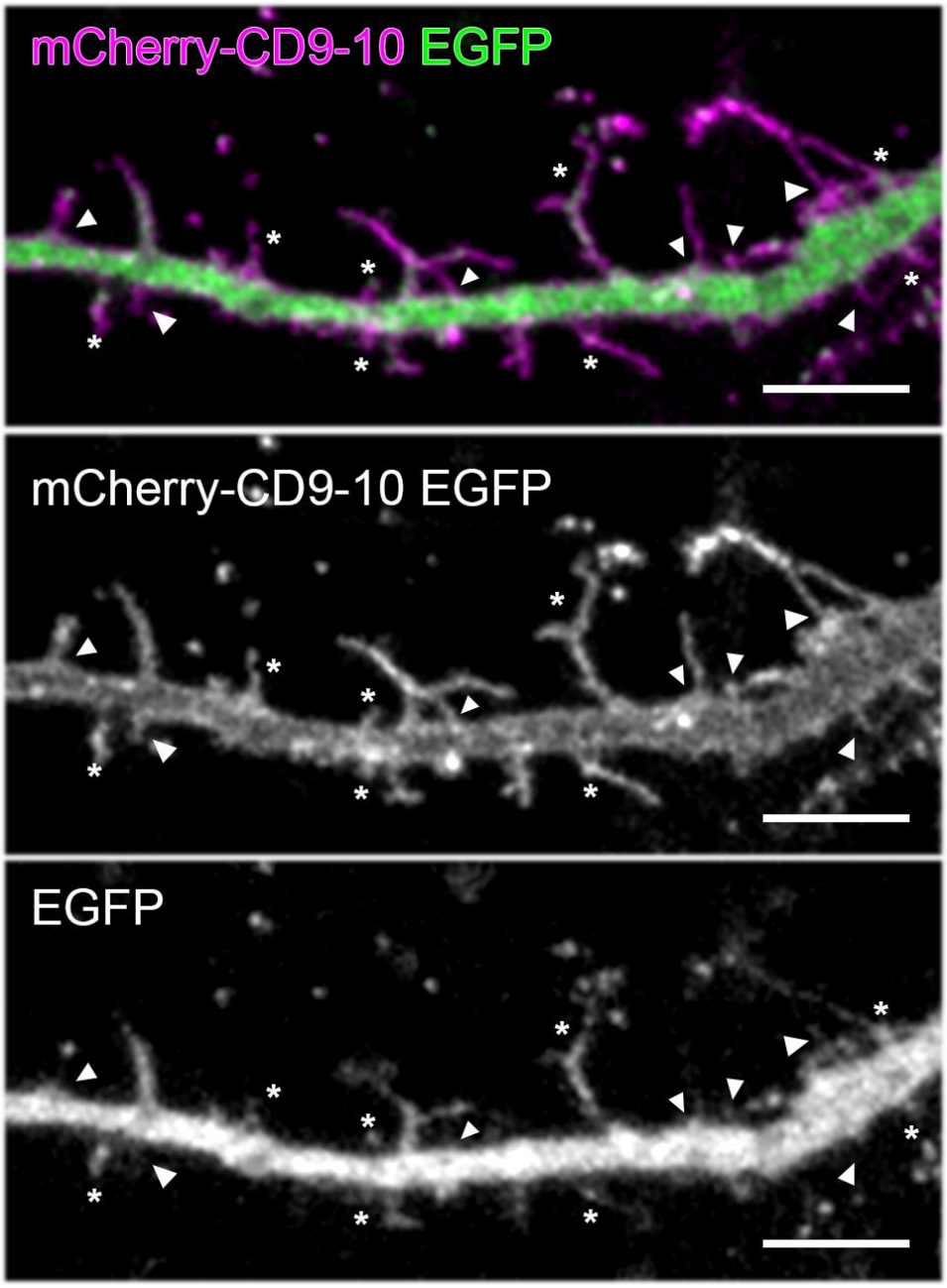

3.5.2 Transfection of Panx1 decreases spiny protrusion density in WT and *Panx1* KO DIV10 neurons

To investigate the impact of Panx1 expression, we transfected WT and *Panx1* KO cortical neuronal cultures with mCherry-CD9-10 as well as EGFP (control) or Panx1EGFP (over-expression/rescue) at DIV6 and fixed the cells 4 days later at DIV10 (**Figure 2*A***).

With EGFP control transfection we observed a 20% increase in spiny protrusion density in primary neurites of *Panx1* KO neurons (effect size: 2.36 [95CI 1.28; 3.54], $p = 0.03517$, [a1]). In Panx1EGFP-expressing cultures we observed a 27% decrease in spiny protrusion density in WT neurons (**Figure 2*Bi***, effect size: -3.24 [95CI -4.54; -2.21], $p = 0.00268$, [a1]) and a 42.5% density reduction in *Panx1* KO neurons (**Figure 2*Bi***, effect size: -6.08 [95CI -7.84; -4.51], $p < 0.0001$, [a1]). Spiny protrusion length was not significantly different amongst the groups (**Figure 2B*ii***, [a2]). These results suggest spiny protrusion density is inversely proportional to Panx1 expression levels.

Figure 3.2. Spiny protrusion density is inversely related to Panx1 expression levels in DIV10 neurons. ***A.*** Representative maximum intensity projections of WT and *Panx1* KO cultured cortical neurons transfected with mCherry-CD9-10 and either EGFP (***Ai***) or Panx1EGFP (***Aii***) as well as cropped images of their respective dendritic segments from a primary neurite. Scale bar: 50, and 5 µm. ***B.*** Effect of Panx1 expression in spiny protrusion density and length in developing cortical neurons transfected with mCherry-CD-9-10 and either EGFP or Panx1EGFP using Cumming estimation plots. Bi. With EGFP expression, spiny protrusion density was higher with *Panx1* KO neurons (WT-EGFP: 12.0 ± 0.3 spiny protrusions per 10 µm; *Panx1* KO EGFP: 14.4 ± 0.5 spiny protrusions per 10 µm, p = 0.03517, two-way ANOVA with Bonferroni's multiple-comparison test). With Panx1EGFP expression, spiny protrusion density was decreased in both WT and *Panx1* KO neurons (WT-Panx1EGFP: 8.8 ± 0.5 spiny protrusions per 10 µm, p = 0.00268; *Panx1* KO-Panx1EGFP: 8.3 ± 0.8 spiny protrusions per 10 µm, p < 0.0001, two-way ANOVA with Bonferroni's multiple-comparison test, a1). ***Bii***. No significant differences in spiny protrusion length were found between groups (WT-EGFP: 2.0 ± 0.3 µm; *Panx1* KO EGFP: 1.9 ± 0.4 µm, p > 0. 9999, two-way ANOVA with Bonferroni's multiple-comparison test, a2; WT-Panx1EGFP: 2.1 ± 0.1 µm; *Panx1* KO Panx1EGFP: 2.1 ± 0.2 µm, p > 0. 9999, two-way ANOVA with Bonferroni's multiple-comparison test). Data are presented as mean ± standard deviation. N = cells, all analyzed cells were obtained from 3 independent cultures. Effect sizes are reported in the main text and

Table 2. Red arrowheads on the y-axis on the bottom panel of Cumming estimation plots represent WT-EGFP means. s.p., spiny protrusion. <0.0001, '****'; <0.001, '***'; <0.01 '**'; <0.05 '*'.

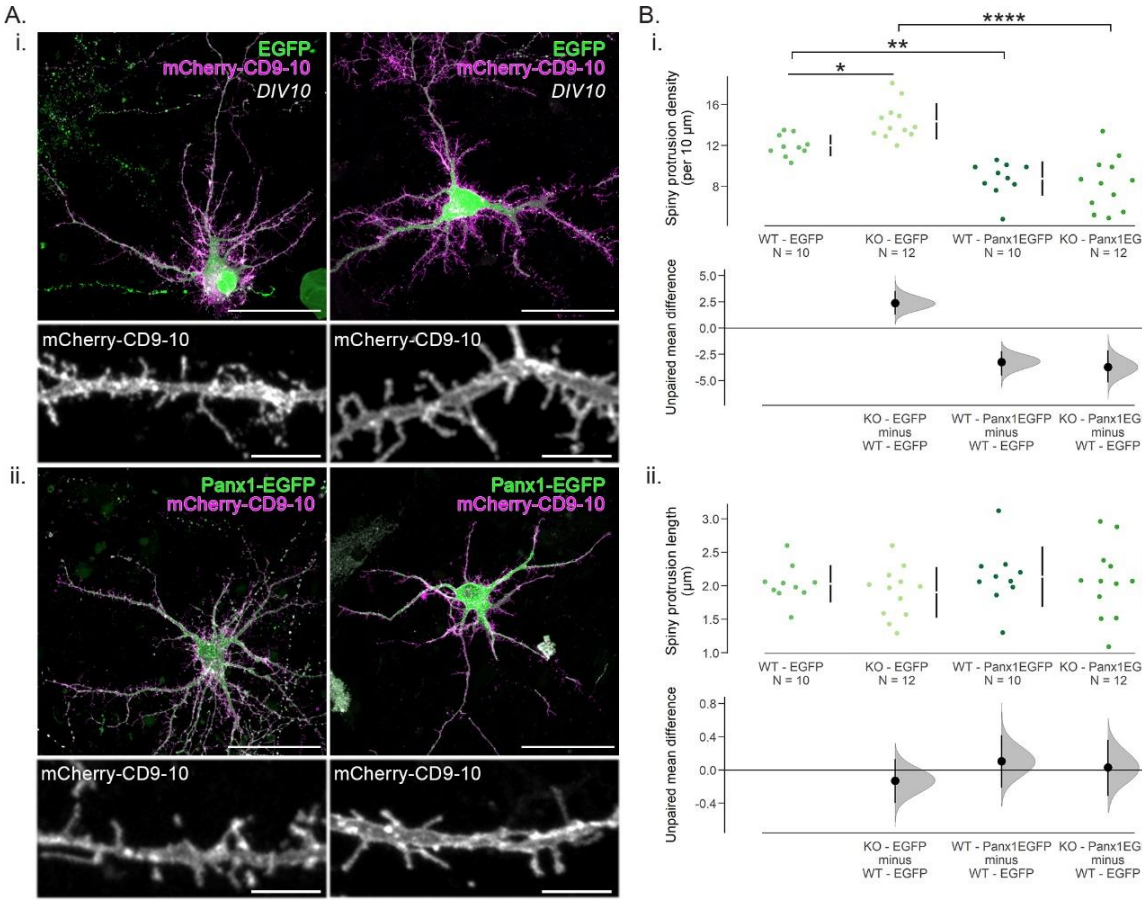

3.5.3 Measuring spiny protrusion dynamics in living neurons using a membrane marker

To investigate the mechanisms contributing to differences in spiny protrusion densities between groups, we acquired 10-minute time-lapses (one frame every 5 seconds) of primary and secondary dendrites from cortical neurons at DIV10. These cultures were transfected with mCherry-CD9-10 and either EGFP or Panx1EGFP at DIV6. At DIV10, dendrites harbour highly dynamic, thin, and long spiny protrusion that are the precursors for dendritic spines (Ziv and Smith, 1996; Fiala et al., 1998). We reduced the dimensionality of the time-lapses by creating maximum z-projections, and then images

were passed through a low-pass filter and thresholded to create outlines (**Figure 3*A***). The dendritic silhouettes (**Figure 3*B*)** were then temporally colour-coded to facilitate the detection of formation, elimination, liability, retraction, and growth of spiny protrusions (**Figure 3*C*)**.

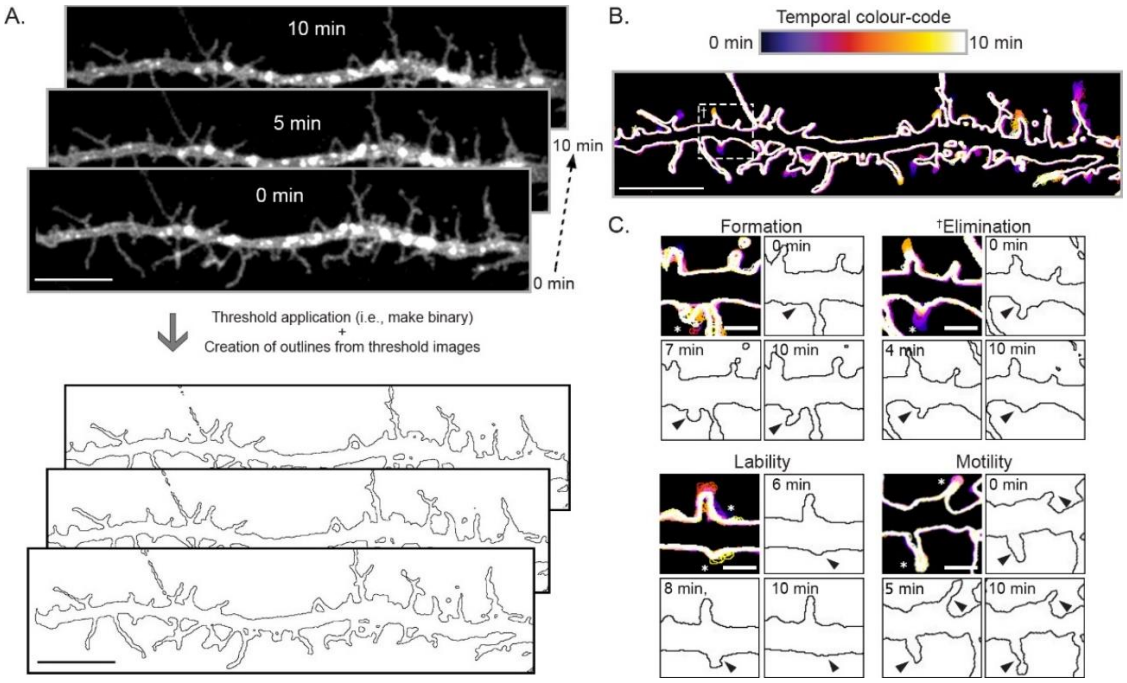

Figure 3.3. Image analysis strategy to quantify spiny protrusion dynamics in cortical cultures.
Ten minutes time-lapses were acquired by imaging dendrite segments from cortical neurons every 5 seconds. Note that this a DIV10 WT cortical neuron transfected with mCherry-CD9-10 and Panx1EGFP; only mCherry-CD9-10 is shown. The dimensionality of these recordings was reduced by creating maximum *z*-projections. Images were thresholded to create outlines (***A***, scale bar 10 µm), which were temporally colour-coded (***B***, scale bar 10 µm), allowing the visualization of various events such as the percentage of spiny protrusion (relative to time 0) undergoing formation (*de novo* appearance), elimination (complete disappearance by the end of the time-lapse), lability (appearance and disappearance by the end of the time-lapse), and retraction/extension (incomplete shrinkage or growth to an existing protrusion) shown in (***C***, scale bar 2 µm). Note that examples in ***C*** (cropped to show highlight the event in question) come from different cultures and different genotypes all at DIV10 transfected with mCherry-CD9-10 and

either EGFP or Panx1EGFP at DIV6. The example for elimination (†) comes from the neurite in **B**. Data in ***Figure 4*** includes quantification of these examples. See Methods for further details.

3.5.4 Basic characteristics of spiny protrusion dynamics in WT and *Panx1* KO neurons at DIV10

Using the above approach, we observed that transfection of Panx1EGFP in *Panx1* KO neurons significantly increased the percentage of formation and elimination of spiny protrusions compared to EGFP transfection of *Panx1* KO neurons (**Figure 4*A* & 4*Bi-ii***, formation – effect size KO-EGFP *vs.* KO-Panx1EGFP: 8.23% [95CI 4.54%; 11.8%], $p = 0.0028$, [b1]; elimination - effect size KO-EGFP *vs.* KO-Panx1EGFP: 11.6% [95CI 7.5%; 15.8%], $p = 0.00024$ [b2]), while no significant differences were observed between Panx1EGFP and EGFP transfection in WT neurons ($p > 0.9999$, [b1]). Similarly, no significant differences were observed between genotypes with EGFP (control) transfection (**Figure 4*Bi-ii***, formation – effect size WT-EGFP *vs.* KO-EGFP: -3.02% [95CI -5.39%; -0.803%], $p = 0.2267$, [b1]; elimination – effect size WT-EGFP *vs.* KO-EGFP: -2.57% [95CI -5.85%; -0.209%], $p = 0.62307$, [b2]). We next quantified spiny protrusion lability within our experimental groups. Transient expression of Panx1EGFP in *Panx1* KO neurons significantly increased spiny protrusion lability; there were no significant effects of Panx1EGFP expression in WT neurons (**Figure 4*Biii***, effect size KO-EGFP *vs.* KO-Panx1EGFP: 7.31% [95CI 3.92%; 10.6%], $p = 0.0034$; effect size WT-EGFP *vs.* WT-Panx1EGFP: 2.34% [95CI -0.966%; 6.76%], $p > 0.9999$, [b3]). There was also no significant effect of EGFP expression between WT and *Panx1* KO neurons (effect size WT-EGFP *vs.* KO-EGFP: -1.11%[95CI -3.17%; 0.786%], $p > 0.9999$, [b3]). Additionally,

within groups transiently expressing EGFP, *Panx1* KO neurons exhibited significantly reduced spiny protrusion motility (**Figure 4*Biv***, effect size WT-EGFP *vs.* KO-EGFP: -13.3% [95CI -18.5%; -8.42%], $p = 0.00016$, [b4]). Intriguingly, transient Panx1EGFP expression increased spiny protrusion motility in *Panx1* KO neurons only (effect size KO-EGFP *vs.* KO-Panx1EGFP: 10.2% [95CI 4.53%; 16%], $p = 0.03582$, [b4]). Together these results suggest that spiny protrusion dynamics roughly correlate with Panx1 expression levels.

Figure 3.4. Basic characteristics of spiny protrusion dynamics in WT and Panx1 KO neurons at DIV10. A. Representative colour-coded outlines of WT and *Panx1* KO neurons transfected with mCherry-CD9-10 and either EGFP or Panx1EGFP showing examples of spiny protrusion formation, elimination, lability, and motility events (arrowheads). These examples are cropped from the full regions of analysis from primary neurites. ***B.*** Effect of Panx1 expression on spiny protrusion formation, elimination, lability, and motility in WT and *Panx1* KO using Cumming estimation plots. ***Bi.*** Spiny protrusion formation was significantly higher in *Panx1* KO neurons transiently expressing Panx1EGFP compared to those expressing EGFP (KO-EGFP: 0.2% ± 0.1%, KO-Panx1EGFP: 4.6% ± 1.3%, $p = 0.0028$, Kruskal-Wallis test, [b1]). No significant differences were observed between genotypes in EGFP-expressing neurons (WT-EGFP: 1.7% ± 0.7%; *Panx1* KO-EGFP: 0.2% ± 0.1%, $p = 0.2267$, Kruskal-Wallis test, [b1]). ***Bii***. Similarly, only transient expression of Panx1EGFP in *Panx1* KO neurons increased spiny protrusion elimination (KO-EGFP: 0.3% ± 0.15%; KO-Panx1EGFP: 4.6% ± 1.28%, $p = 0.00024$, Kruskal-Wallis test, [b2]). No significant differences were found between WT and Panx1 EGFP-expressing cells ($p = 0.62307$, [b2]). ***Biii.*** Spiny protrusion lability was higher in *Panx1* KO neurons transfected with Panx1EGFP (KO-EGFP: 2.1% ± 0.5%; KO-Panx1EGFP: 9.4% ± 1.7%, $p = 0.0034$, Kruskal-Wallis test, [b3]), beyond that observed in WT expressing EGFP control ($p = 0.0291$, Kruskal-Wallis test, [b3]). Transient expression of Panx1EGFP in WT neurons had no significant effects ($p > 0.9999$, [b3]). ***Biv.*** Spiny protrusion motility was significantly reduced in *Panx1* KO neuron expressing EGFP control (WT-EGFP: 20.5% ± 2.3%; KO-EGFP: 7.2% ± 1.3%, $p = 0.00016$, Kruskal-Wallis test, [b4]). Transient Panx1EGFP expression increased spiny protrusion motility in *Panx1* KO neurons only (KO-Panx1EGFP: 17.4% ± 2.8%, $p = 0.03582$, Kruskal-Wallis test, [b4]). N = cells, all analyzed cells were obtained from 3 independent cultures. Effect sizes are reported in the main text and Table 3.2. Red arrowheads on the y-axis on the bottom panel of Cumming estimation plots represent WT-EGFP means. s.p., spiny protrusion; <0.001, '***'; <0.01 '**'; <0.05 '*'.

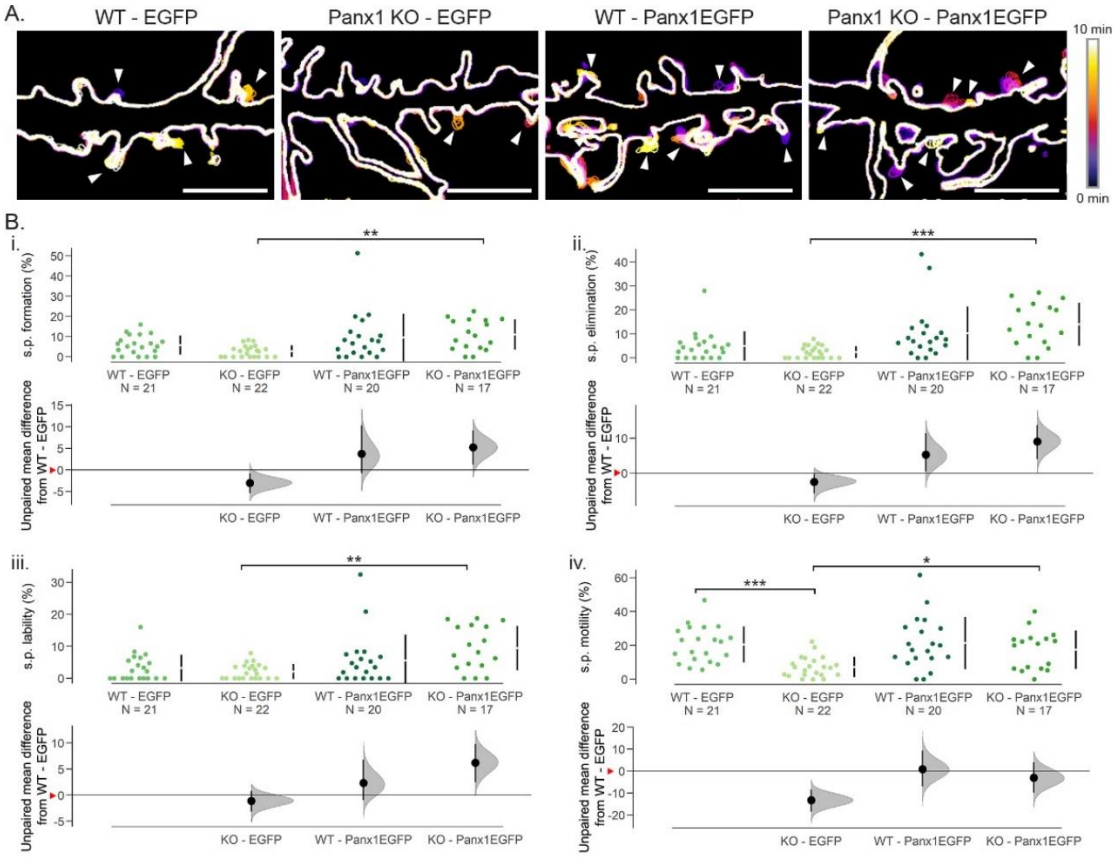

3.5.5 *Panx1* KO neuron spiny protrusions are more stable

We used the basic characteristic measurements devised in ***Figure 3C*** to calculate spiny protrusion survival fraction, turnover, and overall change in movement (Δ movement). The number of spiny protrusions persisting at the end of the analysis period relative to time 0 min, referred to as survival, was significantly reduced in Panx1EGFP expressing *Panx1* KO neurons (**Figure 5*A* & 5*Bi***, KO-EGFP *vs.* KO-Panx1EGFP: -10.4% [95CI -14%; -6.58%], $p = 0.00028$, [c1]). This reduction of survival surpassed that seen in WT, EGFP expressing cells (effect size WT-EGFP *vs.* KO-Panx1EGFP: -8.19% [95CI -12.3%; -3.65%], $p = 0.00909$, [c1]). We next calculated turnover by adding together formation, elimination, and lability, divided by the total number of spiny protrusions at time 0 min. With EGFP expression, turnover was significantly reduced in *Panx1* KO neurons (**Figure 5*Bii***,

effect size WT-EGFP *vs.* KO-EGFP: -4.48% [95CI -7.73%; -2.01%], p = 0.0092, [c2]). Within *Panx1* KO cultures transient Panx1EGFP expression significantly increased turn-over compared to EGFP control (effect size KO-EGFP *vs.* KO-Panx1EGFP: 5.24% [95CI 2.87%; 8.66%], p = 0.0027, [c2]). Finally, to measure the overall change in spiny protrusion movement (Δ movement), we calculated the sum of the four basic dynamic characteristics (formation, elimination, lability, and motility). Within EGFP expressing cells, Δ movement was significantly reduced in *Panx1* KO neurons compared to WT controls (**Figure 5*Biii panel***, effect size WT-EGFP *vs.* KO-EGFP: -17.8 [95CI -23.6; -11.9], p < 0.0001). Transient Panx1EGFP expression resulted in increased Δ movement in Panx1 KO cultures only (effect size KO-EGFP *vs.* KO-Panx1EGFP: 22.8 [95CI 15; 30.4], p = 0.00033, [c3]). Altogether, these results suggest that *Panx1* KO neuron spiny protrusions are more stable.

Figure 3.5. Panx1 KO neuron spiny protrusion are more stable. A. Representative colour-coded outlines of WT and *Panx1* KO neurons transfected with mCherry-CD9-10 and either EGFP or Panx1EGFP showing examples of spiny protrusion movement (arrowheads). These examples are cropped from the full regions of analysis from primary neurites. ***B.*** Cumming estimation plots of spiny protrusion second order metrics: survival fraction, turnover, and overall change in movement (Δ movement). ***Bi.*** Transient Panx1 expression in WT and *Panx1* KO neurons decreased the survival fraction of spiny protrusions; however, this was only statistically significant in *Panx1* KO neurons (WT-EGFP: 94.5 ± 1.2%; WT-Panx1EGFP: 91.1% ± 1.9%, p = 0.2034, [c1]; Panx1-EGFP: 97.7% ± 0.5%; *Panx1* KO-Panx1EGFP: 87.3% ± 1.9%, p = 0.00028, Kruskal-Wallis test, [c1]). ***Bii.*** In the EGFP-control-expressing group, spiny protrusion turnover was reduced in *Panx1* KO neurons (WT-EGFP: 7.5% ± 1.3; Panx1-EGFP: 3.1% ± 0.6%, p = 0.0092, Kruskal-Wallis test, [c2]). Transient expression of Panx1 significantly increased spiny protrusion turnover in *Panx1* KO neurons but not in WT neurons (WT-Panx1EGFP: 14.2% ± 3.3%, p > 0.9999; *Panx1* KO-Panx1EGFP: 15.6% ± 2.34%, p = 0.0027, Kruskal-Wallis test, [c2]). ***Biii.*** Spiny protrusion overall movement change (Δ movement) was reduced in

Panx1 KO neurons (WT-EGFP: 28% ± 2.8%; KO-EGFP: 10.3% ± 1.5%, p <0.0001, Kruskal-Wallis test, [c3]). Panx1EGFP expression increased Δ movement in both WT (WT-Panx1EGFP: 35.5% ± 5.4%) and *Panx1* KO neurons; however, this effect was only significant in *Panx1* KO neurons (KO-Panx1EGFP: 33% ± 3.8%, p = 0.00033, Kruskal-Wallis test, [c3]). N = cells, all analyzed cells were obtained from 3 independent cultures. Effect sizes are reported in the main text and Table 3.2. Red arrowheads on the y-axis on the bottom panel of Cumming estimation plots represent WT-EGFP means. s.p., spiny protrusion. <0.0001, '****'; <0.001, '***'; <0.01 '**'.

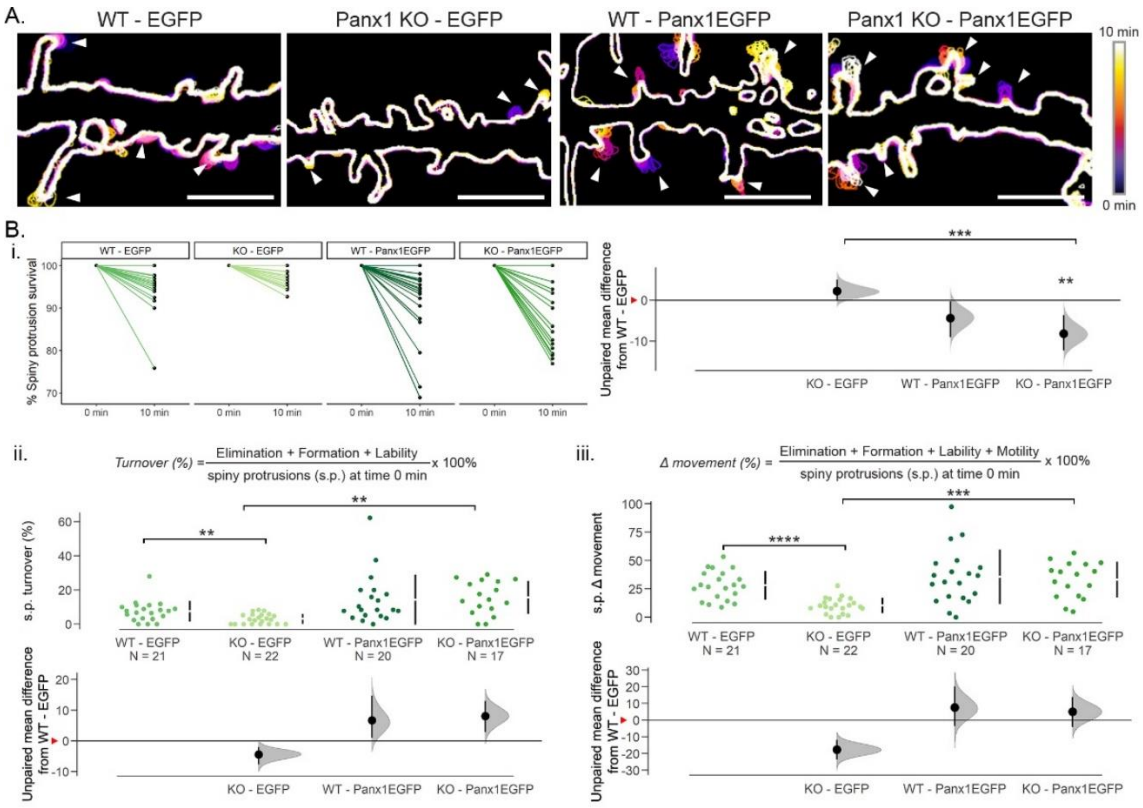

3.6 Discussion

Dendritic spine-based synapses account for the bulk of excitatory neurotransmission in the cerebral cortex and have been implicated in neurodevelopmental and neuropsychiatric disorders (Forrest et al., 2018; Kwon et al., 2019; Lima-Caldeira et al., 2019; Nishiyama, 2019). Although the mechanisms underlying plasticity of existing dendritic spines have

been well characterized (Araya et al., 2014; Holtmaat et al., 2005; Sala & Segal, 2014; Schätzle et al., 2018), the processes involved in their formation are less well understood (Sando et al., 2017; Sigler et al., 2017; reviewed in Südhof, 2018). Here we identified a novel role for Panx1 in regulating the dynamics of developing dendritic spines, building on previous work showing that *Panx1* KO cortical neurons exhibit higher dendritic spine density and more complex networks. Our investigation revealed a reciprocal relationship between Panx1 expression levels and spiny protrusion density and stability. Additionally, in order to make these discoveries, we optimized methods for the visualization and analysis of spiny protrusion dynamics, thereby providing a novel approach for similar types of studies. While the current study was focused on a single timepoint (DIV10), our intriguing results suggest that longitudinal analyses are now warranted. Although *in vitro* spine plasticity characteristics correlate highly with those observed in more complex experimental models (e.g. slice), it will be important to confirm our findings from primary cultures within more comprehensive model systems.

Moreover, even though our global *Panx1* KO mice have been backcrossed for over 10 generations onto a C57BL/6J background (Sanchez-Arias et al., 2019), we cannot at this time rule out putative indirect contributions of potential passenger genetic variants to outcomes observed with *Panx1* KO (Vanden Berghe et al., 2015). The original strain, on a 129X1/SvJ background, in which *Panx1*$^{f/f}$ was generated to create the global *Panx1* KO via a cross with a *CMV-Cre* line (Dvoriantchikova et al., 2012), contains a loss of function mutation in *Casp4* (*Casp11*) and is predicted to have additional possible variants in *Mmp1a*, *Olfr832*, *Fbxl12*, *ENSMUSG00000095186*, and *ENSMUSG00000095891* (Vanden Berghe et al., 2015). In support of our interpretation that loss of *Panx1* (rather

than a passenger variant) increases dendritic spine density in our global *Panx1* KO cortical neurons, we previously replicated our observations from the global *Panx1* KO in conditional *Panx1 KO* (*Panx1*$^{f/f}$*;Emx1*$^{IRES\text{-}Cre}$) strain compared with *Panx1*$^{f/f}$ littermates (i.e. same genetic background in conditional KO and control littermate mice). Further supporting a role for Panx1 in regulating dendritic spine density, transient expression of Panx1EGFP both in WT and *Panx1* KO neurons rescued decreased spiny protrusion density when compared to control EGFP-expressing neurons (control). Taken together these data support the interpretation that Panx1 expression correlates negatively with spiny protrusion density.

The relatively muted impact of Panx1EGFP over-expression in WT neurons, implies there could be a ceiling effect for Panx1 regulation of spiny protrusion dynamics. Saturation of the effect of Panx1 could result from limited availability of machinery for properly trafficking the added and could be a consequence of self-regulation via ATP-dependent internalization (Boyce et al., 2015; Boyce and Swayne, 2017). Alternatively, the effects of supplementary Panx1 could be constrained by limited amounts of endogenous interacting partners, such as Crmp2, Arp3c, and actin or saturation of downstream autocrine or paracrine purinergic signalling pathways related to its ATP release function (e.g. ATP stimulating glia; Abbracchio et al., 2009; Bhalla-Gehi et al., 2010; Wicki-Stordeur and Swayne, 2013; Dahl, 2015; Yang et al., 2015; Xu et al., 2018). In contrast to WT neurons, transient expression of Panx1EGFP exhibited significant effects on spiny protrusion dynamics in *Panx1* KO cultures. Somewhat consistent with previous results, in EGFP-control-expressing cultures, loss of Panx1 precociously stabilized spiny protrusions, pointing to a fundamentally different underlying molecular organization.

Consistent with this idea, recent work has identified brain enriched and autism associated single nucleotide polymorphisms (SNPs) resulting in changes in Panx1 expression levels; although the direction of this change (i.e. decrease or increase Panx1 expression) was not identified (Davis et al., 2012). Further supporting a role for Panx1 in neuronal development, intellectual disability was observed in an individual with a germline single nucleotide polymorphism in *PANX1* (Shao et al., 2016).

In addition to playing a direct role in neurodevelopment, Panx1 is also indirectly involved through its interaction with Crmp2 and purinergic receptor signalling (Boyce et al., 2015; Boyce & Swayne, 2017; reviewed in Swayne & Boyce, 2017). Crmp2 auto-antibodies have been implicated in ASD (Braunschweig et al., 2013), while suramin treatment corrected synaptic and behavioural phenotypes in the Fragile X mouse model (J. C. Naviaux et al., 2015; R. K. Naviaux et al., 2013, 2017).

In summary, this work significantly advances our understanding of the role on Panx1 in dendritic spine development and underscores the importance of additional molecular mechanistic studies investigating intrinsic (e.g. Crmp2) and extrinsic (e.g. glia) pathways.

4 Chapter 4: General discussion

The studies conducted in this dissertation investigated the role of the channel-forming protein Panx1 in the development of dendritic spines and neuronal networks. In this chapter I will integrate how these findings contribute and expand our understanding of Panx1 and its role in neuronal development.

4.1 Elucidating a developmental role for Panx1 in the cerebral cortex

Early studies suggested *Panx1* transcript expression level changes coincided with the critical period for synaptogenesis and dendritic spine formation (Ray et al., 2005; Vogt et al., 2005). Additionally, pioneering work by Zoidl (2007) localized Panx1 to postsynaptic sites in cultured hippocampal neurons co-transfected with Panx1 and PSD-95. Moreover, *in vitro* and *in vivo* work from our group in Neuro2a cells and NPCs, implicated Panx1 in NPC maintenance, migration, and neurite formation and revealed interactions with important cytoskeletal regulators of neuronal morphology. Consistent with a role for Panx1 in regulating synaptic biology, a series of studies using adult hippocampal slices implicated Panx1 in hippocampal excitatory synaptic plasticity (Prochnow et al., 2012; Ardiles et al., 2014; Gajardo et al., 2018). Genetic or pharmacological disruption of Panx1 induced enhanced excitability and longer and more persistent LTP Despite these initial important advances in the characterization of neuronal Panx1, application of these findings to further our *in vivo* understanding of the role of Panx1 in neuronal morphology, specifically neurite formation, under healthy conditions remained a significant knowledge gap in the field.

Importantly, my work has revealed that Panx1 regulation of dendritic spine development and dynamics correlates with neuronal network formation. This places Panx1 as a central player in realizing Hebb's Postulate (Hebb, 1949):

> "*When an axon of cell A is near enough to excite cell B and repeatedly or persistently takes part in firing it, some growth process or metabolic change takes place in one or both cells such that A's efficiency, as one of the cells firing, is increased.*"
>
> (on "cell ensembles") "*a diffuse structure comprising cells in the cortex and diencephalon, capable of acting briefly as a closed system, delivering facilitation to other such systems. Depending on functional requirements, individual cells could participate in different cell assemblies and be involved in multiple computations.*"

Hebb's words would antecedent the discovery of LTP in rabbits in 1966 and the visualization synapses by electron-microscopy (Calverley and Jones, 1990; Bliss et al., 2003); however, the accuracy of his statement is undeniable accurate and almost puzzling. Much like he proposed, neuronal activity can induce rapid dendritic spine morphogenesis, making dendritic spines, or in Hebb's words "*some growth process"*, the substrate for synaptic plasticity (reviewed in Calverley and Jones, 1990; Harris, 1999; Maletic-Savatic et al., 1999; Sala and Segal, 2014). Moreover, Hebb's description on cell ensembles still holds true today, as evidenced by longitudinal imaging of neuronal networks *in vitro* and *in vivo* in which spontaneous and task-specific (in the case of living animals) groups of significant co-activated neurons can clearly be identified (Tibau et al., 2013; Miller et al.,

2014; Carrillo-Reid et al., 2015, 2016). My novel findings presented in this dissertation placePanx1 as a significant player in this process.

As mentioned above, the development of cerebral cortex and its circuitry is characterized by *critical periods* (Hensch, 2004, 2005). Critical periods are strict time windows in which experience fine-tunes and reshapes cortical circuits with life-long consequences (Berardi et al., 2000; Hensch, 2005). As alluded to earlier in this dissertation, most developmental synaptogenesis occurs during critical period in the first and second postnatal weeks in rodents (Schlaggar et al., 1993; O'Leary et al., 1994; Micheva and Beaulieu, 1996), coinciding with the developmental downregulation of Panx1. My work has confirmed synaptic enrichment of Panx1 as well as developmental downregulation of synaptic Panx1 protein in the cerebral cortex(**Figure 2.1)**. Importantly, cortical synaptosome preparations from *Panx1* KO mice exhibited increased PSD-95 and postsynaptic glutamate receptor content in early (P14) and late (P29) postnatal development (**Figure 2.2**).

Complementing these biochemical findings approach, live cell Ca^{2+} imaging coupled to in silico network analysis revealed that cortical cultures derived from *Panx1* KO mice exhibited more and larger neuronal networks(**Figure 2.1**). These observations were paralleled by increased dendritic spine density and dendritic spine positive for PSD-95 in *Panx1* KO fixed cultured cortical neurons and increased spine density in layer 5 pyramidal neurons in both global and cell-type specific *Panx1* KO fixed brain slices (**Figure 2.4**).

While the exact mechanisms underlying dendritic spine genesis remain to be fully resolved, highly dynamic spiny protrusions stabilize and mature into dendritic spines as neurons develop by both synaptic activity-independent and dependent mechanisms *in vitro* and *in vivo* (Ziv and Smith, 1996; Fiala et al., 1998; Maletic-Savatic et al., 1999; Prange

and Murphy, 2001; Trachtenberg et al., 2002; Yuste and Bonhoeffer, 2004). The findings from my investigation on spiny protrusions in live WT and *Panx1* KO neurons transiently expressing EGFP or Panx1EGFP revealed Panx1 expression-associated increased motility and lability and *Panx1* KO increased stabilization suggest that Panx1 regulation of dendritic spines is associated with Panx1 regulation of spiny protrusion dynamics. The stabilization of spiny protrusions is mainly driven by neuronal maturation (spiny protrusions become less dynamic with days in culture and age), components of the extracellular matrix, development of an active zone in a presynaptic partner, and PSD-95 translocation into spiny protrusions (Ziv and Smith, 1996; Fiala et al., 1998; Dunaevsky et al., 1999; Friedman et al., 2000; Jontes and Smith, 2000; Korkotian and Segal, 2001; Prange and Murphy, 2001; Zuo et al., 2005a; Cane et al., 2014; Levy et al., 2014). Notably, PSD-95 delivery to spiny protrusions and dendritic spines requires complex cross-talk between actin and tubulin (Gu et al., 2008; Hu et al., 2011; Schätzle et al., 2018). It is reasonable to suggest that spiny protrusion stabilization and increased spine density found in *Panx1* KO neurons could be partly secondary to increased delivery of PSD-95 to dendritic spines by mechanisms involving interactions with cytoskeletal elements regulating actin and tubulin (Frederiksen et al., 2019).

What other signalling pathways might be involved in Panx1 regulation of dendritic spines? Given its role as an ATP channel, Panx1 likely has an impact on purinergic control of dendritic spine and neuronal network development. For example, anoxia-induced glutamatergic NMDA neurotransmission in hippocampal slices can activate Panx1 channels (Weilinger et al., 2012, 2016). While this NMDA-Panx1 signalling remains to be tested in healthy conditions, NMDA-mediated activation of Panx1 would result in ATP

release, activating ionotropic and metabotropic purinergic receptors and recruiting microglia processes to synapses (Paolicelli et al., 2011; Weinhard et al., 2018; Cserép et al., 2019). For example, genetic disruption of P2X7R purinergic signalling in a model of Rett syndrome (characterized by decreased spine density) led to decreased spine elimination and consequently increased spine density in cortical neurons (Garré et al., 2020). Interestingly, pharmacological disruption of P2X7R signalling with suramin in animal models of Fragile X (*Fmr1* KO) normalizes PSD size in spines, which is characteristically large in *Fmr1* KO mice (Naviaux et al., 2013, 2015, 2017). These contrasting results could partly be explained by differential timing of these interventions, highlighting the importance of critical periods of brain plasticity (Hensch, 2005).

In addition to regulating dendritic spines, purinergic signalling also shapes NPC development. Moreover, aberrant purinergic signalling is associated with developmental disorders. Furthermore, along these lines several risk genes associated with neurodevelopmental disorders have both NPC developmental as well as dendritic spine roles (Heavner and Smith, 2020). Consistent with its multiple roles in regulating neuronal development (both NPCs and dendritic spines), variants of *Panx1* have been recently implicated in neurodevelopmental disorders NDDs). Several *Panx1* SNPs were identified in an ASD GWAS-eQTL analysis by Davis et al (2012). This means the ASD-associated SNPs identified in this study cause changes in *Panx1* expression levels (albeit, the direction of expression change was not revealed). Another study described the discovery of a *PANX1* variant associated multi-system disorder including intellectual disability (Shao et al., 2016). The neurological phenotype of *Panx1* disruption is reminiscent of that of *Syngap1* disruption (Gamache et al., 2020). Deletion of *Syngap1,* a Ras-GAP-activating

protein enriched in dendritic spines, results in increase dendritic spine density, increased levels of PSD-95, increased postsynaptic glutamate receptors, and altered neuronal networks (Clement et al., 2012; Aceti et al., 2015; Araki et al., 2015). Disruption of several of other ASD associated genes produce similar phenotypes (Forrest et al, 2018). Without discounting the convergence of similar dendritic spine phenotypes produced by disruption of these ASD-associated genes supports a model in which synaptic dysfunction plays a key pathogenic role.

Overall, the findings presented in this thesis furthers our understanding on the complexity of the regulation of dendritic spine development and underscore the importance of *Panx1* and similar dendritic spine-regulating genes in healthy brain development. Given the availability of pharmacological tools to modulate Panx1 function, and relatedly purinergic receptor signalling, these findings present potentials new avenues of therapeutic interventions for neurodevelopmental disorders.

Figure 4.1. Putative mechanisms for Panx1 regulation of dendritic spines. In *Panx1*$^{+/+}$ (WT) neurons, postnatal developmental regulation of Panx1 expression levels could contribute to proper development of neuronal circuits via its role in purinergic signaling (activation of ionotropic P2X and metabotropic P2Y purinergic receptors, recruitment of microglia, and Panx1 ATP-internalization) and/or direct protein interactions with regulatory elements of the neuronal cytoskeleton that control dendritic spine maturation. Therefore, loss of Panx1 (*Panx1*$^{-/-}$, *Panx1* KO) could lead to impaired circuitry refinement during critical periods, resulting in increased stability and density of spiny protrusions and altered neuronal network connectivity as observed with *Panx1* KO and risk genes for neurodevelopmental disorders. These putative mechanisms will require further validation in various experimental models. Glut, Glutamate; P2XR, ionotropic purinergic receptor; P2YR, metabotropic purinergic receptor; NMDAR, NMDA receptor; MTs, microtubules.

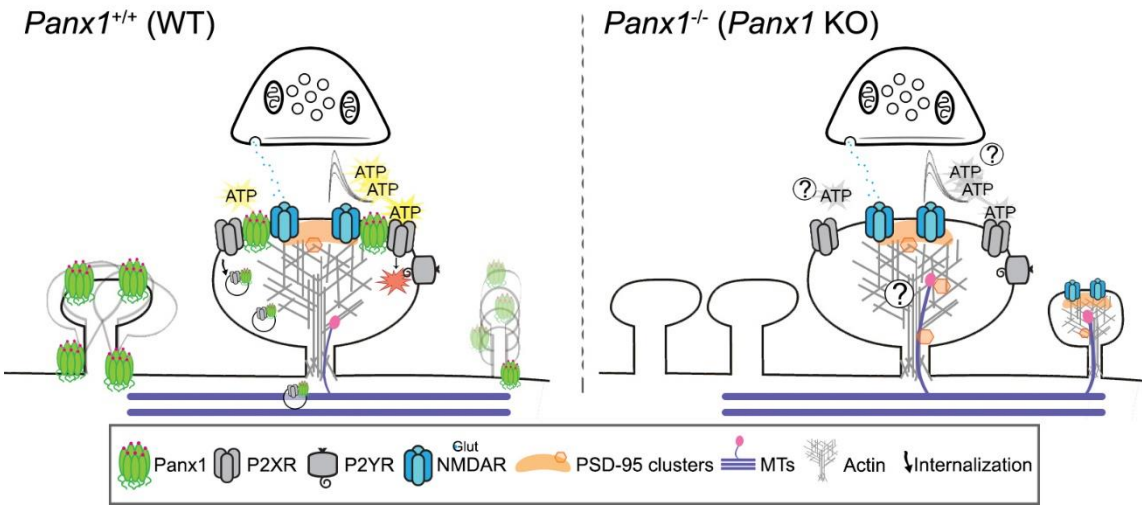
Panx1+/+ (WT)
Panx1-/- (Panx1 KO)
ATP
ATP
ATP
ATP
ATP
ATP
?
?
?
Panx1
P2XR
P2YR
Glut
NMDAR
PSD-95 clusters
MTs
Actin
Internalization

Bibliography

Abbracchio MP, Burnstock G, Verkhratsky A, Zimmermann H (2009) Purinergic signalling in the nervous system: an overview. Trends Neurosci 32:19–29.

Aceti M, Creson TK, Vaissiere T, Rojas C, Huang W-C, Wang Y-X, Petralia RS, Page DT, Miller CA, Rumbaugh G (2015) Syngap1 Haploinsufficiency Damages a Postnatal Critical Period of Pyramidal Cell Structural Maturation Linked to Cortical Circuit Assembly. Biol Psychiatry 77:805–815.

Adelsberger H, Garaschuk O, Konnerth A (2005) Cortical calcium waves in resting newborn mice. Nat Neurosci 8:988–990.

Ambrosi C, Gassmann O, Pranskevich JN, Boassa D, Smock A, Wang J, Dahl G, Steinem C, Sosinsky GE (2010) Pannexin1 and Pannexin2 Channels Show Quaternary Similarities to Connexons and Different Oligomerization Numbers from Each Other. J Biol Chem 285:24420–24431.

Araki Y, Zeng M, Zhang M, Huganir RL (2015) Rapid Dispersion of SynGAP from Synaptic Spines Triggers AMPA Receptor Insertion and Spine Enlargement during LTP. Neuron 85:173–189.

Araya R, Vogels TP, Yuste R (2014) Activity-dependent dendritic spine neck changes are correlated with synaptic strength. Proc Natl Acad Sci 111:E2895–E2904.

Arce-McShane FI, Ross CF, Takahashi K, Sessle BJ, Hatsopoulos NG (2016) Primary motor and sensory cortical areas communicate via spatiotemporally coordinated networks at multiple frequencies. Proc Natl Acad Sci 113:5083–5088.

Ardiles AO, Flores-Muñoz C, Toro-Ayala G, Cárdenas AM, Palacios AG, Muñoz P, Fuenzalida M, Sáez JC, Martínez AD (2014) Pannexin 1 regulates bidirectional hippocampal synaptic plasticity in adult mice. Front Cell Neurosci 8 Available at: https://www.frontiersin.org/articles/10.3389/fncel.2014.00326/full.

Awad PN, Amegandjin CA, Szczurkowska J, Carriço JN, Fernandes do Nascimento AS, Baho E, Chattopadhyaya B, Cancedda L, Carmant L, Di Cristo G (2018) KCC2 regulates dendritic spine formation in a brain-region specific and BDNF dependent manner. Cereb Cortex 28:4049–4062.

Banker G (2018) The Development of Neuronal Polarity: A Retrospective View. J Neurosci 38:1867–1873.

Baranova A, Ivanov D, Petrash N, Pestova A, Skoblov M, Kelmanson I, Shagin D, Nazarenko S, Geraymovych E, Litvin O, Tiunova A, Born TL, Usman N, Staroverov D, Lukyanov S, Panchin Y (2004) The mammalian pannexin family is

homologous to the invertebrate innexin gap junction proteins. Genomics 83:706–716.

Bardy C, Hurk M van den, Eames T, Marchand C, Hernandez RV, Kellogg M, Gorris M, Galet B, Palomares V, Brown J, Bang AG, Mertens J, Böhnke L, Boyer L, Simon S, Gage FH (2015) Neuronal medium that supports basic synaptic functions and activity of human neurons in vitro. Proc Natl Acad Sci 112:E2725–E2734.

Begandt D, Good ME, Keller AS, DeLalio LJ, Rowley C, Isakson BE, Figueroa XF (2017) Pannexin channel and connexin hemichannel expression in vascular function and inflammation. BMC Cell Biol 18:2.

Benson D, Watkins F, Steward O, Banker G (1994) Characterization of GABAergic neurons in hippocampal cell cultures. J Neurocytol 23:279–295.

Berardi N, Pizzorusso T, Maffei L (2000) Critical periods during sensory development. Curr Opin Neurobiol 10:138–145.

Bernard C (2019) Changing the Way We Report, Interpret, and Discuss Our Results to Rebuild Trust in Our Research. eNeuro 6.

Bhalla-Gehi R, Penuela S, Churko JM, Shao Q, Laird DW (2010) Pannexin1 and Pannexin3 Delivery, Cell Surface Dynamics, and Cytoskeletal Interactions. J Biol Chem 285:9147–9160.

Bialecki J, Werner A, Weilinger NL, Tucker CM, Vecchiarelli HA, Egaña J, Mendizabal-Zubiaga J, Grandes P, Hill MN, Thompson RJ (2020) Suppression of Presynaptic Glutamate Release by Postsynaptic Metabotropic NMDA Receptor Signalling to Pannexin-1. J Neurosci 40:729–742.

Billaud M, Chiu Y-H, Lohman AW, Parpaite T, Butcher JT, Mutchler SM, DeLalio LJ, Artamonov MV, Sandilos JK, Best AK, Somlyo AV, Thompson RJ, Le TH, Ravichandran KS, Bayliss DA, Isakson BE (2015) A molecular signature in the pannexin1 intracellular loop confers channel activation by the α1 adrenoreceptor in smooth muscle cells. Sci Signal 8:ra17–ra17.

Bliss TVP, Collingridge GL, Morris RGM, Lømo T (2003) The discovery of long-term potentiation. Philos Trans R Soc Lond B Biol Sci 358:617–620.

Boassa D, Ambrosi C, Qiu F, Dahl G, Gaietta G, Sosinsky G (2007) Pannexin1 Channels Contain a Glycosylation Site That Targets the Hexamer to the Plasma Membrane. J Biol Chem 282:31733–31743.

Boyce AKJ, Epp AL, Nagarajan A, Swayne LA (2018) Transcriptional and post-translational regulation of pannexins. Biochim Biophys Acta BBA - Biomembr 1860:72–82.

Boyce AKJ, Kim MS, Wicki-Stordeur LE, Swayne LA (2015) ATP stimulates pannexin 1 internalization to endosomal compartments. Biochem J 470:319–330.

Boyce AKJ, Swayne LA (2017) P2X7 receptor cross-talk regulates ATP-induced pannexin 1 internalization. Biochem J 474:2133–2144.

Braunschweig D, Krakowiak P, Duncanson P, Boyce R, Hansen RL, Ashwood P, Hertz-Picciotto I, Pessah IN, Van de Water J (2013) Autism-specific maternal autoantibodies recognize critical proteins in developing brain. Transl Psychiatry 3:e277–e277.

Brusco J, Dall'Oglio A, Rocha LB, Rossi MA, Moreira JE, Rasia-Filho AA (2010) Descriptive findings on the morphology of dendritic spines in the rat medial amygdala. Neurosci Lett 483:152–156.

Burma NE, Bonin RP, Leduc-Pessah H, Baimel C, Cairncross ZF, Mousseau M, Shankara JV, Stemkowski PL, Baimoukhametova D, Bains JS, Antle MC, Zamponi GW, Cahill CM, Borgland SL, De Koninck Y, Trang T (2017) Blocking microglial pannexin-1 channels alleviates morphine withdrawal in rodents. Nat Med 23:355–360.

Buzsáki G (2010) Neural syntax: cell assemblies, synapsembles, and readers. Neuron 68:362–385.

Bystron I, Blakemore C, Rakic P (2008) Development of the human cerebral cortex: Boulder Committee revisited. Nat Rev Neurosci 9:110–122.

Cajal SR (1995) Histology of the nervous system of man and vertebrates. Hist Neurosci Oxf Univ Press N Y.

Cajal S y (1894) Estructura intima de los centros nerviosos. Rev Cienc Med 20:145–160.

Calin-Jageman RJ, Cumming G (2019) Estimation for Better Inference in Neuroscience. eNeuro 6 Available at: https://www.eneuro.org/content/6/4/ENEURO.0205-19.2019.

Calverley RKS, Jones DG (1990) Contributions of dendritic spines and perforated synapses to synaptic plasticity. Brain Res Rev 15:215–249.

Cane M, Maco B, Knott G, Holtmaat A (2014) The Relationship between PSD-95 Clustering and Spine Stability In Vivo. J Neurosci 34:2075–2086.

Carrillo-Reid L, Miller JK, Hamm JP, Jackson J, Yuste R (2015) Endogenous sequential cortical activity evoked by visual stimuli. J Neurosci 35:8813–8828.

Carrillo-Reid L, Yang W, Bando Y, Peterka DS, Yuste R (2016) Imprinting and recalling cortical ensembles. Science 353:691–694.

Chekeni FB, Elliott MR, Sandilos JK, Walk SF, Kinchen JM, Lazarowski ER, Armstrong AJ, Penuela S, Laird DW, Salvesen GS, Isakson BE, Bayliss DA, Ravichandran KS (2010) Pannexin 1 channels mediate 'find-me' signal release and membrane permeability during apoptosis. Nature 467:863–867.

Chen X, Winters C, Azzam R, Li X, Galbraith JA, Leapman RD, Reese TS (2008) Organization of the core structure of the postsynaptic density. Proc Natl Acad Sci 105:4453–4458.

Chiu Y-H, Jin X, Medina CB, Leonhardt SA, Kiessling V, Bennett BC, Shu S, Tamm LK, Yeager M, Ravichandran KS, Bayliss DA (2017) A quantized mechanism for activation of pannexin channels. Nat Commun 8:1–15.

Chiu Y-H, Schappe MS, Desai BN, Bayliss DA (2018) Revisiting multimodal activation and channel properties of Pannexin 1. J Gen Physiol 150:19–39.

Clement JP, Aceti M, Creson TK, Ozkan ED, Shi Y, Reish NJ, Almonte AG, Miller BH, Wiltgen BJ, Miller CA, Xu X, Rumbaugh G (2012) Pathogenic SYNGAP1 Mutations Impair Cognitive Development by Disrupting Maturation of Dendritic Spine Synapses. Cell 151:709–723.

Cone AC, Ambrosi C, Scemes E, Martone ME, Sosinsky GE (2013) A comparative antibody analysis of pannexin1 expression in four rat brain regions reveals varying subcellular localizations. Front Pharmacol 4:6.

Cserép C et al. (2019) Microglia monitor and protect neuronal function via specialized somatic purinergic junctions. Available at: http://biorxiv.org/lookup/doi/10.1101/606079.

Dahl G (2015) ATP release through pannexon channels. Philos Trans R Soc B Biol Sci 370:20140191.

Davis LK, Gamazon ER, Kistner-Griffin E, Badner JA, Liu C, Cook EH, Sutcliffe JS, Cox NJ (2012) Loci nominally associated with autism from genome-wide analysis show enrichment of brain expression quantitative trait loci but not lymphoblastoid cell line expression quantitative trait loci. Mol Autism 3:3.

DeFelipe J, Fariñas I (1992) The pyramidal neuron of the cerebral cortex: Morphological and chemical characteristics of the synaptic inputs. Prog Neurobiol 39:563–607.

Deng Z, He Z, Maksaev G, Bitter RM, Rau M, Fitzpatrick JAJ, Yuan P (2020a) Cryo-EM structures of the ATP release channel pannexin 1. bioRxiv:2020.01.05.895235.

Deng Z, He Z, Maksaev G, Bitter RM, Rau M, Fitzpatrick JAJ, Yuan P (2020b) Cryo-EM structures of the ATP release channel pannexin 1. Nat Struct Mol Biol 27:373–381.

Dent EW (2017) Of microtubules and memory: implications for microtubule dynamics in dendrites and spines. Mol Biol Cell 28:1–8.

Dent EW, Merriam EB, Hu X (2011) The dynamic cytoskeleton: backbone of dendritic spine plasticity. Curr Opin Neurobiol 21:175–181.

Dong X, Shen K, Bülow HE (2015) Intrinsic and Extrinsic Mechanisms of Dendritic Morphogenesis. Annu Rev Physiol 77:271–300.

Dossi E, Blauwblomme T, Moulard J, Chever O, Vasile F, Guinard E, Le Bert M, Couillin I, Pallud J, Capelle L (2018) Pannexin-1 channels contribute to seizure generation in human epileptic brain tissue and in a mouse model of epilepsy. Sci Transl Med 10:eaar3796.

Dotti C, Sullivan C, Banker G (1988) The establishment of polarity by hippocampal neurons in culture. J Neurosci 8:1454–1468.

Dunaevsky A, Tashiro A, Majewska A, Mason C, Yuste R (1999) Developmental regulation of spine motility in the mammalian central nervous system. Proc Natl Acad Sci 96:13438–13443.

Dvoriantchikova G, Ivanov D, Barakat D, Grinberg A, Wen R, Slepak VZ, Shestopalov VI (2012) Genetic Ablation of Pannexin1 Protects Retinal Neurons from Ischemic Injury. PLOS ONE 7:e31991.

Ehrlich I, Klein M, Rumpel S, Malinow R (2007) PSD-95 is required for activity-driven synapse stabilization. Proc Natl Acad Sci 104:4176–4181.

El-Husseini AE-D, Schnell E, Chetkovich DM, Nicoll RA, Bredt DS (2000) PSD-95 involvement in maturation of excitatory synapses. Science 290:1364–1368.

Fiala JC, Feinberg M, Popov V, Harris KM (1998) Synaptogenesis Via Dendritic Filopodia in Developing Hippocampal Area CA1. J Neurosci 18:8900–8911.

Forrest MP, Parnell E, Penzes P (2018) Dendritic structural plasticity and neuropsychiatric disease. Nat Rev Neurosci 19:215–234.

Frank AC, Huang S, Zhou M, Gdalyahu A, Kastellakis G, Silva TK, Lu E, Wen X, Poirazi P, Trachtenberg JT, Silva AJ (2018) Hotspots of dendritic spine turnover facilitate clustered spine addition and learning and memory. Nat Commun 9:1–11.

Frederiksen SD, Wicki-Stordeur LE, Sanchez-Arias JC, Swayne LA (2019) Exploring the Pannexin 1 interactome: In silico cross-analyses with postsynaptic proteins and neuropsychiatric disorder susceptibility genes. bioRxiv:801563.

Friedman HV, Bresler T, Garner CC, Ziv NE (2000) Assembly of New Individual Excitatory Synapses: Time Course and Temporal Order of Synaptic Molecule Recruitment. Neuron 27:57–69.

Funahashi Y, Namba T, Nakamuta S, Kaibuchi K (2014) Neuronal polarization in vivo: Growing in a complex environment. Curr Opin Neurobiol 27:215–223.

Gajardo I, Salazar CS, Lopez-Espíndola D, Estay C, Flores-Muñoz C, Elgueta C, Gonzalez-Jamett AM, Martínez AD, Muñoz P, Ardiles ÁO (2018) Lack of Pannexin 1 Alters Synaptic GluN2 Subunit Composition and Spatial Reversal Learning in Mice. Front Mol Neurosci 11 Available at: https://www.frontiersin.org/articles/10.3389/fnmol.2018.00114/full.

Gamache TR, Araki Y, Huganir RL (2020) Twenty Years of SynGAP Research: From Synapses to Cognition. J Neurosci 40:1596–1605.

Garré JM, Silva HM, Lafaille JJ, Yang G (2020) P2X7 receptor inhibition ameliorates dendritic spine pathology and social behavioral deficits in Rett syndrome mice. Nat Commun 11:1–13.

Gray EG (1959) Electron microscopy of synaptic contacts on dendrite spines of the cerebral cortex. Nature 183:1592–1593.

Gu J, Firestein BL, Zheng JQ (2008) Microtubules in Dendritic Spine Development. J Neurosci 28:12120–12124.

Gulley RL, Reese TS (1981) Cytoskeletal organization at the postsynaptic complex. J Cell Biol 91:298–302.

Hallman LE, Schofield BR, Lin C-S (1988) Dendritic morphology and axon collaterals of corticotectal, corticopontine, and callosal neurons in layer V of primary visual cortex of the hooded rat. J Comp Neurol 272:149–160.

Harms KJ, Craig AM (2005) Synapse composition and organization following chronic activity blockade in cultured hippocampal neurons. J Comp Neurol 490:72–84.

Harris KD, Csicsvari J, Hirase H, Dragoi G, Buzsaki G (2003) Organization of cell assemblies in the hippocampus. Nature 424:552–556.

Harris KM (1999) Structure, development, and plasticity of dendritic spines. Curr Opin Neurobiol 9:343–348.

Harris KM, Weinberg RJ (2012) Ultrastructure of Synapses in the Mammalian Brain. Cold Spring Harb Perspect Biol 4:a005587.

Heavner WE, Smith SEP (2020) Resolving the Synaptic versus Developmental Dichotomy of Autism Risk Genes. Trends Neurosci 43:227–241.

Hebb DO (1949) The Organization of Behavior: A Neuropsychological Theory. Psychology Press.

Hensch TK (2004) Critical period regulation. Annu Rev Neurosci 27:549–579.

Hensch TK (2005) Critical period plasticity in local cortical circuits. Nat Rev Neurosci 6:877–888.

Higley MJ, Sabatini BL (2012) Calcium Signaling in Dendritic Spines. Cold Spring Harb Perspect Biol 4:a005686.

Ho J, Tumkaya T, Aryal S, Choi H, Claridge-Chang A (2019) Moving beyond P values: data analysis with estimation graphics. Nat Methods 16:565–566.

Holtmaat AJGD, Trachtenberg JT, Wilbrecht L, Shepherd GM, Zhang X, Knott GW, Svoboda K (2005) Transient and Persistent Dendritic Spines in the Neocortex In Vivo. Neuron 45:279–291.

Hoshiba Y, Wada T, Hayashi-Takagi A (2017) Synaptic Ensemble Underlying the Selection and Consolidation of Neuronal Circuits during Learning. Front Neural Circuits 11 Available at: https://www.frontiersin.org/articles/10.3389/fncir.2017.00012/full.

Hotulainen P, Hoogenraad CC (2010) Actin in dendritic spines: connecting dynamics to function. J Cell Biol 189:619–629.

Hu X, Ballo L, Pietila L, Viesselmann C, Ballweg J, Lumbard D, Stevenson M, Merriam E, Dent EW (2011) BDNF-induced increase of PSD-95 in dendritic spines requires dynamic microtubule invasions. J Neurosci 31:15597–15603.

Hu X, Viesselmann C, Nam S, Merriam E, Dent EW (2008) Activity-dependent dynamic microtubule invasion of dendritic spines. J Neurosci 28:13094–13105.

Jin Q, Zhang B, Zheng X, Li N, Xu L, Xie Y, Song F, Bhat EA, Chen Y, Gao N, Guo J, Zhang X, Ye S (2020) Cryo-EM structures of human pannexin 1 channel. Cell Res:1–3.

Jontes JD, Smith SJ (2000) Filopodia, Spines, and the Generation of Synaptic Diversity. Neuron 27:11–14.

Jung CKE, Herms J (2014) Structural Dynamics of Dendritic Spines are Influenced by an Environmental Enrichment: An In Vivo Imaging Study. Cereb Cortex 24:377–384.

Kim EJ, Juavinett AL, Kyubwa EM, Jacobs MW, Callaway EM (2015) Three Types of Cortical Layer 5 Neurons That Differ in Brain-wide Connectivity and Function. Neuron 88:1253–1267.

Korkotian E, Segal M (2001) Regulation of Dendritic Spine Motility in Cultured Hippocampal Neurons. J Neurosci 21:6115–6124.

Kovalzon VM, Moiseenko LS, Ambaryan AV, Kurtenbach S, Shestopalov VI, Panchin YV (2017) Sleep-wakefulness cycle and behavior in pannexin1 knockout mice. Behav Brain Res 318:24–27.

Kwan KY, Šestan N, Anton ES (2012) Transcriptional co-regulation of neuronal migration and laminar identity in the neocortex. Development 139:1535–1546.

Kwon T, Merchán-Pérez A, Rial Verde EM, Rodríguez J-R, DeFelipe J, Yuste R (2019) Ultrastructural, Molecular and Functional Mapping of GABAergic Synapses on Dendritic Spines and Shafts of Neocortical Pyramidal Neurons. Cereb Cortex 29:2771–2781.

Kwon T, Sakamoto M, Peterka DS, Yuste R (2017) Attenuation of Synaptic Potentials in Dendritic Spines. Cell Rep 20:1100–1110.

Larkman AU (1991) Dendritic morphology of pyramidal neurones of the visual cortex of the rat: I. Branching patterns. J Comp Neurol 306:307–319.

Levy AD, Omar MH, Koleske AJ (2014) Extracellular matrix control of dendritic spine and synapse structure and plasticity in adulthood. Front Neuroanat 8 Available at: https://www.frontiersin.org/articles/10.3389/fnana.2014.00116/full.

Li W, Ma L, Yang G, Gan W-B (2017) REM sleep selectively prunes and maintains new synapses in development and learning. Nat Neurosci 20:427–437.

Lima-Caldeira G, Peça J, Carvalho AL (2019) New insights on synaptic dysfunction in neuropsychiatric disorders. Curr Opin Neurobiol 57:62–70.

Lu W, Bushong EA, Shih TP, Ellisman MH, Nicoll RA (2013) The Cell-Autonomous Role of Excitatory Synaptic Transmission in the Regulation of Neuronal Structure and Function. Neuron 78:433–439.

Maletic-Savatic M, Malinow R, Svoboda K (1999) Rapid Dendritic Morphogenesis in CA1 Hippocampal Dendrites Induced by Synaptic Activity. Science 283:1923–1927.

Mancuso JJ, Chen Y, Li X, Xue Z, Wong STC (2013) Methods of dendritic spine detection: From Golgi to high-resolution optical imaging. Neuroscience 251:129–140.

Matsuzaki M, Honkura N, Ellis-Davies GCR, Kasai H (2004) Structural basis of long-term potentiation in single dendritic spines. Nature 429:761–766.

McDonald J (2014) Handbook of Biological Statistics. [online]. Baltimore: Sparky House.

Medina CB, Mehrotra P, Arandjelovic S, Perry JSA, Guo Y, Morioka S, Barron B, Walk SF, Ghesquière B, Krupnick AS, Lorenz U, Ravichandran KS (2020) Metabolites released from apoptotic cells act as tissue messengers. Nature 580:130–135.

Michalski K, Syrjanen JL, Henze E, Kumpf J, Furukawa H, Kawate T (2019) The Cryo-EM Structure of a Pannexin 1 Channel Reveals an Extracellular Gating Mechanism. bioRxiv:2019.12.30.890780.

Michalski K, Syrjanen JL, Henze E, Kumpf J, Furukawa H, Kawate T (2020) The Cryo-EM structure of pannexin 1 reveals unique motifs for ion selection and inhibition Swartz KJ, Dutzler R, Zhou M, eds. eLife 9:e54670.

Micheva KD, Beaulieu C (1996) Quantitative aspects of synaptogenesis in the rat barrel field cortex with special reference to GABA circuitry. J Comp Neurol 373:340–354.

Miller JK, Ayzenshtat I, Carrillo-Reid L, Yuste R (2014) Visual stimuli recruit intrinsically generated cortical ensembles. Proc Natl Acad Sci 111:E4053–E4061.

Miyata T (2004) Asymmetric production of surface-dividing and non-surface-dividing cortical progenitor cells. Development 131:3133–3145.

Molyneaux BJ, Arlotta P, Menezes JR, Macklis JD (2007) Neuronal subtype specification in the cerebral cortex. Nat Rev Neurosci 8:427–437.

Murphy TH, Blatter LA, Wier WG, Baraban JM (1992) Spontaneous synchronous synaptic calcium transients in cultured cortical neurons. J Neurosci 12:4834–4845.

Nakamuta S, Funahashi Y, Namba T, Arimura N, Picciotto MR, Tokumitsu H, Soderling TR, Sakakibara A, Miyata T, Kamiguchi H, Kaibuchi K (2011) Local Application of Neurotrophins Specifies Axons Through Inositol 1,4,5-Trisphosphate, Calcium, and Ca2+/Calmodulin-Dependent Protein Kinases. Sci Signal 4:ra76–ra76.

Naviaux JC, Wang L, Li K, Bright AT, Alaynick WA, Williams KR, Powell SB, Naviaux RK (2015) Antipurinergic therapy corrects the autism-like features in the Fragile X (Fmr1 knockout) mouse model. Mol Autism 6:1.

Naviaux RK et al. (2017) Low-dose suramin in autism spectrum disorder: a small, phase I/II, randomized clinical trial. Ann Clin Transl Neurol 4:491–505.

Naviaux RK, Zolkipli Z, Wang L, Nakayama T, Naviaux JC, Le TP, Schuchbauer MA, Rogac M, Tang Q, Dugan LL, Powell SB (2013) Antipurinergic Therapy Corrects the Autism-Like Features in the Poly(IC) Mouse Model. PLOS ONE 8:e57380.

Nishiyama J (2019) Plasticity of dendritic spines: Molecular function and dysfunction in neurodevelopmental disorders. Psychiatry Clin Neurosci 73:541–550.

Noctor SC, Martínez-Cerdeño V, Ivic L, Kriegstein AR (2004) Cortical neurons arise in symmetric and asymmetric division zones and migrate through specific phases. Nat Neurosci 7:136–144.

Oh WC, Hill TC, Zito K (2013) Synapse-specific and size-dependent mechanisms of spine structural plasticity accompanying synaptic weakening. Proc Natl Acad Sci 110:E305–E312.

Okamoto K-I, Nagai T, Miyawaki A, Hayashi Y (2004) Rapid and persistent modulation of actin dynamics regulates postsynaptic reorganization underlying bidirectional plasticity. Nat Neurosci 7:1104–1112.

O'Leary DDM, Ruff NL, Dyck RH (1994) Development, critical period plasticity, and adult reorganizations of mammalian somatosensory systems. Curr Opin Neurobiol 4:535–544.

Panchin Y, Kelmanson I, Matz M, Lukyanov K, Usman N, Lukyanov S (2000) A ubiquitous family of putative gap junction molecules. Curr Biol 10:R473-4.

Paolicelli RC, Bolasco G, Pagani F, Maggi L, Scianni M, Panzanelli P, Giustetto M, Ferreira TA, Guiducci E, Dumas L, Ragozzino D, Gross CT (2011) Synaptic Pruning by Microglia Is Necessary for Normal Brain Development. Science 333:1456–1458.

Penuela S, Bhalla R, Gong X-Q, Cowan KN, Celetti SJ, Cowan BJ, Bai D, Shao Q, Laird DW (2007) Pannexin 1 and pannexin 3 are glycoproteins that exhibit many distinct characteristics from the connexin family of gap junction proteins. J Cell Sci 120:3772–3783.

Penuela S, Bhalla R, Nag K, Laird DW (2009) Glycosylation Regulates Pannexin Intermixing and Cellular Localization. Mol Biol Cell 20:4313–4323.

Penuela S, Gehi R, Laird DW (2013) The biochemistry and function of pannexin channels. Biochim Biophys Acta BBA - Biomembr 1828:15–22.

Peters A, Jones EG (1984) Cellular components of the cerebral cortex. Plenum Press. Available at: https://books.google.ca/books?id=EqrwAAAAMAAJ.

Petit TL, Leboutillier JC, Gregorio A, Libstug H (1988) The pattern of dendritic development in the cerebral cortex of the rat. Dev Brain Res 41:209–219.

Phillips M, Pozzo-Miller L (2015) Dendritic spine dysgenesis in autism related disorders. Neurosci Lett 601:30–40.

Prange O, Murphy TH (2001) Modular Transport of Postsynaptic Density-95 Clusters and Association with Stable Spine Precursors during Early Development of Cortical Neurons. J Neurosci 21:9325–9333.

Prochnow N, Abdulazim A, Kurtenbach S, Wildförster V, Dvoriantchikova G, Hanske J, Petrasch-Parwez E, Shestopalov VI, Dermietzel R, Manahan-Vaughan D, Zoidl G (2012) Pannexin1 Stabilizes Synaptic Plasticity and Is Needed for Learning. PLOS ONE 7:e51767.

Qu R, Dong L, Zhang J, Yu X, Wang L, Zhu S (2020) Cryo-EM structure of human heptameric Pannexin 1 channel. Cell Res Available at: http://www.nature.com/articles/s41422-020-0298-5.

Ray A, Zoidl G, Weickert S, Wahle P, Dermietzel R (2005) Site-specific and developmental expression of pannexin1 in the mouse nervous system. Eur J Neurosci 21:3277–3290.

Romand S, Wang Y, Toledo-Rodriguez M, Markram H (2011) Morphological Development of Thick-Tufted Layer V Pyramidal Cells in the Rat Somatosensory Cortex. Front Neuroanat 5 Available at: https://www.frontiersin.org/articles/10.3389/fnana.2011.00005/full.

Rubenstein JLR (2011) Annual Research Review: Development of the cerebral cortex: implications for neurodevelopmental disorders. J Child Psychol Psychiatry 52:339–355.

Sala C, Segal M (2014) Dendritic Spines: The Locus of Structural and Functional Plasticity. Physiol Rev 94:141–188.

Sanchez-Arias JC, Liu M, Choi CSW, Ebert SN, Brown CE, Swayne LA (2019) Pannexin 1 Regulates Network Ensembles and Dendritic Spine Development in Cortical Neurons. eNeuro 6:ENEURO.0503-18.2019.

Sanchez-Arias JC, Wicki-Stordeur LE, Swayne LA (2016) Perspectives on the role of Pannexin 1 in neural precursor cell biology. Neural Regen Res 11:1540–1544.

Sandilos JK, Chiu Y-H, Chekeni FB, Armstrong AJ, Walk SF, Ravichandran KS, Bayliss DA (2012) Pannexin 1, an ATP Release Channel, Is Activated by Caspase Cleavage of Its Pore-associated C-terminal Autoinhibitory Region. J Biol Chem 287:11303–11311.

Sando R, Bushong E, Zhu Y, Huang M, Considine C, Phan S, Ju S, Uytiepo M, Ellisman M, Maximov A (2017) Assembly of Excitatory Synapses in the Absence of Glutamatergic Neurotransmission. Neuron 94:312-321.e3.

Schätzle P, Silva ME da, Tas RP, Katrukha EA, Hu HY, Wierenga CJ, Kapitein LC, Hoogenraad CC (2018) Activity-Dependent Actin Remodeling at the Base of Dendritic Spines Promotes Microtubule Entry. Curr Biol 28:2081-2093.e6.

Schindelin J, Arganda-Carreras I, Frise E, Kaynig V, Longair M, Pietzsch T, Preibisch S, Rueden C, Saalfeld S, Schmid B, Tinevez J-Y, White DJ, Hartenstein V, Eliceiri

K, Tomancak P, Cardona A (2012) Fiji: an open-source platform for biological-image analysis. Nat Methods 9:676–682.

Schlaggar BL, Fox K, O'Leary DM (1993) Postsynaptic control of plasticity in developing somatosensory cortex. Nature 364:623–626.

Segal M (2005) Dendritic spines and long-term plasticity. Nat Rev Neurosci 6:277–284.

Shao Q, Lindstrom K, Shi R, Kelly J, Schroeder A, Juusola J, Levine KL, Esseltine JL, Penuela S, Jackson MF, Laird DW (2016) A germline variant in PANX1 has reduced channel function and is associated with multisystem dysfunction. J Biol Chem Available at: http://www.ncbi.nlm.nih.gov/pubmed/27129271.

Sigler A, Oh WC, Imig C, Altas B, Kawabe H, Cooper BH, Kwon H-B, Rhee J-S, Brose N (2017) Formation and Maintenance of Functional Spines in the Absence of Presynaptic Glutamate Release. Neuron 94:304-311.e4.

Solecki DJ, Govek E-E, Tomoda T, Hatten ME (2006) Neuronal polarity in CNS development. Genes Dev 20:2639–2647.

Sosinsky GE, Boassa D, Dermietzel R, Duffy HS, Laird DW, MacVicar B, Naus CC, Penuela S, Scemes E, Spray DC, Thompson RJ, Zhao H-B, Dahl G (2011) Pannexin channels are not gap junction hemichannels. Channels 5:193–197.

Spano GM, Banningh SW, Marshall W, Vivo L de, Bellesi M, Loschky SS, Tononi G, Cirelli C (2019) Sleep Deprivation by Exposure to Novel Objects Increases Synapse Density and Axon–Spine Interface in the Hippocampal CA1 Region of Adolescent Mice. J Neurosci 39:6613–6625.

Südhof TC (2018) Towards an Understanding of Synapse Formation. Neuron 100:276–293.

Svoboda K, Tank DW, Denk W (1996) Direct Measurement of Coupling Between Dendritic Spines and Shafts. Science 272:716–719.

Swayne LA, Boyce AKJ (2017) Regulation of Pannexin 1 Surface Expression by Extracellular ATP: Potential Implications for Nervous System Function in Health and Disease. Front Cell Neurosci 11 Available at: https://www.frontiersin.org/articles/10.3389/fncel.2017.00230/full.

Takano T, Xu C, Funahashi Y, Namba T, Kaibuchi K (2015) Neuronal polarization. Development 142:2088–2093.

Tibau E, Valencia M, Soriano J (2013) Identification of neuronal network properties from the spectral analysis of calcium imaging signals in neuronal cultures. Front Neural Circuits 7 Available at: https://www.frontiersin.org/articles/10.3389/fncir.2013.00199/full.

Trachtenberg JT, Chen BE, Knott GW, Feng G, Sanes JR, Welker E, Svoboda K (2002) Long-term in vivo imaging of experience-dependent synaptic plasticity in adult cortex. Nature 420:788–794.

Vanden Berghe T, Hulpiau P, Martens L, Vandenbroucke RE, Van Wonterghem E, Perry SW, Bruggeman I, Divert T, Choi SM, Vuylsteke M, Shestopalov VI, Libert C, Vandenabeele P (2015) Passenger Mutations Confound Interpretation of All Genetically Modified Congenic Mice. Immunity 43:200–209.

Verhage M, Maia AS, Plomp JJ, Brussaard AB, Heeroma JH, Vermeer H, Toonen RF, Hammer RE, Den TK van, Berg, Missler M, Geuze HJ, Südhof TC (2000) Synaptic Assembly of the Brain in the Absence of Neurotransmitter Secretion. Science 287:864–869.

Vogt A, Hormuzdi SG, Monyer H (2005) Pannexin1 and Pannexin2 expression in the developing and mature rat brain. Mol Brain Res 141:113–120.

Wang J, Ambrosi C, Qiu F, Jackson DG, Sosinsky G, Dahl G (2014) The membrane protein Pannexin1 forms two open-channel conformations depending on the mode of activation. Sci Signal 7:ra69–ra69.

Weaver JL, Arandjelovic S, Brown G, K. Mendu S, S. Schappe M, Buckley MW, Chiu Y-H, Shu S, Kim JK, Chung J, Krupa J, Jevtovic-Todorovic V, Desai BN, Ravichandran KS, Bayliss DA (2017) Hematopoietic pannexin 1 function is critical for neuropathic pain. Sci Rep 7:1–15.

Weilinger NL, Lohman AW, Rakai BD, Ma EMM, Bialecki J, Maslieieva V, Rilea T, Bandet MV, Ikuta NT, Scott L, Colicos MA, Teskey GC, Winship IR, Thompson RJ (2016) Metabotropic NMDA receptor signaling couples Src family kinases to pannexin-1 during excitotoxicity. Nat Neurosci 19:432–442.

Weilinger NL, Tang PL, Thompson RJ (2012) Anoxia-Induced NMDA Receptor Activation Opens Pannexin Channels via Src Family Kinases. J Neurosci 32:12579–12588.

Weinhard L, di Bartolomei G, Bolasco G, Machado P, Schieber NL, Neniskyte U, Exiga M, Vadisiute A, Raggioli A, Schertel A, Schwab Y, Gross CT (2018) Microglia remodel synapses by presynaptic trogocytosis and spine head filopodia induction. Nat Commun 9:1–14.

Wenzel M, Han S, Smith EH, Hoel E, Greger B, House PA, Yuste R (2019) Reduced Repertoire of Cortical Microstates and Neuronal Ensembles in Medically Induced Loss of Consciousness. Cell Syst 8:467-474.e4.

Wicki-Stordeur LE, Boyce AKJ, Swayne LA (2013) Analysis of a pannexin 2-pannexin 1 chimeric protein supports divergent roles for pannexin C-termini in cellular localization. Cell Commun Adhes 20:73–79.

Wicki-Stordeur LE, Sanchez-Arias JC, Dhaliwal J, Carmona-Wagner EO, Shestopalov VI, Lagace DC, Swayne LA (2016) Pannexin 1 Differentially Affects Neural Precursor Cell Maintenance in the Ventricular Zone and Peri-Infarct Cortex. J Neurosci 36:1203–1210.

Wicki-Stordeur LE, Swayne LA (2013) Panx1 regulates neural stem and progenitor cell behaviours associated with cytoskeletal dynamics and interacts with multiple cytoskeletal elements. Cell Commun Signal 11:62.

Xiao F, Waldrop SL, Khimji A, Kilic G (2012) Pannexin1 contributes to pathophysiological ATP release in lipoapoptosis induced by saturated free fatty acids in liver cells. Am J Physiol-Cell Physiol 303:C1034–C1044.

Xu X, Wicki-Stordeur LE, Sanchez-Arias JC, Liu M, Weaver MS, Choi CSW, Swayne LA (2018) Probenecid Disrupts a Novel Pannexin 1-Collapsin Response Mediator Protein 2 Interaction and Increases Microtubule Stability. Front Cell Neurosci 12 Available at: https://www.frontiersin.org/articles/10.3389/fncel.2018.00124/full.

Yang D, He Y, Muñoz-Planillo R, Liu Q, Núñez G (2015) Caspase-11 Requires the Pannexin-1 Channel and the Purinergic P2X7 Pore to Mediate Pyroptosis and Endotoxic Shock. Immunity 43:923–932.

Yang G, Gan W-B (2012) Sleep contributes to dendritic spine formation and elimination in the developing mouse somatosensory cortex. Dev Neurobiol 72:1391–1398.

Yang Y, Delalio LJ, Best AK, Macal E, Milstein J, Donnelly I, Miller AM, McBride M, Shu X, Koval M, Isakson BE, Johnstone SR (2020) Endothelial Pannexin 1 Channels Control Inflammation by Regulating Intracellular Calcium. J Immunol:ji1901089.

Yuste R (2011) Dendritic Spines and Distributed Circuits. Neuron 71:772–781.

Yuste R, Bonhoeffer T (2004) Genesis of dendritic spines: insights from ultrastructural and imaging studies. Nat Rev Neurosci 5:24–34.

Zack GW, Rogers WE, Latt SA (1977) Automatic measurement of sister chromatid exchange frequency. J Histochem Cytochem 25:741–753.

Zappalà A, Cicero D, Serapide MF, Paz C, Catania MV, Falchi M, Parenti R, Pantò MR, La Delia F, Cicirata F (2006) Expression of pannexin1 in the CNS of adult mouse: Cellular localization and effect of 4-aminopyridine-induced seizures. Neuroscience 141:167–178.

Zhang Y, Chen K, Sloan SA, Bennett ML, Scholze AR, O'Keeffe S, Phatnani HP, Guarnieri P, Caneda C, Ruderisch N, Deng S, Liddelow SA, Zhang C, Daneman R, Maniatis T, Barres BA, Wu JQ (2014) An RNA-Sequencing Transcriptome and Splicing Database of Glia, Neurons, and Vascular Cells of the Cerebral Cortex. J Neurosci 34:11929–11947.

Ziv NE, Smith SJ (1996) Evidence for a Role of Dendritic Filopodia in Synaptogenesis and Spine Formation. Neuron 17:91–102.

Zoidl G, Petrasch-Parwez E, Ray A, Meier C, Bunse S, Habbes H-W, Dahl G, Dermietzel R (2007) Localization of the pannexin1 protein at postsynaptic sites in the cerebral cortex and hippocampus. Neuroscience 146:9–16.

Zuo Y, Lin A, Chang P, Gan W-B (2005a) Development of Long-Term Dendritic Spine Stability in Diverse Regions of Cerebral Cortex. Neuron 46:181–189.

Zuo Y, Yang G, Kwon E, Gan W-B (2005b) Long-term sensory deprivation prevents dendritic spine loss in primary somatosensory cortex. Nature 436:261–265.